Contribution to the Development of an Adaptive Solver for Numerical Simulation of Steady and Unsteady Flows

Von der Fakultät für Mathematik, Informatik und Naturwissenschaften
der RWTH Aachen University
zur Erlangung des akademischen Grades eines
Doktors der Ingenieurwissenschaften genehmigte Dissertation

vorgelegt von

Master in Technology
Saurya Ranjan Ray
aus
Gop, Puri, Indien

Berichter: Universitätsprofessor Dr.-Ing. Josef Ballmann
Universitätsprofessor Dr. rer. nat. Nicolas R. Gauger

Tag der müdlichen Prüfung: 25.01.2013

Published by Saurya Ranjan Ray in 2013

ISBN: 978-0-9926468-0-6

Acknowledgements

The material presented in this thesis is based on the work conducted at Lehr- und Forschungsgebiet für Mechanik, RWTH, Aachen between May, 2001-May, 2007. I had been a part of the group, working in the Collaborative Research Center project (SFB 401) ”Flow Modulation and Fluid-Structure Interaction at Airplane Wings” sponsored by the Deutsche Forschungsgemeinschaft.

Firstly, I am indebted to Prof. Dr-Ing. Josef Ballmann for imposing trust on me to work in such a challenging and dynamic project. His lectures in Gasdynamics and technical guidance have essentially built my foundation on the compressible fluid dynamics and heat transfer. I am grateful to him for providing a patient ear during numerous helpful discussions in diverse topics and encouraging me through out the work.

I am thankful to Prof. Dr. Nicolas R. Gauger to go through the draft copy of the thesis and affirmed to be one of the supervisors.

My gratitude to Prof. J.C. Mandal of IIT, Bombay for providing an early guidance and encouragement to pursue PhD in RWTH, Aachen.

My thanks goes to Dr. Frank Bramkamp for his helpful guidance in introducing me to Quadflow during the early phase. Thanks to Philipp Lamby for his support in providing grids for all the numerical simulations discussed in this thesis. Special thanks to Dr. Siegfried Müller for briefing me through the complexity of the wavelet analysis tool used in the adaptation module.

Thanks to the LFM team members Carsten, Birgit, Michi, Willy, Sigrid; specially to Christoph Hohn and Dr. Alexander Karavas for making my stay in Germany enjoyable.

Last but not the least, I owe a lot to the support of my parents and wife in the final phase of completion of the thesis.

Kurzfassung

Die Arbeit behandelt die Ertüchtigung des unstrukturierten, adaptiven, Finite-Volumen-Lösungsverfahrens QUADFLOW für Strömungen kompressibler Fluide. Der bestehende Löser ist ein integriertes Werkzeug mit multiskalenbasierter Gitteradaption und B-Spline-Techniken zur Erzeugung von Viereck- bzw. Hexaedernetzen. Weil die Gitteradaption hängende Knoten einbringen kann, ist die Datenstruktur zelloberflächenorientiert. Für die Flussdiskretisierung sind Upwind-Methoden und für die Zeitdiskretisierung eine explizite sowie implizite Formulierungen in Kombination mit Newton-Linearisierung und Krylov-Unterraum Methode eingebaut. In der Dissertation wird ein Vorkonditionierer nach der Formulierung von Weiss und Smith zur Simulation reibungsfreier und reibender Strömungen kleiner Machzahl um Profile in Reise- und Hochauftriebskonfiguration eingebaut. Die Ergebnisse offenbaren das Erzielen Machzahl-unabhängiger Werte für Auftriebs- und Widerstandskoeffizienten (d'Alembert-Paradoxon) und treffen sehr gut Resultate der Literatur. Der Wandabstand für die Turbulenzmodellierung wird bei Auftreten sehr gestreckter, verfeinerter Zellen und hängender Knoten mittels Vektoralgebra abgeschätzt, um adaptionsbedingt gestörte Wandreibungsverteilungen zu vermeiden. Weiters wird dargestellt, dass ein "Detached-Eddy-Ansatz" auf Basis des Spalart-Allmaras Turbulenzmodells sich zusammen mit der Gitteradaption als effektiv erweist und sich bei Hochauftriebskonfigurationen sehr gut zur Erfassung massiver Strömungsablösung eignet. Mittels zeitlicher Rückwärtsdifferenzen wird eine geometrisch konservative, implizite Diskretisierung zweiter Ordnung formuliert, eingebaut und durch Simulation instationärer, reibungsfreier Strömung um ein nickendes NACA0012 Profil validiert. Die Methode erweist sich dem vorher verwendeten Mittelpunktsschema überlegen, indem es größere Zeitschrittweiten und CFL-Zahlen erlaubt. Die nichtlineare Multigrid-Methode, basierend auf "Full Approximation Storage" mit V-Zyklus, wird implementiert, um die Konvergenz des zeitlich expliziten Verfahrens bei der Lösung reibungsfreier Strömungsprobleme zu beschleunigen. Die Gittervergröberung fußt auf einer hierarchischen Strategie, die feineren Zellen, die zu identischen Elternzellen auf gleicher Verfeinerungsstufe gehören, zu einer Folge von Grobgittern zusammenzufassen. Der Restriktionsoperator basiert auf dem Volumengewicht, die Prolongation erfolgt mittels des Upwind-Schemas. Alle Implementierungen in das Lösungsverfahren werden an verfügbaren experimentellen und numerischen Resultaten ausführlich validiert. Es werden vollturbulente Strömungen bei unterschiedlichen Anström-Mach- und -Reynoldszahlen berechnet und mit Daten aus im Auftrag des SFB 401 durchgeführten KRG-Experimenten verglichen, darunter Tests, in denen starke Stoß-Grenzschicht-Interaktionen und Buffet beobachtet wurden, was numerisch an drei Gitterauflösungen studiert wird. Daraus folgt, dass eine angemessene Gitterauflösung in Strömungsrichtung für eine genaue Wiedergabe des Stoß-Buffet vital ist. Das Ende der Arbeit enthält Erweiterungen des adaptiven Strömungslösers für die dreidimensionale Strömungssimulation und auch erste Ergebnisse aus Berechnungen mit der vorhandenen Computerausstattung.

Abstract

The work deals with enhancing the capabilities of the unstructured adaptive Finite Volume flow solver QUADFLOW for compressible fluid flow. The solver exists as an integrated tool with multiscale based grid adaptation and B-spline based quadrilateral/hexahedral multi-block grid generation modules. Due to hanging nodes introduced through grid adaptation, data structure is cell face based. Upwind methods are implemented for flux discretisation in combination with explicit time integration as well as implicit temporal discretisation using Newton linearisation and Krylov subspace method. In the thesis, a preconditioner based on the formulation of Weiss and Smith is implemented for simulating inviscid and viscous flows at low Mach number over airfoils in cruise as well as high lift configurations. The results demonstrate the achievement of Mach number independent lift and drag coefficients (D'Alembert's paradox) and have an excellent agreement with results available in the literature. The wall distance for the turbulence modelling in the presence of highly stretched, refined cells and hanging nodes close to the wall is correctly estimated using vector algebra. With this formulation, the wriggles in the skin friction distribution due to grid adaptation are avoided. Detached Eddy formulation based on the Spalart-Allmaras turbulence model is shown to be effective together with the grid adaptation and demonstrated to have excellent stall capturing characteristics for high lift configurations. A second order accurate, geometrically conservative implicit scheme, based on Backward Difference discretisation is formulated, implemented and validated to simulate the unsteady inviscid flow over the pitching NACA0012 profile. The method shows an advantage over the existing Mid-point scheme allowing relatively higher time steps and higher global CFL numbers during the simulation. The non-linear multigrid method based on the Full Approximation Storage scheme with V-cycle is implemented to improve the convergence behaviour of the explicit scheme in solving inviscid flow problems. The coarsening is based on the hierarchical agglomeration strategy to combine the fine cells belonging to the identical parent cell at the same level to generate a series of coarse grid levels. The restriction operator is based on the volume weightiness and the prolongation operation is carried out using the upwind scheme. The implementations in the solver are extensively validated using results from available experiments and numerical solutions existing in the literature. Fully turbulent flow computations at different free stream Mach numbers and Reynolds numbers are carried out and compared with data obtained from the KRG experiments conducted in Goettingen on behalf of SFB 401, including some tests where strong shock-boundary layer interaction with buffet was observed. These are studied at three different grid resolutions. It is concluded that the adequate resolution of the grid cells along the stream-wise direction is vital in accurately resolving the flow physics in shock buffet. Furthermore, code extensions are carried out to offer the capability to the adaptive solver for simulating three-dimensional flow and some first computations are performed with the available computational power.

Contents

List of Figures

List of Tables

Nomenclature

α	Angle of attack
Δt	Timestep
$\dot{Q}$	Heat generation per unit volume
ε	Limiting value of the normal Mach number in preconditioning
Γ_c	Preconditioning matrix for the conservative variables
$\hat{\rho}$	Non-dimensional density of the fluid
$\hat{t}$	Non-dimensional temperature of the fluid
$\hat{u}$	Non-dimensional velocity of the fluid along X-direction
$\hat{v}$	Non-dimensional velocity of the fluid along Y-direction
$\hat{x}$	Non-dimensional length along X-direction of the computational domain
$\hat{y}$	Non-dimensional length along Y-direction of the computational domain
κ	reduced frequency of the structural oscillation
λ	Bulk viscosity of the fluid
μ	Dynamic viscosity of the fluid
μ_t	Turbulent viscosity
μ_{ref}	Reference dynamic viscosity of the fluid
ω	angular velocity of the oscillating structure
$\Omega(t)$	Volume of the control cell at time t
Ω^k	Control volume at the k_{th} Newtonstep
Ω^n	Control volume at the n_{th} timestep
Ω^{n+1}	Control volume at the $(n+1)_{th}$ timestep
Ω^{n-1}	Control volume at the $(n-1)_{th}$ timestep
$\partial\Omega(t)$	Temporally varying control surface enclosing the control volume
ρ	Density of the fluid in the control volume

ρ_{ref}	Reference density of the fluid
τ	Deviatoric stress tensor
σ	Surface traction tensor
F_b	Contribution of the source vector per unit volume
f_b	Body force per unit mass
F_c	Convective flux vector
F_v	Diffusive flux vector
F	flux vector
f	A generic transported quantity
I	Unit matrix
q	Heat flux vector
$V^{'}$	Instantaneous velocity vector of the fluid (not time averaged)
V	Time averaged velocity vector of the fluid in the control volume
V_g^m	Scaled grid velocity
B_1	Backward-Euler timestep
C	Sutherland's constant
C_d	Aerodynamic total drag coefficient
C_f	Aerodynamic skin friction drag coefficient
C_L	Aerodynamic lift coefficient
C_p	Specific heat of the air at constant pressure
c_v	Specific heat of the air at constant volume
Cp	Surface static pressure coefficient
$d\Omega$	Elemental change in control volume
e	Internal energy of the fluid due to temperature
$E^{'}$	Instantaneous energy of the fluid due to fluctuating temperature

E_{ref}	Reference energy of the fluid
J	Jacobian matrix
k	Turbulent kinetic energy
k_t	Turbulent thermal conductivity of the fluid
K_w	Zonal boundary specification parameter for the DES model
L_e	Lifting efficiency of the airfoil
M_∞	Free stream Mach number of the air
M_{ref}	Reference Mach number
N_p	Number of grid points in the computational domain
p	Static pressure of the air
p_{ref}	Reference pressure of the fluid
Pr	Prandtl number
Pr_t	Turbulent Prandtl number
$Q(x,t)$	Spatially and temporally varying conservative flow variable
Q^{k+1}	Conservative variable at $(k+1)_{th}$ Newton iteration
Q^k	Conservative variable at k_{th} Newton iteration
Q^{n+1}	Conservative variable at $(n+1)_{th}$ time
Q^{n-1}	Conservative variable at $(n-1)_{th}$ time
Q^n	Conservative variable at $(n)_{th}$ time
R	Gas constant of the air
Re	Reynolds number
Re_{ref}	Reference Reynolds number
$Res(Q^{k+1})$	Residual at $(k+1)_{th}$ time
$Res(Q^k)$	Residual at k_{th} time
$Res(Q^{n+1})$	Residual at $(n+1)_{th}$ time

$Res(Q^n)$	Residual at n_{th} time
S	Strain rate quantity
T	Absolute temperature of the fluid
T_m	Grid resolved turbulent time scale
T_t	Numerically resolved turbulent time scale
T_{ref}	Reference temperature of the fluid
t_{ref}	Reference time
u	Velocity of the fluid along X-direction
u_τ	friction velocity
u_{ref}	Reference speed of the fluid
v	Absolute value of the velocity of the fluid
V_∞	Free stream speed of the air
w	Velocity of the fluid along Z-direction
x_{ref}	Reference length
y^+	y plus ($\frac{yu_\tau}{\nu}$)
c	chord length of the airfoil
E	Total internal energy of the fluid
K	Cut-off parameter used in preconditioning matrix
v	Velocity of the fluid along Y-direction

Acronyms

LEVM Linear Eddy Viscosity Model

RANS Reynolds Averaged Navier-Stokes formulation

DES Detached Eddy Simulation

LES Large Eddy Simulation

SGS Sub-grid Scale model

DNS Direct Numerical Simulation

BDF Backward Difference Formulation

GCL Geometric Conservation Law

ETW European Transonic Windtunnel

MUSCL Monotonic Upwind Scheme for Conservation Laws

1 Introduction

The incremental evolution in the technology of today's transport aircraft over the last decade has led to the belief that the discipline of aeronautics is gradually entering into maturity. Today's aeronautics is characterised by analysis and design tools that are relatively mature and based on the current understanding of the physics of the flight. Current tools, combined with significant empiricism and experience, have been successful in developing concepts and designing new vehicle systems [1].

Gradually, the aeronautics is entering into a phase, where the expectation is to bring improvement in the multidisciplinary simulations to decrease the aerodynamic design time, reduce the development cycle time for aircrafts [2], optimise the aerodynamic shape, simulate off-design flow configurations associated with the complex flow fields, and design innovative aerodynamic configurations to push the flight envelop.

Computational Fluid Dynamics has already achieved the status of a valid, reliable and cost effective tool in aeronautics to aid the process of simulation, analysis, understanding and control of the flow phenomena. The applicability of the CFD has further been pushed by the recent growth in the availability of the computational resources in the form of increase in the processing power and development in the memory architecture. In addition to that, improvement in the numerical techniques has augmented the progress of CFD in a direction to cater to the current expectations from the aeronautical research and technology.

To date, enormous challenges are imposed on the CFD methods from the perspective of solution accuracy, robustness of the scheme to widen the applicabilities, improvement in the computational speed for simulating the flow field over complex aerodynamic configurations. The stringent requirement of solution accuracy can be demonstrated from the fact that a unit drag count ($\Delta C_d = 10^{-4}$) is equivalent to four passengers for a large transport aircraft [3].

Hence, the development of a state-of-the art CFD tool comprising of numerical components, based upon valid theoretical frameworks, and has the ability to address the issues related to the accuracy, robustness and speed in resolving the flow field is crucial. The current work, carried out in the above motivation contributes significantly to the research and applications of the CFD.

Quadflow

The work described in this thesis is carried out in the context of development and application of a CFD tool (Quadflow) with the above mentioned objectives to improve computational speed, accuracy and robustness of the flow solver. Quadflow is a CFD software package developed by a group within the Collaborative Research Center project (SFB 401), "Flow Modulation and Fluid-Structure Interaction at Airplane Wings" sponsored by the Deutsche Forschungsgemeinschaft. The Quadflow code is in the developing stage with an existing framework set upon by the earlier work [4–7].

The core of the Quadflow code is based upon the concept of grid adaptation, where the mesh resolution is controlled on the basis of multiscale analysis [6] of the intermediate flow solution in order to improve the accuracy of the final numerical solution. The grid generation process and the numerical schemes in the flow solver are designed to aid in achieving this objective. The flow solver, grid generation and grid adaptation modules are tightly integrated to form the CFD software package, *Quadflow*.

Flow solver: The flow solver is based on a cell-centered finite volume scheme, with face based data structure to effectively deal with regions of the computational domain containing hanging nodes. The detailed description of the available numerical schemes and their applicability is provided in Chapter-2.

Grid generation: The conceptual framework of the grid generation module in Quadflow is designed to address the following numerical aspects.:

- Appropriate approximation of the curvilinear surface in the physical domain.
- Hierarchical representation of the cells necessary for the grid adaptation constraining the child cells to be exactly overlapped by the parent cell.

The first criterion is linked to the geometrical modelling of the structural configuration and achieved through the representation of the mesh lines using B-spline curves [8, 9]. The control points on the curvilinear B-splines are relocated to model the geometrical boundaries with boundary conforming curves. The disassociation of the required number of points for accurate resolution of the surface (CAD modelling) from the number of required grid points to efficiently resolve the flow field (Numerical modelling) is the essential feature of the grid generation module.

The satisfaction of the second criterion is essential in supporting the concept of grid adaptation. The computational domain is discretised in two dimensions with a multiblock structured grid of quadrilateral (hexahedral in 3D) cells. The cells are arranged in a hierarchical structure with block, level and index information, which is unique to the adaptive solver, Quadflow.

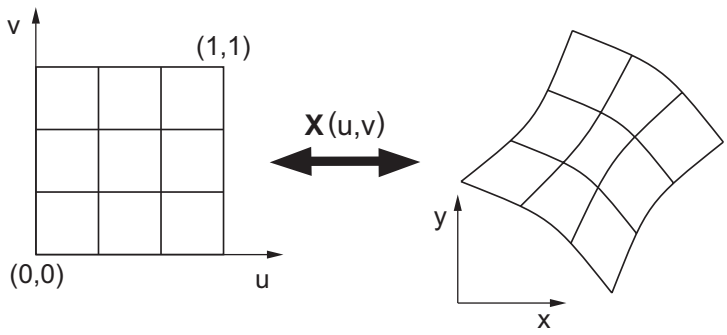

Figure 1: Parametric mapping during grid generation

Fig. 1 shows the *parametric transformation* of the physical domain into the logical space for generation of nested hierarchical cells suitable for adaptation.

Adaptation: The solver employs a wavelet based adaptive technique [6], utilising a quadtree data structure to detect highly active regions embedded in the flow domain to eventually refine or even coarsen the grid in the less active regions, resulting in a change in the grid topology. It is achieved by *multiscale decomposition* of the solution variables at the cell centers of a particular grid level Q_L into a sequence of cell averages (Q_{L-1}) and the detail coefficients (d_{L-1}) for lower levels recursively, till the coarsest grid level is achieved (shown in Fig. 2) . The method of

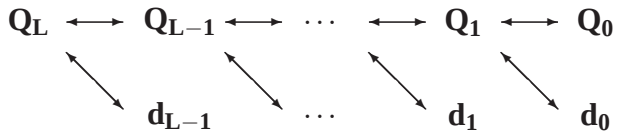

Figure 2: Pyramid scheme of multiscale transformation

transformation for generating the coefficients depend only on the geometry of the cells rather than the cell averages. The amount of variation in the detail coefficients of four child cells belonging to a parent cell (in 2D) is considered as the criterion for grid refinement. A threshold parameter is chosen to control the intensity of refinement in the computational domain. The grid refinement is isotropic in nature. In two dimensional flow simulation, four consecutive child cells at a higher level are created as a result of the refinement of a parent cell. During the coarsening operation, the four cells are coalesced together to form a single cell at one level lower than the original child cells. The level of the cell remains unchanged if it stays unaffected during the process of grid adaptation. The resulting modification of the grid cells due to grid adaptation is constrained to a specific block. The cross transfer of the cells from one block to another is prevented during adaptation.

The applications considered in the course of the work is primarily for resolving the external flow field over the lifting structures used in the transport aircraft. One of the active research areas that has huge impact on the economics, performance and safety of the transport aircraft is the efficient design of the high-lift configuration during take off and landing phases [10]. The task is challenging because of the complexity of the flow; involving a mixture of localised subsonic and supersonic regions and the interaction of the boundary layer with the wake of the preceeding components. The enormity of the task can be realised from the number of research programs being conducted in the past and are currently running; e.g. HIRENASD [11], AST/IWD [2], EUROLIFT [12], MEGAFLOW [13]. Several studies have been conducted on flow simulation, analysis and design of the high lift configuration, e.g. Aerodynamic Shape Optimisation (ASO) of the high-lift configuration with viscous adjoint method [14], delaying separation on the flap surface by periodic injection of air [15], numerical modelling of transition [16] and

many others [17–19].

An efficient and reliable prediction of the flow field over the high-lift configuration is crucial and critical because of its primary importance on the aircraft design. Though, several previous studies [13, 47] are able to accurately predict the variation of the lift coefficient with angle of attack in the linear region; the solution accuracy is observed to be deteriorated near the stall and in the post stall region. Accurate resolution of the flow field over the high-lift configuration in both design and off-design conditions with improved turbulence modelling and grid adaptation has been given a high priority in the work.

A low Mach number preconditioner is implemented to improve the convergence behaviour of the predominant low Mach number regions in the flow field over a high-lift configuration. Implementation of the low Mach number preconditioner in Quadflow helps in unifying the simulation methods for compressible and incompressible flow fields.

Quadflow is intended to be used as a highly accurate and robust tool for aeroelastic analysis involving fluid-structure interaction. This involves the challenges of designing a numerical scheme to

- use higher order discretisation in time for improved temporal resolution,
- satisfy the *geometric conservation law* in the presence of dynamic mesh movement,
- be robust in order to increase the simulation timestep for reducing the computational time,
- be able to efficiently utilise the concept of grid adaptivity for improved spatial resolution of the flow field.

A second order time accurate and geometrically conserved implicit backward difference scheme has been formulated, implemented and tested in the adaptive flow solver Quadflow to enhance the speed and robustness for simulating unsteady problems with the mesh movement.

Computation is performed over a transonic airfoil (SFB profile) to understand the significantly complex and challenging aerodynamic phenomenon of ”shock buffet”, caused by the interaction between the boundary layer and the shock closing the transonic domain, resulting in the non-harmonic periodic oscillation of the shock along the profile. The numerically predicted solution is compared with the experimentally available data. The following aspects of the physical phenomena are analysed.

- flow configuration triggering the onset of the shock buffet,
- shock traversing distance on the surface of the airfoil,
- frequency of the shock oscillation,
- temporal variation of the static pressure coefficients on the airfoil surface.

The application of turbulence modelling using DES method is demonstrated in accurate capturing of the stalling angle of the high-lift configuration. A Full Approximation Storage (FAS), geometric Multigrid method is implemented to enhance the convergence acceleration of the explicit time integration scheme. The component of the implicit time integration scheme, e.g. the method to compute the Jacobian matrix is enhanced. Further work is carried out to extend the applicabilities of Quadflow for simulating three-dimensional flow fields.
Huge amount of data available from the experiments conducted at the Kryo-Rohrwindkanal Göttingen (KRG) [22, 23] provides an opportunity to validate the numerical simulation and demonstrate the accuracy of the numerical schemes implemented in Quadflow. Additionally, available numerical and experimental results in the existing literature are used for validation.

The contents of the thesis are organised in the following way. The formulation of the numerical schemes used in modelling and their implementation in Quadflow is described in Chapter-2. The approach to the flow modelling determined by analysing the physical mechanisms in the flow field and the basis of the derivation of numerical formulations are explained in the chapter. The numerical schemes to simulate turbulent flow, low Mach number flow and unsteady flow fields in the presence of mesh movement are elucidated. Chapter-3 illustrates the application of the schemes in simulating flow over different configurations. The results are analysed and the numerical schemes are validated by comparing with the experimentally available data or with the pre-existing reliable numerical solutions. The benefits of the methods in accelerating convergence and improving the accuracy of the flow solution are assessed. Finally, the concluding chapter outlines the inferences drawn on the basis of the present work and provides recommendations on the possible future progress of the work.

2 Numerical Modelling and Implementation

The fundamental behaviour of a physical problem can be mathematically modelled under a certain set of assumptions to give rise to a set of equations, termed as *governing equations*. The assumptions are considered either in order to reduce the complexity of the mathematical modelling or to address a problem where the physical effect is considered to be insignificantly influencing the solution. The type and nature of the governing equations determine the characteristics of the physical problem. The equations along with the initial and boundary conditions provide the condition of *wellposedness* to the problem, where the solution is known to exist. The possibility of expressing the governing equation in different forms (weak/strong) leads to distinct formulations (FVM/FDM/FEM) which can be solved with the adoption of various strategies available in the existing literature [24]. Numerical discretisation of the governing

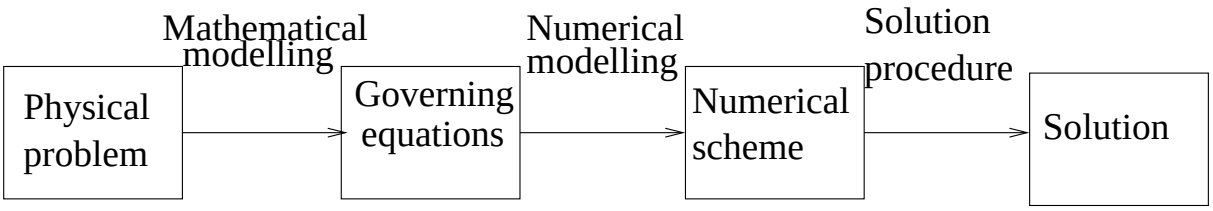

Figure 3: Steps of modelling the physical problem leading to solution

equation with the help of Taylor series expansion leads to the creation of a numerical model of the problem. Stability, convergence and accuracy of the numerical scheme depends on the discretisation process. Iterative schemes are employed to solve the numerical models to achieve the required solution to the problem.

The effort to numerically model the governing equation for the problems related to the aerodynamics of the airfoil and wing structures is described in the current section dealing with the aspect of numerical modelling.

2.1 Governing equations

Laws of continuum mechanics provide the mathematical basis to explain the dynamics of a system comprising of a continuous distribution of particles in the sense of continuum mechanics. Navier-Stokes equations, consisting of conservation of mass, momentum and energy, are used as the governing equations to mathematically model and physically explain the flow field under the assumption of continuity in the medium. Out of all possible forms, the weak integral form is suitable to deal with the discontinuities in the flow field. In a single phase aerodynamic flow field, the spatial discontinuities appear in the form of jumps of the flow variables arising out of non-linearity in the governing equations under a certain set of boundary conditions.

The integral form of Navier-Stokes equations in Finite Volume formulation is,

$$\frac{d}{dt}\int_{\Omega(t)} Q d\Omega = \oint_{\partial\Omega(t)} F \cdot n ds + \int_{\Omega(t)} F_b d\Omega. \tag{1}$$

Splitting the flux into convective and viscous terms yields

$$\frac{\partial}{\partial t}\int_{\Omega(t)} Q d\Omega + \oint_{\partial\Omega(t)} F_c \cdot n ds = \oint_{\partial\Omega(t)} F_v \cdot n ds + \int_{\Omega(t)} F_b d\Omega. \tag{2}$$

$$Q = \begin{pmatrix} \rho \\ \rho V \\ \rho E \end{pmatrix}, \quad F_c = \begin{pmatrix} \rho V' \\ \overline{\rho V' \otimes V'} \\ \overline{\rho V' E'} \end{pmatrix}, \quad F_v = \begin{pmatrix} 0 \\ \sigma \\ \sigma \cdot V - q \end{pmatrix}, \quad F_b = \begin{pmatrix} 0 \\ \rho f_b \\ \rho f_b \cdot V - \rho \dot{Q} \end{pmatrix},$$

where Q is the conservative vector representing the state variables. F_c and F_v represent the contribution of the convective and diffusive fluxes through the control surfaces into the control volume, respectively. ρf_b is the body force per unit volume experienced by the fluid in the control volume.

E is the total internal energy of the fluid and defined as $E = e + \frac{V^2}{2}$. It includes the internal energy of the fluid by virtue of its molecular motion in the form of temperature and the dynamic head, resulted from the velocity stream. The internal energy (e) of a calorically perfect gas is a function of temperature and is expressed as $e = c_v T$, Where c_v is the specific heat of the fluid at constant volume.

σ is the surface traction tensor experienced by the fluid at the control surfaces. From Stokes' law, in matrix notation, $\sigma = -pI + \tau$. p is the static pressure experienced by the fluid and τ is the Deviatoric stress tensor. The constitutive relation for Newtonian fluids correlates the stress and strain tensor through the dynamic viscosity (μ) , giving rise to

$$\tau = \mu(\nabla V + \nabla V^T) + \lambda I \nabla \cdot V \tag{3}$$

λ represents the bulk viscosity and accounts for the component of stress due to the compressible strain. Enforcement of equality between the thermodynamic pressure with the hydrodynamic pressure leads to the satisfaction of $\tau_{ij}\delta_{ij} = 0$, giving rise to the condition $\lambda = -\frac{2}{3}\mu$. Dynamic viscosity ($\mu$) is a property of the fluid which depends on the absolute temperature. Its variation in the computational domain is modelled using Sutherland's law, $\mu = \mu_{ref}(\frac{T}{T_{ref}})^{\frac{3}{2}}\frac{T_{ref}+C}{T+C}$. The reference value of the dynamic viscosity (μ_{ref}) is obtained using the reference temperature (T_{ref}) (explained in the section 2.2 dealing with non-dimensionalisation of the governing equations) and the preset reference Reynolds number. Sutherland's temperature (C) is a constant, set to 110.4K.

V' in Eqn. (2) represents the instantaneous velocity components, comprising of the mean value and the fluctuating part. Temporal average of the dyadic product of the instantaneous quantity gives rise to the Reynolds stress tensor as explained in the turbulence modelling section 2.3 in the later part of this thesis.

The heat flux vector (q), depends upon the temperature gradients of the flow and is modelled by the Fourier's law, $q = -k\nabla T$. k is the thermal conductivity of the fluid and is related to the dynamic viscosity of the fluid through Prandtl's number. Thus, $k = \frac{\mu C_p}{Pr}$, where C_p is the specific heat of the gas at constant pressure. $\dot{Q}$ is the volumetric heat supply to the unit mass of fluid in the control volume. In the present work, air is modelled as a thermally perfect working fluid with constant values of the specific heats (C_p, C_v). The state equation, $p = \rho RT$ is used in addition to the governing equations to establish the closure in relation among the flow variables under the assumption of the ideal gas condition.

2.2 Non-dimensionalisation of the governing equation

The conservative variables exist in different orders of magnitude when expressed in physical units. They are non-dimensionalised in order to avoid significant round-off errors cropping up during numerical iterative processes. In this work we consider two-dimensional time-dependent flow.

For operational convenience during non-dimensionalisation, the governing equations are expressed in conservative Finite Difference form. The continuity equation becomes

$$\frac{\partial \rho}{\partial t} + \frac{(\partial \rho u)}{\partial x} + \frac{(\partial \rho v)}{\partial y} = 0.$$

Substituting the dimensioned flow variables as the product of non-dimensional and reference quantities,

$$\Rightarrow \frac{\partial(\hat{\rho}\rho_{ref})}{\partial(\hat{t}t_{ref})} + \frac{\partial(\hat{\rho}\rho_{ref}\hat{u}u_{ref})}{(\hat{x}x_{ref})} + \frac{\partial(\hat{\rho}\rho_{ref}\hat{v}u_{ref})}{(\hat{y}x_{ref})} = 0,$$

where,

$\hat{\rho} = \frac{\rho}{\rho_{ref}}, \hat{u} = \frac{u}{u_{ref}}, \hat{v} = \frac{v}{u_{ref}}, \hat{t} = \frac{t}{t_{ref}},$

$\hat{x} = \frac{x}{x_{ref}}, \hat{y} = \frac{y}{x_{ref}}, \hat{p} = \frac{p}{p_{ref}}, \hat{E} = \frac{E}{E_{ref}}.$

Reference quantities are set based on the free stream values of the flow variables. Thus, $\rho_{ref} = \rho_\infty$, $u_{ref} = c_\infty$, where c_∞ is the sonic speed based on the free stream variables. x_{ref} is set to the chord length of the airfoil and reference time, $t_{ref} = x_{ref}/u_{ref}$.

Reference values, being constant, can be taken outside of the partial derivative terms. Thus,

$$\Rightarrow \frac{\rho_{ref}}{t_{ref}}\frac{\hat{\rho}}{\hat{t}} + \frac{(\rho_{ref}u_{ref})}{x_{ref}}\frac{\partial(\hat{\rho}\hat{u})}{\partial\hat{x}} + \frac{(\rho_{ref}u_{ref})}{x_{ref}}\frac{\partial(\hat{\rho}\hat{v})}{\partial\hat{y}} = 0,$$

Cancelling the reference terms, we have the non-dimensional form of the continuity equation

$$\Rightarrow \frac{\partial\hat{\rho}}{\partial\hat{t}} + \frac{\partial(\hat{\rho}\hat{u})}{\partial\hat{x}} + \frac{\partial(\hat{\rho}\hat{v})}{\partial\hat{y}} = 0. \tag{4}$$

Momentum equation along the x-direction in the absence of the body force can be written as

$$\frac{\partial(\rho u)}{\partial t}+\frac{\partial(\rho u^2+p)}{\partial x}+\frac{\partial(\rho uv)}{\partial y}+\frac{\partial(\tau_{xx})}{\partial x}+\frac{\partial(\tau_{xy})}{\partial y}=0.$$

The reference value of the pressure (p_{ref}) is set in order to achieve a unit Euler number. Hence, p_{ref}=$\rho_{ref}u_{ref}^2$. and $T_{ref}=u_{ref}^2$

Introducing the reference variables and rearranging the terms, the dimensional form of the momentum equation gives rise to

$$\Rightarrow \frac{\partial(\hat{\rho}\hat{u})}{\partial \hat{t}}+\frac{\partial(\hat{\rho}\hat{u}^2+\hat{p})}{\partial \hat{x}}+\frac{\partial(\hat{\rho}\hat{u}\hat{v})}{\partial \hat{y}}+\frac{1}{Re_{ref}}(\frac{\partial\hat{\tau}_{xx}}{\partial \hat{x}}+\frac{\partial\hat{\tau}_{xy}}{\partial \hat{y}})=0. \quad (5)$$

where the reference Reynolds number, $Re_{ref}=\frac{\mu_{ref}}{x_{ref}\rho_{ref}u_{ref}}$.
μ_{ref} is obtained using the Reynolds number, which is pre-set during each computation to model the physical flow in external aerodynamics. In all the computations through out this work, the Reynolds number is based on the chord length of the airfoil.
Energy equation, in the absence of any external work due to the body force and internal heat generation, can be expressed as

$$\frac{\partial(\rho E)}{\partial t}+\frac{\partial(\rho uH)}{\partial x}+\frac{\partial(\rho vH)}{\partial y}-\frac{\partial(u\tau_{xx}+v\tau_{xy})}{\partial x}-\frac{\partial(u\tau_{xy}+v\tau_{yy})}{\partial y}+\frac{\partial(q_x)}{\partial x}+\frac{\partial(q_y)}{\partial y}=0,$$

where
$\tau_{xx}=2\mu\frac{\partial u}{\partial x}-\frac{2}{3}\mu(\frac{\partial u}{\partial x}+\frac{\partial v}{\partial y})$, $\tau_{xy}=\frac{\partial v}{\partial x}+\frac{\partial u}{\partial y}$.
$q_x=k\frac{\partial T}{\partial x}$, $q_y=k\frac{\partial T}{\partial y}$.
Substituting the heat flux vector and shear stress tensor in the energy equation and introducing reference values,

$$\begin{aligned}\frac{(\rho_{ref}E_{ref})}{t_{ref}}\frac{\partial(\hat{\rho}\hat{E})}{\partial t}+\frac{\rho_{ref}u_{ref}E_{ref}}{x_{ref}}\frac{\partial(\hat{\rho}\hat{u}\hat{H})}{\partial x}+\frac{\rho_{ref}u_{ref}E_{ref}}{x_{ref}}\frac{\partial(\hat{\rho}\hat{v}\hat{H})}{\partial y}\\ -\frac{u_{ref}^2\mu_{ref}}{x_{ref}^2}\frac{\partial(\hat{u}\hat{\tau}_{xx}+\hat{v}\hat{\tau}_{xy})}{\partial x})-\frac{u_{ref}^2\mu_{ref}}{x_{ref}^2}\frac{\partial(\hat{u}\hat{\tau}_{xy}+\hat{v}\hat{\tau}_{yy})}{\partial y})\\ +\frac{k_{ref}T_{ref}}{x_{ref}^2}\frac{\partial(\hat{q}_x)}{\partial x}+\frac{k_{ref}T_{ref}}{x_{ref}^2}\frac{\partial(\hat{q}_y)}{\partial y}=0,\end{aligned}$$

Dimensionally, $[E_{ref}]=[T_{ref}]$
Prandtl number, $Pr=\frac{\mu C_p}{k}$

Grouping the reference values with Reference Reynolds number and Prandtl number,

$$\Rightarrow \frac{\partial(\hat{\rho}\hat{E})}{\partial\hat{t}} + \frac{\partial(\hat{\rho}\hat{u}\hat{H})}{\partial\hat{x}} + \frac{\partial(\hat{\rho}\hat{v}\hat{H})}{\partial\hat{y}} - \frac{1}{Re_{ref}}\left(\frac{\partial(\hat{u}\hat{\tau}_{xx} + \hat{v}\hat{\tau}_{xy})}{\partial\hat{x}} + \frac{\partial(\hat{u}\hat{\tau}_{xy} + \hat{v}\hat{\tau}_{yy})}{\partial\hat{y}} - \frac{\hat{\mu}}{Pr}\left(\frac{\partial\hat{q}_x}{\partial\hat{x}} + \frac{\partial\hat{q}_y}{\partial\hat{y}}\right)\right) = 0. \tag{6}$$

Laminar Prandtl number has been set to 0.72.

The above derived non-dimensional form of the governing equation is used in numerical modelling as described in the subsequent chapters. The hat symbols used to denote the non-dimensional flow variables are dropped in the rest of the thesis for the sake of simplicity.

2.3 Turbulence Modelling

2.3.1 Physical nature of turbulence

Turbulence is a deterministic chaos [26] generated due to the fluctuation of the flow quantities, varying spatially as well as temporally over the average values and can be mathematically modelled [27]. These fluctuating components are physically interpreted as the spectrum of length scales cascading energy from the core region of the flow [28] to the viscous boundary wall to be dissipated as heat energy through friction.

2.3.2 Numerical modelling of turbulence

Broadly, the spectrum of the scales in a turbulent flow field, ranging from the smallest as determined by the Kolmogorov scale [29] to the largest as detected by the boundary layer thickness can be classified into three different regimes associated with different length scales. The flow in the core region interacts with the equivalent sized and comparatively larger length scale (integral scale [26]) to channelise energy into the inertial range, which contains eddies with moderate scale size. Kolmogorov's universal law of equilibrium is obeyed in this regime and the length scale is uniquely determined by the molecular viscosity and the rate of energy dissipation. The energy from the inertial range is cascaded into the eddy structures with the smallest scale size (dissipation scale [26]) and the flow phenomena is governed by molecular dissipation.

In the range of larger length scale, the eddies are anisotropic and governed by the orientation of the mean flow. They are dominant in the part of the flow domain away from the solid wall due to their interaction with the mean flow to extract energy for transferring to smaller eddies. They are physically present in the form of large separation bubbles or wakes in the flow field. The energy is dissipated near the viscous solid wall. Hence, the energy is channelised through the spectrum of the eddies away from the wall to the region of the solid wall. The small scale eddies near the wall responsible for converting the flow energy to heat as a result of friction due to the molecular viscosity are isotropic as the diffusion phenomenon has no preferred direction.

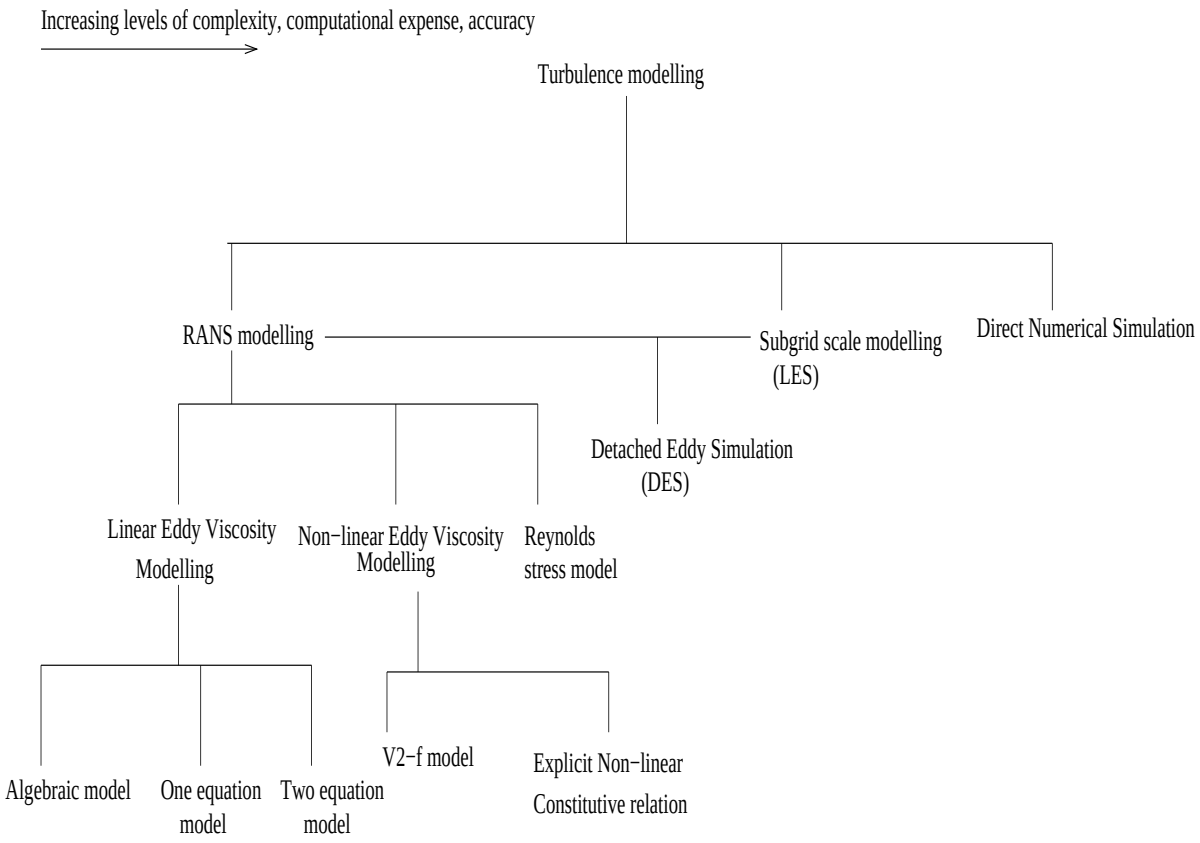

Figure 4: Numerical modelling of the turbulent flow

Depending upon the required computational effort and numerical resolution of the eddies, modelling of the turbulent flow can be broadly classified into three different categories.

In the Direct Numerical Simulation (DNS), the whole spectrum of the turbulent scale is resolved by the grid. The grid needs to be finely refined in order to capture the smallest length scale in the dissipation range.. Hence, the number of points in every direction, $\frac{1}{\lambda} = Re^{\frac{3}{4}}$. The number of points in the grid becomes, $N_p = Re^{\frac{9}{4}}$. for a three-dimensional computational domain. The number of grid points increases significantly with the increase in the Reynolds numbers. The computational expense associated with the DNS model becomes the constraint due to the grid size requirements, as the external aerodynamical flows deal with relatively high Reynolds number.

In the Large Eddy Simulation (LES), spatial averaging is used in the form of a grid filter to capture the components of the solution with larger length scale in comparison to the grid size, and the smaller length scales are explicitly modelled using Sub-grid Scale Modelling (SGS). Grid near the solid boundary has to be isotropically refined to capture all the length scales. Though the requirement of the number of grid points is comparatively lesser than the requirement in using DNS model, still it is prohibitively high for large scale industrial applications.

In Reynolds Averaged Navier-Stokes equation (RANS), all the turbulent scales are meant to be captured through numerical modelling. Ideally, the grid is designed to capture the variation

in the mean flow component rather than any turbulent length scales. As the variation in the mean flow quantities are significant along the normal direction near the wall, high aspect ratio cells are used to capture the boundary layer. The technique to model the eddy viscosity from the mean flow components is the prime factor determining the accuracy and the computational expense of the RANS model.

2.3.3 Reynolds stress modelling through LEVM

The instantaneous component of a conservative quantity can be expressed as the sum of the average quantity and the fluctuating part.

$$Q(x,t) = \frac{1}{\Delta t}\int_{t}^{t+\Delta t}(\bar{Q}(x,t) + q(x,t))dt$$

When the time scale of fluctuation is very small compared to the computational timestep, the fluctuating part is averaged out to null and only the mean component is captured. During this method of Reynolds averaging, the linear terms in the governing equations (Eqn. 1) contribute to the numerical solution through the averaged quantities, but the non-linear terms have an additional component, expressed as the product of the two fluctuating flow quantities. Such a term present in the momentum equation is called the *Reynolds stress tensor* and in the energy equation, due to the scalar form is termed as the *Reynolds flux vector*.

Boussinesq hypothesis is used to linearly correlate the Reynolds stress tensor with the mean flow quantities during turbulence modelling through the introduction of Eddy viscosity. This process is called as the Linear Eddy Viscosity Modelling (LEVM).

$$-\rho\overline{V^{'}\otimes V^{'}} = \mu_t(\nabla V + (\nabla V)^T) - \frac{2}{3}I(\nabla\cdot V) - \frac{2}{3}I(\rho k). \tag{7}$$

k is the turbulent kinetic energy.

The product of the fluctuating components present in the transportation of the total internal energy in Eqn. (2) is modelled

$$-\rho\overline{V^{'}E^{'}} = k_t\nabla E,$$

where, $k_t = \dfrac{\mu_t}{Pr_t}$, Pr_t is the turbulent Prandtl number and the value is set to 0.90 for all the computation.

μ_t is the eddy viscosity and quantifies the turbulence in the flow field. Unlike dynamic viscosity, which is a fluid property, eddy viscosity is a flow property and depends on the flow field. This unknown eddy viscosity is obtained by solving the turbulent flow quantities.

2.3.4 Detached Eddy Simulation

When the time scale of certain turbulent eddies becomes larger than the unsteady timestep used in the numerical simulation, a part of the fluctuating component related to the low frequency

end of the solution is captured along with the mean flow quantities through grid resolution. This causes the dual inclusion of the fluctuating term as the component is modelled through the turbulent equations using LEVM. This leads to a modelling error during numerical evaluation, specifically for unsteady flow simulation with RANS, where the restriction in the numerical timestep makes it comparable to the time scale of certain eddies. As large spatial scale of the turbulent eddies are associated with larger time scale of fluctuation, the problem is encountered due to the presence of massively separated flow in the computational domain.

This drawback of RANS in imposing a limitation for accurately resolving and modelling the turbulent scales in the region of massive separation has also been reported by Franke *et al* [30]. In order to enhance the applicability of RANS Simulation, Rung [15, 31] suggests the ratio between the grid resolved timescale (T_m) and modelled turbulent timescale (T_t) should satisfy the condition based on the Reynolds number and the Stanton number. $\frac{T_m}{T_t} \approx \gamma \frac{Re^{\frac{1}{5}}}{St}$, where $\gamma = [1, 10]$ in the boundary layer; $\gamma = [0.1, 1]$ in the free shear layer. The results obtained with a modified k-ω model [32] on a high-lift configuration has shown improvement compared to the standard model [15]. In contrary, LES, being a spatially averaged model and able to distinguish the grid filtered component of the solution from the numerically modelled part, does not suffer from this drawback [38]. Inspite of this advantage, the applicability of the LES is restricted due to the requirement of prohibitively high grid resolution in the near wall region.

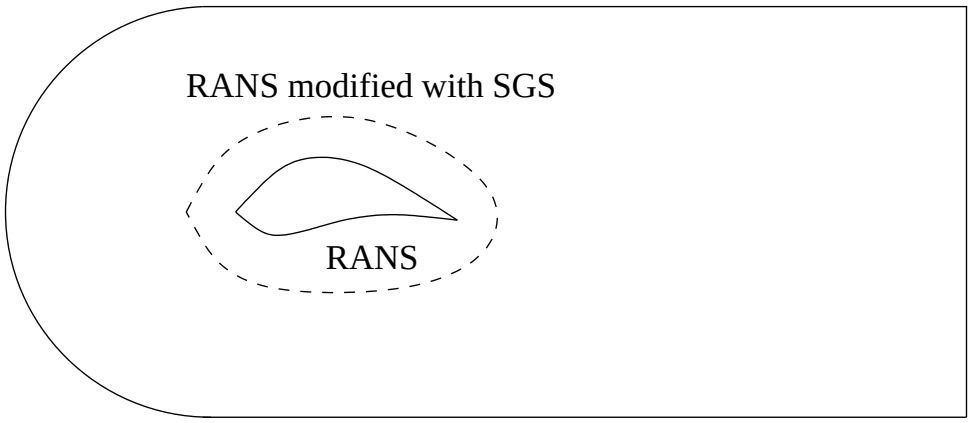

Figure 5: Numerical models used in the computational domain for Zonal DES

Hence, using RANS for the boundary layer simulation and LES in the region far-away from the wall as suggested by Spalart [27], one can effectively blend the strengths of both the models. A boundary in the computational domain in percentage of the chord length separating the RANS region from the LES region is prescribed a priori, thus making it equivalent to the Zonal DES [34]. The effect of the dimension of the specified boundary to separate the two regions on the accuracy of the solution is discussed in the result section 3.1.3.

Several researchers have successfully tried to utilise the benefit of RANS and Large Eddy Simulation (LES) by effectively combining them to create a series of hybrid models for the kinds

of flow dominated by separation [35–41] and unsteadiness [42]. These successful studies conducted in the recent years by various researchers for using the DES in simulating unsteady and massively separated flows affirms the decision to use the model.

2.3.5 Spalart-Allmaras model and modification for DES

Flow is assumed to be fully turbulent without undergoing any transition for all the computations demonstrated in this work. Turbulence in the computational domain is modelled with one-equation Spalart-Allmaras model [43] which solves a transport equation of an intermediate variable($\bar{\nu}$).

$$\frac{D\bar{\nu}}{Dt} = \frac{1}{\sigma}(\nabla\cdot((\nu+\bar{\nu})\nabla\bar{\nu}+c_{b2}(\nabla(\bar{\nu}))^2)) + c_{b1}\bar{S}\bar{\nu} - c_{w1}f_w(\frac{\bar{\nu}}{d})^2, \tag{8}$$

where the terms on the right hand side of the equation model the contributions from the diffusion, production and destruction phenomena. .
$\bar{S} = S + \frac{\bar{\nu}}{(\kappa d)^2}f_{v2}$, where the scalar quantity S derived from the shear strain rate tensor

$$S = \sqrt{((\frac{\partial w}{\partial y} - \frac{\partial v}{\partial z})^2 + (\frac{\partial u}{\partial z} - \frac{\partial w}{\partial x})^2 + (\frac{\partial u}{\partial y} - \frac{\partial v}{\partial x})^2)}.$$

f_{v1} and f_{v2} are defined as,
$f_{v1} = \frac{\chi^3}{\chi^3 + c_{v1}^3}, \chi = \frac{\bar{\nu}}{\nu},$
$f_{v2} = 1 - \frac{\chi}{1+\chi f_{v1}},$
Auxiliary functions are defined as, $f_w = g(\frac{1+c_{w3}^6}{g^6+c_{w3}^6})^{\frac{1}{6}}$, $g = r + c_{w2}(r^6 - r), r = \frac{\bar{\nu}}{\bar{S}\kappa^2 d^2}$
The closure constants are $c_{b1} = 0.1355$, $\sigma = \frac{2}{3}$, $c_{b2} = 0.622$, $\kappa = 0.41$, $c_{w2} = 0.3$, $c_{w3} = 0.3$, $c_{v1} = 0.3$, $c_{w1} = \frac{c_{b1}}{\kappa^2} + \frac{1+c_{b2}}{\sigma}$.
After solving the transport equation numerically, the turbulent viscosity is obtained by using, $\nu_t = \bar{\nu} f_{v1}$.

For DES, the wall distance is modified as suggested by Spalart [35],

$$d = \begin{cases} Unchanged & \text{if } d_w < K_w \times C; \\ 0.65 \times max(\Delta x, \Delta y) & \text{if } d_w \geq 0.1 \times C\ . \end{cases}$$

where d_w is the actual distance of the cell center from the wall. Δx and Δy are the grid dimensions in the Cartesian coordinate directions. The effectiveness of the model in the modification of the wall distance is based on the required presence of the uni-directionally stretched near wall grid cells, which prevents any wall distance being modified near the wall region. This restriction exactly fits to the requirement of high Reynolds number turbulent flow simulation, where the grid near the boundary layer is stretched in the flow direction to

capture the high gradients of mean flow quantities along the normal direction to the wall. Away from the solid boundary, the largest dimension of the grid cell becomes smaller than the actually estimated wall distance and the wall distance undergoes modification. This modification results in increasing the dissipation as the destruction term present in the original S-A model is increased. In the outer region, away from the solid wall, the model with DES modification is proved to be reduced to Smagorinsky LES model [35]. In order to prohibit the SGS modification from entering into the RANS zone, grids with right kind of variation in the coordinate directions have to be specifically designed [33].

To ensure the effectiveness of LES at a relatively larger distance from the wall, the dimensional characteristic of the grid needs to be controlled by the flow which is usually comprised of relatively larger and isotropic scales. In order to satisfy the imposed condition on the grid generation, the initial grid used is relatively stretched near the wall but dimensionally isotropic away from the wall. As Quadflow uses adaptivity, the grid is automatically refined in those regions detected by the activity in the flow field but still maintaining their aspect ratios. In the outer region, away from the solid wall, the adapted grid maintains its isotropic nature after the grid adaptation and able to capture the high energy isotropic turbulent scales which are dimensionally similar and interacting with the mean flow. Adaptation decreases the wall distance of the grid cells in the vicinity of the boundary and improves the grid quality in improved capturing of the flow variation. Hence, the grid adaptation is naturally complementary to the DES modelling for improving the accuracy of the numerical simulation.

2.3.6 Wall distance computation

Computations have been performed using Spalart-Allmaras' one equation RANS model and its variant, modified DES model to effectively capture the turbulent scales. The specification of number of cells and the stretching ratio control the grid resolution in the boundary layer. The approach is similar to the Low Reynolds number modelling, where the grid cells near the solid wall are refined to capture the turbulent flow field rather than any utilisation of explicit models in the form of *wall function* [44].

The wall distance keeps on decreasing with every successive grid adaptation and the improved resolution of the boundary layer flow enhances the accuracy of the solution. Hence, the method to compute the wall distance becomes critical as the normal distance from the cell center to the wall becomes smaller with each grid adaptation level. Special care is taken, as explained below, in order to compute the wall distance in the presence of highly stretched adapted grid near the wall.

$\vec{r}$ is the position vector of a point on the solid boundary from the center of the cell whose wall distance needs to be computed. The estimated wall distance, expressed in the form of the magnitude of the $\vec{r}$ needs to be minimised to ensure the proximity of the cell from the obtained

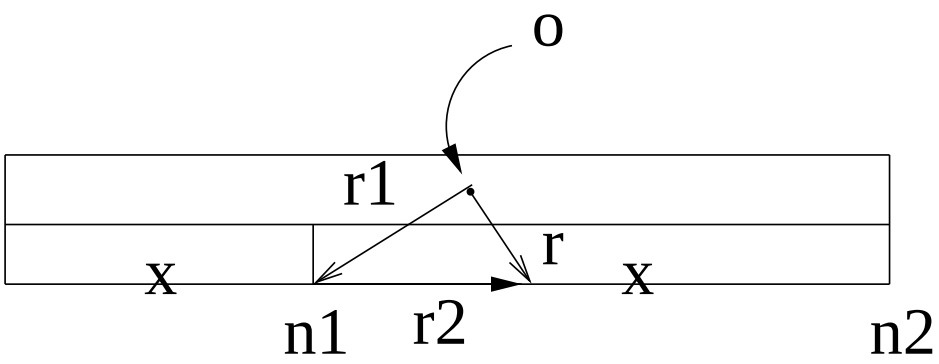

Figure 6: Vectorial estimation of the wall distance

location of the solid wall. Vectorially it is expressed as

$$\vec{r} = \vec{r}_1 + \sigma\vec{r}_2, \tag{9}$$

where $\vec{r}_1, \vec{r}_2$ are the position vectors of the nodes and σ is the free parameter needs to be optimised for obtaining the minimum distance.
$|\vec{r}|$ is minimum when

$$\sigma = \frac{-(\vec{r}_1.\vec{r}_2)}{(\vec{r}_2.\vec{r}_2)} \tag{10}$$

The extension of the method to determine the wall distance for three-dimensional computation is similar.

2.4 Time integration scheme

The development of the flow field during computation is a two step process, namely *reconstruction* and *evolution*. The reconstruction process determines the spatial accuracy of the scheme and is detailed in the section 2.6. The current section describes the numerical schemes used for the temporal evolution of the flow field.
Backward-Euler and its modification to a two step time integration scheme suggested by Batten and Leschziner [45] have been used for steady state flow simulations. The above mentioned implicit schemes are theoretically unconditionally stable and allow considerably large CFL numbers to be used during computations, thus reducing the simulation time. These schemes are first order accurate in time and rapid numerical convergence is achieved with the use of local time-stepping. Despite the limitation imposed by the CFL condition, explicit time integration scheme based on the Runge-Kutta method is implemented. The scheme has the advantage of reduced requirement of the memory space over the implicit scheme during computation. The construction and storage of the Jacobian matrix in the implicit formulation requires a huge Random Access Memory (RAM) space and proves to be a bottleneck especially in three-dimensional flow simulation, where the number of cells in the computational domain increases significantly

as a result of grid adaptation. Multigrid method has been implemented in the explicit time integration scheme to improve the convergence behaviour.

A time integration scheme based on the second order backward difference discretisation is numerically formulated using the control volume approach. The scheme is utilised in simulating unsteady flow field arising out of the movement of the rigid body in the presence of grid adaptation. The scheme is shown to be accurate and demonstrated to be more robust compared to a previously implemented unsteady time integration scheme using the mid-point method [25].

2.4.1 Scheme for steady flow simulation

Preconditioned Navier-Stokes equations for the stationary grid can be written as

$$\Gamma_c \int_{\Omega(t)} \frac{\partial Q}{\partial t} d\Omega + \int_{\partial\Omega(t)} [F_c - F_v] \cdot n dA = 0$$

where Γ_c is the preconditioning matrix defined for the conservative variables.

F_c and F_v represent the inviscid and viscous flux vectors respectively. In implicit form, the residual is to be evaluated at the $(n+1)^{th}$ timestep. Thus,

$$\Gamma_c \int_{\Omega(t)} \frac{\partial Q}{\partial t} d\Omega + Res(Q^{n+1}) = 0$$

The above equation after Newton linearisation (further explained in the section 2.9) and numerical discretisation gives

$$\Gamma_c \frac{\Delta Q_i^n}{\Delta t} \Omega_i + \frac{\partial}{\partial Q}(Res(Q^n))\Delta Q^n + Res(Q^n) = 0$$

After rearrangement of the terms,

$$[\Gamma_c \frac{I}{\Delta t}\Omega + \frac{\partial}{\partial Q} Res(Q^n)]\Delta Q^n = -Res(Q^n)$$

$$\Delta Q^n = -J^{-1} Res(Q^n) \tag{11}$$

where

$$J = [\Gamma_c \frac{I}{\Delta t}\Omega + \frac{\partial}{\partial Q} Res(Q^n)]$$

Eqn. (11) represents the implicit numerical formulation of the Navier-Stokes equations, which is solved using the *Backward-Euler* time integration process. $B_1(Q^n, \Delta t)$ is a single iteration step in Eqn. (11) and the formulation is symbolically represented as shown in Eqn. (12).

$$\Delta Q^n = B_1(Q^n, \Delta t)) \tag{12}$$

Jacobian matrix arising out of the linearisation process can be numerically or analytically constructed (explained in section 2.8) and is used to build the preconditioning matrix required for

solving the system of linear equations. A two step time integration scheme (B2), originally developed by Batten and Leschziner [45], as a modification to the Backward Euler scheme has been implemented. A provisional solution is derived in the predictor step which is numerically equivalent to the Backward-Euler scheme with reduced timestep. The predicted solution is corrected to obtain the final solution at the second stage of the time integration process. The possibility of using higher CFL numbers in the B2 scheme for identical computational problems demonstrates a higher degree of robustness of the scheme compared to the Backward-Euler scheme.

$$\delta\overline{Q} = B1(Q^n, \frac{\delta t}{2}), \overline{Q} = Q^n + \delta\overline{Q} \tag{13}$$

$$\delta\overline{Q} = B1(\overline{Q}, \delta t), \overline{Q}^{n+1} = \overline{Q} + \frac{\delta\overline{Q}}{2} \tag{14}$$

The scheme is observed to suppress the chattering induced by the limiter and results in improving the convergence behaviour without affecting the solution accuracy.

2.4.2 Moving grid formulation

One of the prime objectives of the Quadflow solver is to use it as a CFD tool in aeroelastic applications. The section outlines the derivation of the numerical formulation to address Arbitrary-Lagrangian-Eulerian problems (ALE) on the foundation of the first principle of differentiation considering the movement of the solid body in the computational domain. The movement of the solid wall enforces a deformation in the computational domain and the control volume of the grid cells undergoes a change with time. The change in the control volume of the grid cells can be expressed as the velocity of the nodes constituting the control cell, as explained in [7]. The numerical scheme is modified to take into account the nodal velocities when dealing with the problem involving the rigid body movement. The physical significance of various terms arising out of the derivation is also explained. Let, f is a conservative quantity transported into the control volume due to the relative motion between the fluid and the control surfaces.
Using the first principle of the differentiation,

$$\frac{d}{dt}(\int_{\Omega(t)} f(r,t)d\Omega) = \lim_{\Delta t\to 0} \frac{\int_{\Omega(t+\Delta t)} f(r+\Delta r, t+\Delta t)d\Omega - \int_{\Omega(t)} f(r,t)d\Omega}{\Delta t}$$

the substantial derivative takes both the spatial and temporal changes of the conservative quantity into account.
Using Taylors series expansion and neglecting the higher order terms,

$$= \lim_{\Delta t\to 0} \frac{\int_{\Omega(t)} (f(r,t) + \nabla f \cdot \Delta r + \frac{\partial f(r,t)}{\partial t}\Delta t)d\Omega - \int_{\Omega(t)} f(r,t)d\Omega}{\Delta t}$$

$$= \lim_{\Delta t\to 0} \frac{1}{\Delta t} \int_{\Omega(t)} \nabla f \cdot \Delta r d\Omega + \int_{\Omega(t)} \frac{\partial f(r,t)}{\partial t} d\Omega]$$

$$= \int_{\Omega(t)} \nabla f \cdot V d\Omega + \int_{\Omega(t)} \frac{\partial f(r,t)}{\partial t} d\Omega$$

$$= \int_{\Omega(t)} \nabla(fV) d\Omega - \int_{\Omega(t)} f\nabla(V) d\Omega + \int_{\Omega(t)} \frac{\partial}{\partial t} f(r,t) d\Omega$$

Using Reynolds transport theorem,

$$\int_{\Omega(t)} \nabla(fV) d\Omega = \oint_{\partial\Omega(t)} fV \cdot nds$$

From the conservation of the control volume,

$$\nabla(V) d\Omega = -\frac{\partial}{\partial t}(d\Omega).$$

The negative sign appears as the velocity of the incoming fluid responsible for increasing the control volume is directionally opposite to the normal of the control surface.

$$\frac{d}{dt}(\int_{\Omega(t)} f(r,t) d\Omega) = \oint_{\partial\Omega(t)} fV \cdot nds + \int_{\Omega(t)} f\frac{\partial}{\partial t}(d\Omega) + \int_{\Omega(t)} \frac{\partial}{\partial t} f(r,t) d\Omega$$

Thus the final equation takes the form,

$$\frac{d}{dt}(\int_{\Omega(t)} f(r,t) d\Omega) = \oint_{\partial\Omega(t)} fV \cdot nds - \oint_{\partial\Omega(t)} fV_g \cdot nds + \int_{\Omega(t)} \frac{\partial}{\partial t} f(r,t) d\Omega \tag{15}$$

2.4.3 Scheme for unsteady flow simulation

2.4.3.1 Backward Difference Scheme Euler equation, in the implicit conservative form can be expressed as

$$\frac{\partial}{\partial t} \int_{\Omega(t)} Q d\Omega + Res^{k+1} = 0. \tag{16}$$

$\Omega(t)$ is a small segment in the computational domain enclosed by the surface $\partial\Omega(t)$, representing the single control volume in the following derivation.
Applying chain rule [83] in Eqn. (16)

$$\int_{\Omega(t)} \frac{\partial Q}{\partial t} d\Omega + \int_{\Omega(t)} Q\frac{\partial}{\partial t}(d\Omega) + Res^{k+1} = 0. \tag{17}$$

Using Beam-Warming second order temporal discretisation for the time derivative terms

$$\int_{\Omega(t)} (\frac{3Q^{k+1} - 4Q^n + Q^{n-1}}{2\triangle t}) d\Omega + \int_{\Omega(t)} Q(\frac{3d\Omega^{n+1} - 4d\Omega^n + d\Omega^{n-1}}{2\triangle t}) + Res^{k+1} = 0 \tag{18}$$

Where $n-1$, n and $n+1$ represent the physical timesteps and k denotes the index for Newton iteration.

Linearisation of the residual gives,

$$\begin{aligned} Res^{k+1} &= Res^k + \frac{\partial}{\partial Q}(Res^k)\triangle Q^k \\ &= \oint_{\partial\Omega_{t_{n+1}}} F_c(Q^k)\cdot n_{n+1} ds + \frac{\partial}{\partial Q}(Res^k)\triangle Q^k. \end{aligned}$$

Substituting the linearised residual and rearranging the terms in the Eqn. (18)

$$\begin{aligned} &\int_{\Omega(t)} (\frac{(3Q^{k+1}-3Q^k)+(3Q^k-3Q^n)-(Q^n-Q^{n-1})}{2\triangle t}) d\Omega \\ &\quad + \int_{\Omega(t)} Q(\frac{(3d\Omega^{n+1}-3d\Omega^n)-(d\Omega^n-d\Omega^{n-1})}{2\triangle t}) \\ &\quad + \oint_{\partial\Omega_{t_{n+1}}} F_c(Q^k)\cdot n_{n+1} ds + \frac{\partial}{\partial Q}(Res^k)\triangle Q^k = 0. \end{aligned} \tag{19}$$

Rearranging the terms and using the notation "$\triangle$" for forward difference,

$$\begin{aligned} &\int_{\Omega(t)} \frac{3}{2}\frac{\triangle Q^k}{\triangle t} d\Omega + \int_{\Omega(t)} \frac{3}{2\triangle t}(Q^k - Q^n) d\Omega - \int_{\Omega(t)} \frac{1}{2\triangle t}(Q^n - Q^{n-1}) d\Omega \\ &\quad + \int_{\Omega(t)} Q\frac{3}{2}\frac{\triangle(d\Omega^n)}{\triangle t} - \int_{\Omega(t)} Q\frac{1}{2}\frac{\triangle(d\Omega^{n-1})}{\triangle t} \\ &\quad + \oint_{\partial\Omega_{t_{n+1}}} F_c(Q^k)\cdot n_{n+1} ds + \frac{\partial}{\partial Q}(Res^k)\triangle Q^k = 0. \end{aligned} \tag{20}$$

The vector of conservative variables can be taken outside of the volume integral as it represents the solution vector at the cell center of the control volume and can be held as a constant inside the cell. The proposition is based on the satisfaction of *conservativity condition* of the Finite Volume method.

$$\begin{aligned} &\frac{3}{2\triangle t}\Omega^{n+1}\triangle Q^k + (\frac{3}{2\triangle t}Q^k\Omega^{n+1} - \frac{4}{2\triangle t}Q^n\Omega^n + \frac{Q^{n-1}\Omega^{n-1}}{2\triangle t}) \\ &\quad + \int_{\Omega(t)} Q\frac{3}{2}\frac{\triangle(d\Omega^n)}{\triangle t} - \int_{\Omega(t)} Q\frac{1}{2}\frac{\triangle(d\Omega^{n-1})}{\triangle t} \\ &\quad + \oint_{\partial\Omega_{t_{n+1}}} F_c(Q^k)\cdot n_{n+1} ds + \frac{\partial}{\partial Q}(Res^k)\triangle Q^k = 0. \end{aligned} \tag{21}$$

The change in the control volume can be expressed in the term of grid velocities of the control surfaces, using Eqn. (24). Hence, the Eqn. (21) becomes,

$$\begin{aligned} &\frac{3}{2\triangle t}\Omega^{n+1}\triangle Q^k + (\frac{3}{2\triangle t}Q^k\Omega^{n+1} - \frac{4}{2\triangle t}Q^n\Omega^n + \frac{Q^{n-1}\Omega^{n-1}}{2\triangle t}) \\ &\quad - \frac{3}{2}\oint_{\partial\Omega_{t_{n+1}}} Q^k V_{g_n}\cdot n_{n+1} ds + \frac{1}{2}\oint_{\partial\Omega_{t_n}} Q^{n-\frac{1}{2}} V_{g_{n-1}}\cdot n_n ds \\ &\quad + \oint_{\partial\Omega_{t_{n+1}}} F_c(Q^k)\cdot n_{n+1} ds + \frac{\partial}{\partial Q}(Res^k)\triangle Q^k = 0. \end{aligned} \tag{22}$$

$V_{g_{n-1}}$ and V_{g_n} are the grid velocities computed for the existing Mid-point scheme using the method described by Lamby [7] and correspond to $(n-1)^{th}$ and n^{th} timesteps, respectively. Rearranging the terms,

$$[\mathbf{I}\frac{3\Omega^{n+1}}{2\triangle t}+\frac{\partial}{\partial Q}(Res^k)]\triangle Q^k+(\frac{3}{2\triangle t}Q^k\Omega^k-\frac{4}{2\triangle t}Q^n\Omega^n+\frac{1}{2\triangle t}Q^{n-1}\Omega^{n-1})$$
$$+\oint_{\partial\Omega_{t_{n+1}}}(F_c(Q^k)-\frac{3}{2}Q^kV_{g_n})\cdot n_{n+1}ds+\oint_{\partial\Omega_{t_n}}\frac{1}{2}Q^{n-\frac{1}{2}}V_{g_{n-1}}\cdot n_n ds=0$$

Substituting $\frac{3}{2}V_g=V_g^m$ for convenience,

$$[\mathbf{I}\frac{3\Omega^{n+1}}{2\triangle t}+\frac{\partial}{\partial Q}(Res^k)]\triangle Q^k$$
$$=-\oint_{\partial\Omega_{t_{n+1}}}(F_c(Q^k)-Q^kV_{g_n}^m)\cdot n_{n+1}ds-\frac{1}{2}\oint_{\partial\Omega_{t_n}}Q^{n-\frac{1}{2}}V_{g_{n-1}}\cdot n_n ds$$
$$-(\frac{3}{2\triangle t}Q^k\Omega^k-\frac{4}{2\triangle t}Q^n\Omega^n+\frac{1}{2\triangle t}Q^{n-1}\Omega^{n-1}) \tag{23}$$

V_{g_n} is the component of the grid velocity along the normal direction to the face, which is computed during the grid deformation at the beginning of every timestep. Assuming the grid velocity is constant in a time interval, the variation of the control volume in two dimensions will be quadratic with respect to time. Thus a single Gauss point in the temporal direction at the mid point of the time interval is sufficient to relate the grid velocity with the change in the control volume using the numerical integration given by Eqn. (24). Expressing numerically,

$$\int_{\Omega(t)}\frac{\triangle d\Omega^n}{\triangle t}=\sum_{i=1}^{n_s}V_{g_{n_i}}\cdot n_{(n+\frac{1}{2})_i}ds_i, \tag{24}$$

where $\triangle d\Omega^n$ is the change in a small segment of a single control volume enclosed by $\partial\Omega_{t_{n+\frac{1}{2}}}$ and $V_{g_{n_i}}$ is the grid velocity corresponding to the surface i. n_s is the number of surfaces enclosing the control volume.

In three-dimensional computation, two Gaussian quadrature points with appropriate weightage is needed for the numerical integration of Eqn. (24) for resolving the cubical variation in the control volume with respect to time.

Eqn. (23) is valid for the complete computational domain undergoing a change in the control volume due to the movement of a rigid body inside the domain and also, in the presence of grid adaptation.

The subsequent section proves the derived numerical scheme satisfying the *Geometric Conservation Law*.

2.4.3.2 Proof of satisfaction of Geometric Conservation Law A valid unsteady time integration scheme has to necessarily satisfy the geometric conservation law in order to be a

"cell-volume-preserving finite-volume scheme" [56] for solving the Arbitrary Lagrangian Eulerian (ALE) problems. It eliminates numerical oscillations and preserves physical conservation laws for solutions on moving meshes.

The geometric conservation law states that the uniform flow field remains unchanged in the presence of movement of the boundaries of the computational domain. In this subsection, the invariance of the uniform flow field in the computational domain with deforming boundaries is shown to be satisfied by the currently derived scheme.

Discretisation with Implicit Backward Difference scheme gives

$$[\mathbf{I}\frac{3\Omega^{n+1}}{2\triangle t}+\frac{\partial}{\partial Q}(Res^k)]\triangle Q^k = R, \tag{25}$$

where

$$\begin{aligned} R \;\; = & -\oint_{\partial\Omega_{t_{n+1}}}(F_c(Q^k)-Q^k(\frac{3}{2})V_{g_n})\cdot n_{n+1}ds-\frac{1}{2}\oint_{\partial\Omega_{t_n}}Q^{n-\frac{1}{2}}V_{g_{n-1}}\cdot n_n ds \\ & -(\frac{3}{2\triangle t}Q^k\Omega^{n+1}-\frac{4}{2\triangle t}Q^n\Omega^n+\frac{1}{2\triangle t}Q^{n-1}\Omega^{n-1}). \end{aligned} \tag{26}$$

For a uniform flow field

$$\begin{aligned} R_\infty = -F_c(Q_\infty)\oint_{\partial\Omega_{t_{n+1}}}n_{n+1}ds+Q_\infty\frac{3}{2}\oint_{\partial\Omega_{t_{n+1}}}V_{g_n}\cdot n_{n+1}ds \\ -\frac{1}{2}Q_\infty\oint_{\partial\Omega_{t_n}}V_{g_{n-1}}\cdot n_n ds-(\frac{3}{2\triangle t}Q_\infty\Omega^{n+1}-\frac{4}{2\triangle t}Q_\infty\Omega^n+\frac{1}{2\triangle t}Q_\infty\Omega^{n-1}). \end{aligned} \tag{27}$$

After rearranging the terms

$$\begin{aligned} \Rightarrow R_\infty = \frac{3}{2}Q_\infty\frac{\Omega^{n+1}-\Omega^n}{\triangle t}-\frac{1}{2}Q_\infty(\frac{\Omega^{n+1}-\Omega^n}{\triangle t}) \\ -(\frac{3}{2\triangle t}Q_\infty\Omega^{n+1}-\frac{4}{2\triangle t}Q_\infty\Omega^n+\frac{1}{2\triangle t}Q_\infty\Omega^{n-1}). \end{aligned} \tag{28}$$

$\Rightarrow R_\infty = 0.$

2.4.3.3 Implementation The integral term, $\oint_{\partial\Omega_{t_n}}Q^{n-\frac{1}{2}}V_{g_{n-1}}\cdot n_n ds$ present in the Eqn. (26) is resulted from the Beam-Warming discretisation of control volume which is essential for the satisfaction of the GCL.

Numerically

$\oint_{\partial\Omega_{t_n}}Q^{n-\frac{1}{2}}V_{g_{n-1}}\cdot n_n ds = Q^{n-\frac{1}{2}}\frac{(\Omega^n-\Omega^{n-1})}{\triangle t}$, where $Q^{n-\frac{1}{2}}=(\frac{Q^n+Q^{n-1}}{2})$

For unsteady simulation in the absence of the grid movement, the term is reduced to null.

The above derived formulation of the backward difference scheme can be implemented without any further complexity for the flow problems with moving boundaries without grid adaptation. But as Quadflow is conceptually based on the grid adaptation technique, certain specific modifications are essential for the sake of implementation. The complexity arises because of the requirement of the information at the $(n-1)_{th}$ time level. These quantities appear as the terms, $\frac{Q^{n-1}\Omega^{n-1}}{2\triangle t}$ and $\oint_{\partial\Omega_{t_n}} Q^{n-\frac{1}{2}} V_{g_{n-1}} \cdot n_n ds$ in the Eqn. (23). The cells in the domain undergo refinement or coarsening during grid adaptation resulting in the change of the grid topology between the time levels t_{n-1} and t_{n+1}. Hence, the cells at the time t_{n-1} are no longer present in the domain at t_{n+1}. Thus, the connectivity between the cells in the domain g^a_{n-1} is established with the cells belonging to the domain at g_{n+1} in order to obtain the quantities at $(n-1)_{th}$ in Eqn. (23).

The k_{th} and n_{th} terms in Eqn. (23) depend on the grid and flow variables corresponding to the time t_{n+1} and t_n respectively and hence, are directly available.

Searching algorithm

The grid topology undergoes a change during adaptation. The cells in the past grid domain corresponding to the cells in the present grid domain is searched using the method described in the section, as illustrated in the schematic diagram Fig. 7. The rectangular block represents

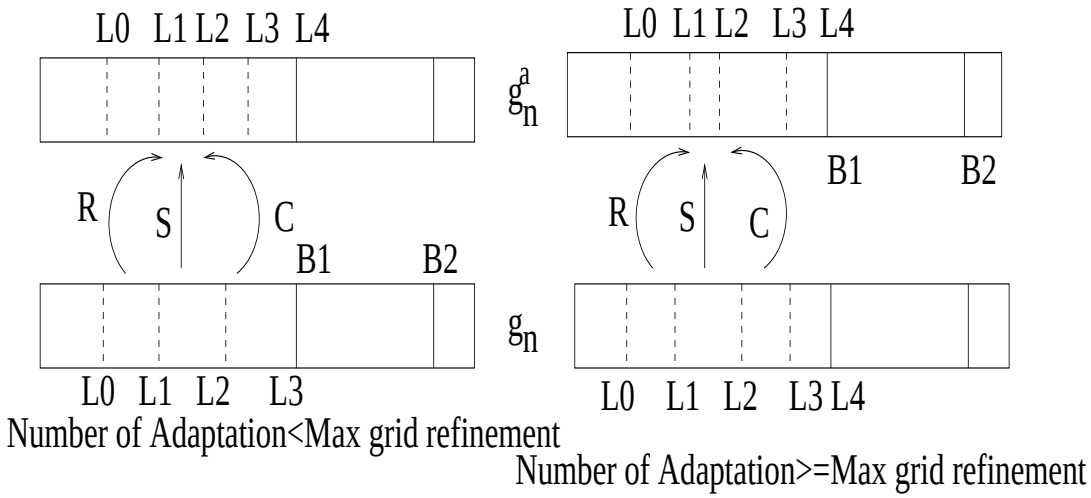

Figure 7: Possible forms of modification in the control volume due to grid adaptation

the storage of the cells in block and level wise manner denoted as ”B” and ” L” respectively. All the cells belonging to the first block are stored in the segment of the array marked by the line ”B1”. Inside the block, the cells are categorised according to the level information and stored in the segments as shown by dotted lines, L_0, L_1, $\ldots L_n$, representing the grid levels. The cells subjected to the refinement process (the operation is denoted as ”R” in Fig. 7) undergo a unit increase in their level and during coarsening, the level of the cells is decreased by a unit (denoted as ”C” in Fig. 7). The level information remains unchanged if the cell is subjected to neither refinement nor coarsening. The magnitude of jump in the grid level of the cells during a

single adaptation process is always restricted to unit. In addition to that, the adaptation criterion also restricts the difference between the level of the cell with all the surrounding neighbours to unit in order to prevent a drastic variation in the cell size in the regions of grid adaptation.

The grid adaptation can raise two distinct possibilities. If the prescribed maximum level of refinement has already been reached then the maximum number of levels in which cells can possibly stay remain same in the next adaptation, though cells can undergo alteration of their levels in the domain. This has been shown in the right side of Fig. 7. Otherwise, cells with one level higher values will be created after adaptation as represented in the left hand side of Fig. 7. Interblock cell transfer is avoided during grid adaptation and newly generated cells are always confined to the same block as their parent cell. Thus, the search is more efficient in the block-wise manner.

Cells at any level in a particular block belonging to the recent grid domain can correspond to the cells either in the same level or in one successive level or in one predecessive level of the same block in the previous grid domain depending upon whether the cell remains unchanged or coarsened or refined, respectively. The association between them can be found out by comparing the level and index information which is specific to an individual cell.

There are three different and distinct possibilities of transformation, a cell can undergo during grid adaptation, as considered below by two different possible cases.

Procedure for coarsened and unmodified cells

The schematic diagram in Fig. 8 shows the sequence of operations, the control volume cells are subjected to during the refinement process of grid adaptation. The grid represented as g^a_{n-1} undergoes deformation at time t^{n-1} and a new grid (g_n) with modified control volumes is obtained. The grid topology remains unchanged during the operation. The grid velocity $V_{g_{n-1}}$ at t^{n-1} is estimated.

At time t_n, the grid (g_n) is subjected to the coarsening process of adaptation, where four control volumes are agglomerated to create a single cell in the domain represented by g^a_n. The grid topology changes during the operation, but the volume remains unmodified. The grid velocity V_{g_n} at t^n is estimated from the change in the control volume, during the deformation of the grid from g^a_n to g_{n+1}. Newton iterations represent the further sequence of operations from t_n to t_{n+1}, where the system of linearised equations is solved and the solution is updated. "p" represents a cell in the domain g_{n+1} at t^n with control volume Ω_p. Its corresponding cells in g^a_{n-1} are indexed as "l" with control volume Ω_l. If the cell is either coarsened or remains unchanged, then by the definition of conservativity,

$$(Q_p\Omega_p)_{n-1} = \sum_{l=1}^{m} Q_l^{n-1}\Omega_l^{n-1}; m = \begin{cases} 1 & \text{if unmodified;} \\ 4 & \text{if coarsened .} \end{cases} \tag{29}$$

Similarly

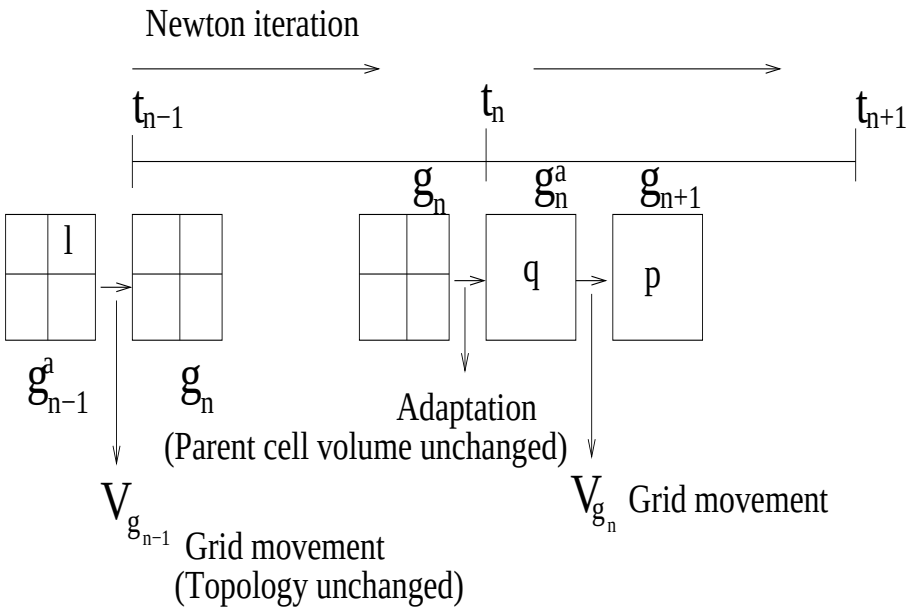

Figure 8: Sequence of operations in a single unsteady ALE simulation timestep during grid coarsening

$$(\oint_{\partial\Omega_{t_n}} Q^{n-\frac{1}{2}} V_{g_{n-1}} \cdot n_n ds)_{n-1} = \sum_{l=1}^{m} Q_l^{n-\frac{1}{2}} (\frac{\Omega_l^n - \Omega_l^{n-1}}{\triangle t}); m = \begin{cases} 1 & \text{if unmodified;} \\ 4 & \text{if coarsened .} \end{cases} \tag{30}$$

Procedure for the refined cells

The cells undergoing refinement during grid adaptation is differently treated. Fig. 9 schematically represents the sequence of operations, the grid goes through during simulation.

The coarse cell in the grid g_{n-1}^a is divided into four cells (referred to as q in g_n) during the process of grid refinement at time t_n. $\Omega_{p'}$ is the control volume to be calculated for the fictitious cells ($p^{'}$) at t_{n-1} in the grid domain g_{n-1}^a, corresponding to the cell (q) in the domain g_n^a with the control volume Ω_q. Those fictitious cells in the domain g_{n-1}^a are represented by dotted lines in Fig. 9.

The difference between $\Omega_{p'}$ and Ω_q is arisen due to the change in control volume because of the deformation at time t_{n-1}. Considering $\triangle\Omega_{p'}$ is the change in control volume during grid deformation,

$$\sum_{p'=1}^{4} \Omega_{p'} + \sum_{p'=1}^{4} \triangle\Omega_{p'} = \sum_{q=1}^{4} \Omega_q. \tag{31}$$

So for each cell $p^{'}$

$$\Omega_{p'} + \triangle\Omega_{p'} = \Omega_q \tag{32}$$

Due to the presence of a single coarse cell at t_{n-1}, the change in control volume can be assumed to be proportional to the original control volume. Hence, $\triangle\Omega_{p'} \propto \Omega_{p'}$

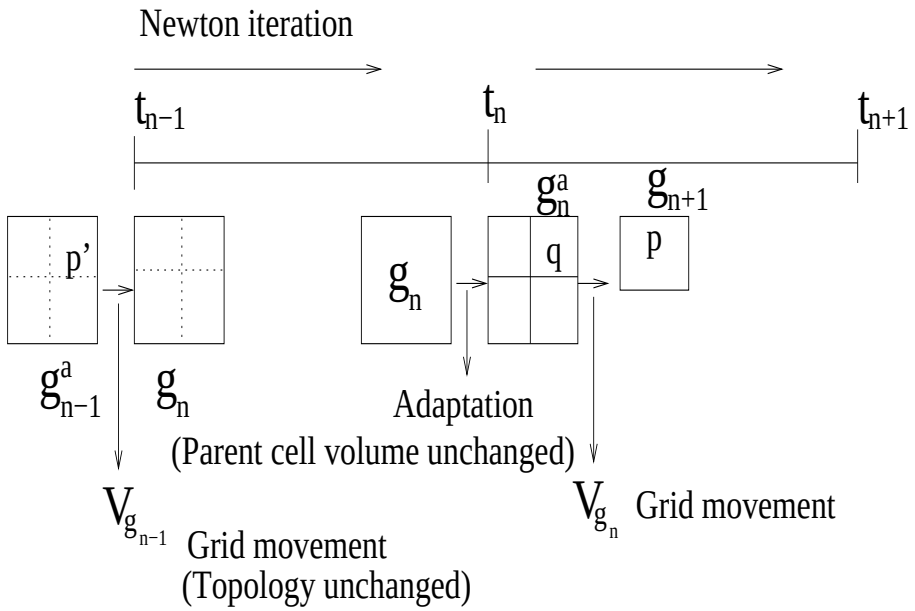

Figure 9: Sequence of operations in a single unsteady ALE simulation timestep during grid refinement

$$\Rightarrow \triangle\Omega_{p'} = K\Omega_{p'}, \tag{33}$$

where K is the proportionality constant.
Substituting Eqn. (33) in Eqn. (31),

$$\sum_{p'=1}^{4} \Omega_{p'} + \sum_{p'=1}^{4} K\Omega_{p'} = \sum_{q=1}^{4} \Omega_q, \tag{34}$$

$$\Rightarrow (1+K) = \frac{\sum_{q=1}^{4} \Omega_q}{\sum_{p'=1}^{4} \Omega_{p'}} = \frac{\sum_{q=1}^{4} \Omega_q}{\Omega_l}. \tag{35}$$

Substituting Eqn. (33) in Eqn. (32),

$$\Omega_{p'} = \frac{\Omega_q}{1+K} = \frac{\Omega_q}{\sum_{q=1}^{4} \Omega_q}\Omega_l,$$

$$(Q_p\Omega_p)_{n-1} = Q_l^{n-1}\Omega_{p'}. \tag{36}$$

Similarly,

$$(\oint_{\partial\Omega_{t_n}} Q^{n-\frac{1}{2}} V_{g_{n-1}} \cdot n_n ds)_{n-1} = Q_l^{n-\frac{1}{2}} \frac{\triangle\Omega_{p'}}{\triangle t} = (Q_l^{n-\frac{1}{2}} \frac{\triangle\Omega_l}{\triangle t})(\frac{\Omega_q}{\sum_{q=1}^{4} \Omega_q}). \tag{37}$$

2.4.4 Explicit time integration scheme

A fully explicit, three stage, Runge-Kutta time stepping scheme is implemented in Quadflow, which forms the smoother to the Multigrid algorithm (section 2.10). The explicit scheme is

comparatively slower than the implicit time integration scheme, as a result of the enforcement of the CFL condition, which limits the allowable local timestep. Nevertheless, the characteristic of the scheme in utilising very low Random Memory during the computations (helpful in three-dimensional simulations) has motivated us in improving its convergence behaviour through Multigrid method.

The Explicit time integration scheme for the Navier-Stokes equations can be represented as

$$\frac{\partial}{\partial t}\int_{\Omega(t)} Q d\Omega + Res(Q^n) = 0 \tag{38}$$

Using three stage Runge-Kutta discretisation,

$$Q^1 = Q^n - \alpha_1 \Delta t Res(Q^n),$$
$$Q^2 = Q^n - \alpha_2 \Delta t Res(Q^1),$$
$$Q^3 = Q^n - \alpha_3 \Delta t Res(Q^2),$$
$$Q^{n+1} = Q^3$$

Q^1, Q^2, Q^3 are the intermediate conservative vectors during the Runge-Kutta multistage process. $\alpha_1, \alpha_2, \alpha_3$ are the stage coefficients with values set to 0.1918, 0.4929, 1.0, respectively.

2.4.5 Timestep computation

The timestep for every cell in the computational domain in simulating the steady flow field is estimated from a prescribed value of the CFL number. Most of the simulations conducted in the course of this work utilise implicit time integration schemes. The implicit schemes are theoretically unconditionally stable; albeit their numerical formulations and the components such as, the method of Jacobian computation, linear equation solver and the type of preconditioner used in the scheme determine the actual numerical stability. Hence, a CFL number much larger than the unit is used during the temporal evolution of the solution. Local time-stepping is used to accelerate the convergence of the steady flow computations. The Eqn. (39) explains the estimation of the timestep from an imposed CFL number, which is the minimum between the estimated convective timestep and viscous timestep.

$$\Delta t = min(\Delta t_c, \Delta t_v) \tag{39}$$

The convective timestep is calculated using,

$$\Delta t_c = CFL \frac{\Omega}{\sum_{i=1}^{n} \lambda_i^{max} \Delta \Omega_i},$$

where "i" is the index, representing the surrounding faces with surface area ($\Delta\Omega_i$) of the control volume (Ω). λ_i^{max} is the maximum eigenvalue of the characteristics corresponding to the flow

field at the control face. In case of preconditioned computations, modified eigenvalues are used. The viscous timestep is given by,

$$\Delta t_v = 0.25 \times CFL \frac{\Omega^2}{\sum_{i=1}^{n} (\frac{\mu_l}{Pr_l} + \frac{\mu_t}{Pr_t})_i \Delta\Omega_i}.$$

The CFL number is set to a small value at the beginning of the computation; the usual value being set 1.0. This small value aids in attaining numerical stability during the development of the flow solution at the initial phase of the computation. The value of CFL number is gradually increased in a geometric progression to reach the maximum prescribed value. The maximum CFL number depends on the physical nature of the flow and the quality of grids used in the simulation, e.g. the maximum CFL number for simulating inviscid flow is set approximately to 10^5 where as for the turbulent flow simulation the value is fixed at 50.

Unsteady flow simulation requires a single global timestep to be prescribed for all the cells in the domain during which the solution is evolved simultaneously, exhibiting a variation of the CFL number in the domain. Maximum CFL number achieved during the computation is estimated and is used to compare the numerical stability of different time integration schemes.

2.4.6 Dual time-stepping

The concept of dual time-stepping is used for unsteady flow simulation at low Mach number in the presence of grid movement. The governing equation is modified to include the preconditioned term.

$$\frac{\partial}{\partial t}\int_{\Omega(t)} Q d\Omega + \Gamma_p \int_{\Omega(t)} \frac{\partial}{\partial \tau} Q d\Omega + Res(Q^{k+1}) = 0. \tag{40}$$

The outer time-loop (Δt) is solved in a time accurate manner with a specified global timestep using Backward difference scheme. The inner time-loop ($\Delta\tau$) is solved using the steady Implicit backward Euler scheme with local time-stepping.

Expanding the middle term in Eqn. (40) by using the chain rule,

$$\Gamma_p \frac{\partial}{\partial \tau}\int_{\Omega(t)} Q d\Omega = \Gamma_p \int_{\Omega(t)} \frac{\partial Q}{\partial \tau} d\Omega + \Gamma_p \int_{\Omega(t)} Q \frac{\partial}{\partial \tau}(d\Omega).$$

As the steady flow solution is required at the inner time-loop, the term $\Gamma_p \int_{\Omega(t)} Q \frac{\partial}{\partial \tau}(d\Omega)$ can be neglected. Thus,

$$\begin{aligned}
\Gamma_p \int_{\Omega(t)} \frac{\partial Q}{\partial \tau} d\Omega &= \frac{\Gamma_p}{\Delta\tau}\Omega(Q_i^{k+1} - Q_i^n) \\
&= \frac{\Gamma_p}{\Delta\tau}\Omega(Q_i^{k+1} - Q_i^n) \\
&= \frac{\Gamma_p}{\Delta\tau}\Omega(Q_i^{k+1} - Q_i^k) + \frac{\Gamma_p}{\Delta\tau}\Omega(Q_i^k - Q_i^n) \\
&= \frac{\Gamma_p}{\Delta\tau}\Omega\Delta Q_i^k + \frac{\Gamma_p}{\Delta\tau}\Omega(Q_i^k - Q_i^n).
\end{aligned}$$

Substituting the expanded term in the Backward difference scheme,

$$
\begin{aligned}
&[\mathbf{I}(\frac{3\Omega^{n+1}}{2\triangle t}+\Gamma_p\frac{\Omega^k}{\Delta\tau})+\frac{\partial}{\partial Q}(Res^k)]\triangle Q^k \\
&\quad=-\oint_{\partial\Omega_{t_{n+1}}}(F(Q^k)-Q^kV^m_{g_n})\cdot n_{n+1}ds-\frac{1}{2}\oint_{\partial\Omega_{t_n}}Q^{n-\frac{1}{2}}V_{g_{n-1}}\cdot n_n ds \\
&\quad+(\frac{\Gamma_p}{\Delta\tau}(\Omega^nQ^k-\Omega^nQ^n))-(\frac{3}{2\triangle t}Q^k\Omega^k-\frac{4}{2\triangle t}Q^n\Omega^n+\frac{1}{2\triangle t}Q^{n-1}\Omega^{n-1}).
\end{aligned}
\tag{41}
$$

The linearised system of equations inside the inner time loop is solved by a Krylov subspace method. ILU(2) Preconditioned Generalised Minimal Residual (GMRES) method is used for the purpose.

2.5 Low Mach number preconditioning

Mathematically, Navier-Stokes equations solved with the time marching iterative method are hyperbolic in nature with a distinct set of characteristic variables. These characteristic variables are the eigenvectors of the Jacobian matrix, moving at certain characteristic speeds. The disparity in the speeds of propagation, detected by the difference in the eigenvalues is the cause of the stiffness in the numerical scheme.

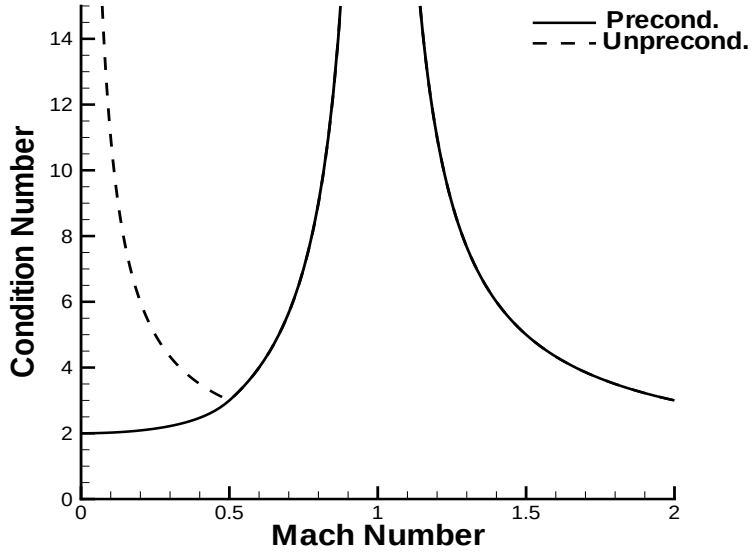

Figure 10: Variation of condition number with Mach number

Condition number defined as the ratio between the largest and smallest eigenvalues, quantitatively represents the numerical stiffness of the system. Dependency of condition number on Mach number is shown in the Fig. 10. Larger magnitude of the condition number signifies

the inhibition of convergence and deterioration of the solution accuracy observed during flow computations in the low Mach number region.

Traditionally, pressure based methods are used to simulate the flow field at lower Mach numbers. Many variants of these pressure based methods (SIMPLE, SIMPLEC, PISO) [57] on collocated grid structure are used to establish pressure-velocity coupling in order to achieve a divergence free velocity distribution in the computational domain. Conversely, density based methods are used to solve the flow field in the compressible flow regime. Numerical schemes based on the density based formulation suffer from the drawback to deal with the numerical stiffness in the low Mach number regime because of the disparity in the characteristic speeds. Initial work was carried out by Chorin [58] in the form of addition of an artificial compressibility term to the pressure equation for effective Mach number dependent scaling to extend the validity of the formulation to the incompressible flow domain. The foundation established by Chorin and its subsequent extension by Turkel, Weiss and Smith [59–61] led to the development and maturity of the *preconditioning approach* in the framework of the density based method for flow simulation in relatively lower Mach number.

A preconditioning matrix is multiplied with the temporal part of the Jacobian Matrix which modifies the eigenvalues to decrease the condition number favourably, resulting in the faster convergence and improved solution accuracy. Multiplication of the preconditioner to the Jacobian matrix modifies the formulation at the governing equation level. As the temporal part of the equation is modified, the accuracy of the steady state flow field is not affected when the iterative process achieves adequate convergence level through local time-stepping. The process of flux evaluation and timestep computation need to be modified consistently to take into account the effect of the change in the eigenvalue structure of the system. Modified eigenvalues are used to determine the left and right propagating waves in the HLLC scheme [62] as explained in the evaluation of inviscid flux formulation in section 2.6.1.

Γ_P is the preconditioning matrix defined for the set of primitive variables, W [61]

$$\Gamma_p = \begin{bmatrix} \{\Theta+(1/RT)\} & 0 & 0 & 0 & -\rho/T & 0 \\ \{\Theta+(1/RT)\}u & \rho & 0 & 0 & -\rho u/T & 0 \\ \{\Theta+(1/RT)\}v & 0 & \rho & 0 & -\rho v/T & 0 \\ \{\Theta+(1/RT)\}w & 0 & 0 & \rho & -\rho w/T & 0 \\ \{\Theta+(1/RT)\}H-1 & \rho u & \rho v & \rho w & \rho(c_p-H/T) & 0 \\ \{\Theta+(1/RT)\}\bar{\nu} & 0 & 0 & 0 & -\rho\bar{\nu}/T & \rho \end{bmatrix}$$

Multiplication of the transformation matrix transfers the preconditioning matrix to be applied to a set of conservative variables, which is denoted as Γ_c.

$\Gamma_c = \Gamma_p \dfrac{\partial W}{\partial Q}$.

Θ is the preconditioning parameter, which depends on the reference speed and local sonic

speed [61],
$\Theta = \frac{1}{U_r^2} - \frac{1}{a^2}, U_r = M_r * a$.

Preconditioning modifies the eigen system of the numerical equation. Modified eigenvalues are

$$\lambda(\Gamma_c^{-1}\frac{\partial F_c}{\partial Q}) = \frac{1}{2}(1+M_r^2)v_n \pm \frac{a}{2}\sqrt{(1-M_r^2)^2M_n^2+4M_r^2}, v_n \tag{42}$$

The value of the reference Mach number (M_r) controls the effectiveness of the preconditioning matrix. The regional variation of M_r in the computational domain provides a local nature to the preconditioning. In order to avoid the reference Mach number being very small near the stagnation regions, a cutoff value for M_r is specified, depending on the free stream Mach number M_∞ and local cell Reynolds number. The preconditioning is switched off in order to retrieve the original formulation by setting the reference Mach number to unit, when the local normal Mach number (M_n) reaches above 0.5.

Combining the ideas of Darmofal [63] and Weiss [60], M_r can be defined as

$$M_r = \begin{cases} \varepsilon & \text{if } M_n \leq \varepsilon; \\ \sqrt{(\frac{2.0M_n^2}{1-2.0M_n^2})} & \text{if } M_n \in (\varepsilon, 0.5); \\ 1 & \text{if } M_n \geq 0.5 \text{ .} \end{cases}$$

There, $\varepsilon = max(\varepsilon_{inviscid}, \varepsilon_{viscous})$,

$\varepsilon_{inviscid} = KM_\infty$, $\varepsilon_{viscous} = \frac{Ur}{\nu}$, U =local fluid speed.

In our work, $K \in [0.5, 0.85]$. Usually a higher value of K adds robustness to the scheme and is preferred for the turbulent flow simulation.

$\varepsilon_{viscous}$ is the local cell Reynolds number, depending upon the characteristic length of the cells and has to be taken into account during laminar as well as turbulent flow simulation. The characteristic length is defined by

$$r = \frac{\Delta x \Delta y}{\sqrt{(\Delta x)^2 + (\Delta y)^2}},$$

where Δx and Δy are the maximum and minimum dimensions of the cell.

2.6 Flux discretisation

2.6.1 Evaluation of inviscid fluxes

In the literature, there are two distinct approaches used to compute the cell interface flux in the Finite Volume Discretisation method. One of the earlier methods pioneered by Jameson [64], uses the artificial viscosity as a stabiliser to the second order central differencing scheme. The fourth order dissipation term preventing the odd-even decoupling in the numerical scheme is not sufficient enough to inhibit the oscillation in solution in the vicinity of the shock. Hence, an additional second order artificial viscosity term controlled by a numerical switch depending upon the local pressure variation in the computational domain is used.

The second approach is to use the upwind method by taking into account the propagation of the waves in the computational domain. This approach is again subdivided into two groups. Flux difference splitting schemes, initially formulated by Godunov to solve the Riemann problem, computes the flux explicitly through the use of wave speeds obtained by solving an eigenvalue problem. Flux-vector splitting methods, numerically splits the interface flux on the basis of the flow speed or Mach number. A Flux-vector splitting technique proposed by Van Leer [65] is used, which numerically splits the interface flux on the basis of the interface Mach number.

In the current work, the upwind method designed by Harten, Lax, Van-Leer and later extended to capture the contact discontinuities (HLLC) is chosen for numerical discretisation of the convective flux to achieve improved accuracy in the spatial resolution as a result of low numerical viscosity. Achieving a smaller numerical viscosity, which brings stability of the scheme is crucial in accurate resolution of the features present in the viscous flow field. The Riemann problem based on the projection of the state vectors on both sides of the face from the corresponding cell centered data is solved at the interface for computing the numerical flux. Data projected on the face is rotated in the normal direction using the unit surface normals for solving the one-dimensional Riemann problem.

Intercell flux ($F_{l,r}^{hllc}$) at the face shared between two control volumes is computed using the expression,

$$F_{l,r}^{hllc} = \begin{cases} F_l & , \text{ if } s_l > 0; \\ F_{*l} = F_l + s_l(Q_l^* - Q_l), & \text{if } s_l \leq 0 \leq s_*; \\ F_{*r} = F_r + s_r(Q_r^* - Q_r), & \text{if } s_* \leq 0 \leq s_r; \\ F_r & , \text{ if } s_r < 0; \end{cases} \tag{43}$$

where, F_l and F_r are the flux vectors, depending upon the left and right state vectors respectively. The blending of these two flux vectors is controlled by the wave speeds (s_l, s_r,s^*), which depend on the state variables. The wave speeds are determined by the Roe averaged value of the left and right state vectors as expressed below,

$$s_l = min[(\hat{u} - \hat{a} - V_{g_n}^m), (u_l - a_l)]$$

$$S_r = min[(\hat{u} + \hat{a} - V_{g_n}^m), (u_r + a_r)]$$

$$s^* = \frac{p_r - p_l + \rho_l u_l(s_l - u_l) - \rho_r u_r(s_r - u_r)}{\rho_l(s_l - u_l) - \rho_r(s_r - u_r)}$$

where Roe averaged velocity, total enthalpy and sonic speed are defined as

$\hat{u} = \frac{\sqrt{\rho}_l u_l + \sqrt{\rho}_r u_r}{\sqrt{\rho}_l + \sqrt{\rho}_r}$, $\hat{H} = \frac{\sqrt{\rho}_l H_l + \sqrt{\rho}_r H_r}{\sqrt{\rho}_l + \sqrt{\rho}_r}$, $\hat{a} = [(\gamma - 1)[\hat{H} - \frac{1}{2}\hat{u}^2]^{\frac{1}{2}}$.

The intermediate state vector due to the jump over the contact discontinuity is

$$Q_k^* = (\rho_k)(\frac{s_k - u_k}{s_k - s^*}) \begin{pmatrix} 1 \\ s^* \\ v_k \\ w_k \\ \frac{E_k}{\rho_k} + (s^* - u_k)[s^* + \frac{p_k}{\rho_k(s_k - u_k)}] \end{pmatrix},$$

where k is the index used to represent either left or right state vectors.

For low Mach number preconditioning, the wave speeds are modified in order to take into account the modification of the eigenvalues due to the preconditioning.

Flux is evaluated at the interface using Flux Vector Splitting, originally suggested by Van Leer and later modified by Anderson [66] for simulating inviscid ALE problems. The formulation used is described below.

$$F_c^{'} \cdot n = \begin{pmatrix} f_{mass}^{\pm} \\ f_{mass}^{\pm} \left[n_x \frac{(-V_n \pm 2a)}{\gamma} \right] + u \\ f_{mass}^{\pm} \left[n_y \frac{(-V_n \pm 2a)}{\gamma} \right] + v \\ f_{energy} \end{pmatrix}. \tag{44}$$

$F_c^{'}$ is the flux vector with the modification for the grid velocity, and

$f_{mass}^{\pm} = \pm \frac{\rho a}{4}(M_n \pm 1)^2$,

$f_{energy}^{\pm} = f_{mass} \left(\left[\frac{-(\gamma-1)V_n^2 \pm 2(\gamma-1)V_n a + 2a^2}{\gamma^2 - 1} \right] + \frac{u^2 + v^2}{2} + \frac{V_{g_n}(-V_n \pm 2a)}{\gamma} \right)$.

The interface velocity normal to the face is given by

$V_n = V \cdot n - V_{g_n}^m$,

$M_n = V_n / a$.

u and v are components of the velocity along the Cartesian coordinate directions, a is the sonic speed. $V_{g_n}^m$ is the modified normal component of the grid velocity, explained in the derivation of the BDF scheme in the section 2.4.2.

2.6.1.1 Reconstruction Improvement in the spatial resolution of the solution through the process of *reconstruction* is initially proposed by Van Leer in his seminal paper on Monotonic Upstream-centered Scheme for Conservation Laws (MUSCL). The state variables at both sides of the face, used for solving the approximate Riemann problem are reconstructed from the cell centered state vectors utilising the available gradient information at the cell center. Gradient is calculated by creating an approximate linear surface by using the data at the cell center along with the information from the neighbouring cells present in the stencil. Direct neighbours sharing the faces and cross neighbours at the corner of the cells are used to construct the stencil.

A multi-dimensional first order accurate Taylor series expansion is considered to project the primitive variables from the cell center to all the neighbouring cells in the stencil.

$$Q(r) = Q(r_i) + \phi_i \nabla Q_i \cdot (r - r_i) \tag{45}$$

The number of equations is determined by the number of neighbouring cells and the number of unknowns in the equation depends on the dimensionality of the problem. Hence, the method results in an over-determined system, which is solved by the least-squares method [72].
The process of linear reconstruction aids in achieving second order spatial discretisation and automatically satisfies the conservation of the solution variables in the control volume due to the linearity. The extension of the process of reconstruction to three-dimensional flow simulation is straight forward.

The accuracy of the gradients, calculated with the above reconstruction procedure is deteriorated in the presence of highly stretched grid used for the turbulent flow simulation. Several alternatives have been developed, such as Weighted Least Square [67], to address the problem. For computations involving viscous fluid flow, the Green-Gauss method [72] is employed to evaluate the gradients. It relies on creating a closed volume surrounding the cell under consideration to include the surrounding cells during the process of creating the stencil.

2.6.1.2 Limiter In certain circumstances, the reconstruction process may cause the numerical scheme to violate the non-linear stability condition by generating local extremas beyond the solution data in the neighbourhood cells. The phenomenon creates overshoots and undershoots of the solution, specifically in the high gradient regions, e.g. in the localities around the shock. In order to avoid the generation of unphysical extrema during the reconstruction process, monotonicity is enforced by the application of a limiter to satisfy Total Variation Diminishing (TVD) condition [74]. A limiter designed by Venkatakrishnan [75], which avoids self-flipping in the smooth flow region, but prevents numerical oscillation in the high gradient region to achieve a better convergence behaviour, is employed, as described below.

ϕ_i is the limiter in Eqn. (45).

For every cell i,

$\phi_i = min(\phi_{i,g}), g = 1, 2 \ldots N$. N is the number of neighbour cells sharing faces with cell i.

$$\phi_{i,g} = \begin{cases} \dfrac{Q_{i,g}^{+^2} + 2Q_{i,g}^{+}Q_{i,g}^{-} + \varepsilon_l}{Q_{i,g}^{+^2} + Q_{i,g}^{+}Q_{i,g}^{-} + 2Q_{i,g}^{-^2} + \varepsilon_l}, & \text{if } Q_{i,g}^{-} \neq 0; \\ 1 \qquad\qquad\qquad , & \text{if } Q_{i,g}^{-} = 0; \end{cases} \tag{46}$$

with

$$
\begin{aligned}
Q^{-}_{i,g} &= Q_g - Q_i, \\
Q^{+}_{i,g} &= \begin{cases} Q^{max}_i - Q_i, & \text{if} \quad Q^{-}_{i,g} > 0 \\ Q^{min}_i - Q_i, & \text{if} \quad Q^{-}_{i,g} < 0 \end{cases}
\end{aligned}
$$

Q^{max}_i and Q^{min}_i are the maximum and minimum values of the conservative variable among the cells in the stencil.

$$
\begin{aligned}
Q^{max}_i &= max_{j=1,\ldots,N} \left\{ Q_i, Q_j \right\}, \\
Q^{min}_i &= min_{j=1,\ldots,N} \left\{ Q_i, Q_j \right\}.
\end{aligned}
$$

Q_g denote the unlimited reconstructed cell centered values of Q_i at the face centers. The parameter ε_l is typically set to 10^{-4}.

2.6.2 Computation of the viscous fluxes

Viscous flux at the faces surrounding the control volume is obtained using the gradient correction method suggested by Weiss *et al.* [73], which uses compact stencil involving all neighbouring cells. The averaged gradient at the face between the cell centers for a variable "w" can be corrected as:

$$\nabla w^{'}_{lr} = \nabla w_{lr} + \frac{1}{|r_r - r_l|^2}(\delta w_{lr} - (\nabla w_{lr}.(r_r - r_l))(r_r - r_l)), \tag{47}$$

where, r_r, r_l are the position vectors of the left and right cells, respectively. δw_{lr} is the difference in the magnitude of the primitive variables between the left and right cells sharing the face, and ∇w_{lr} represents the uncorrected averaged gradient between the left and right cells.

$$\nabla w_{lr} = \frac{\nabla w_l + \nabla w_r}{2}$$

In order to obtain the gradients at the cell center, a system of two equations which are formed from the data available at the cell centers and nodes are solved. Data at the nodes are obtained by the inverse distance averaging of the cell-centered data surrounding the corresponding node as elucidated in the Fig. 11.

$$w_{n_1} = d_{n_1} \sum_{i=1}^{n^1} \frac{w_i}{d_i}$$

$$w_{n_2} = d_{n_2} \sum_{i=1}^{n^2} \frac{w_i}{d_i}$$

w_{n_1} and w_{n_2} are the interpolated primitive variables at nodes $n1$ and $n2$, respectively using the available neighbourhood cell center solution variables. n^1 and n^2 are the number of neighbours

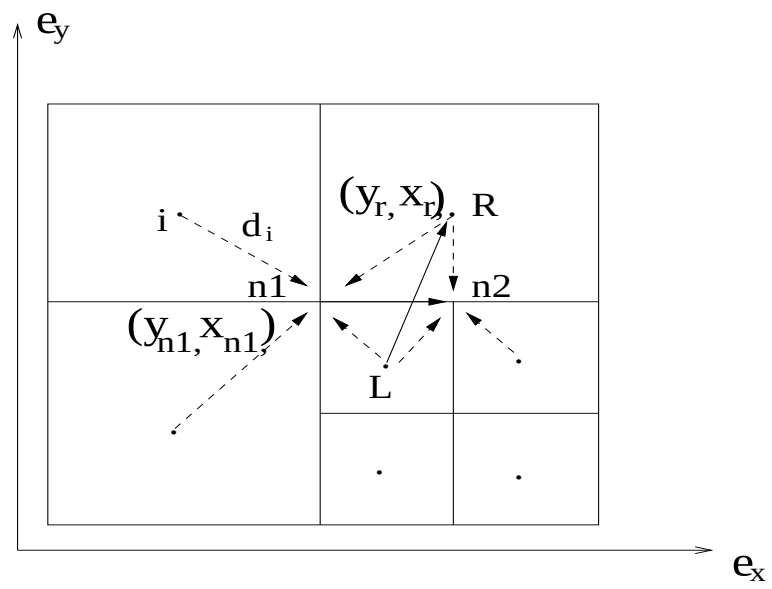

Figure 11: Cell to node interpolation and formulation of a two-equation system for gradient computation

surrounding the nodes $n1$ and $n2$, respectively. d_i, is the distance of the node from the i_{th} neighbouring cell. Applying the formula, $\frac{\partial w}{\partial x}\Delta x + \frac{\partial w}{\partial y}\Delta y = \Delta w$, in two available directions and solving the generated two system of equations,

$$\frac{\partial w}{\partial x} = \frac{(w_{rl}y_{n_{21}} - w_{n_{21}}y_{rl})}{D}, \tag{48}$$

$$\frac{\partial w}{\partial y} = \frac{(w_{n_{21}}x_{rl} - w_{rl}y_{n_{21}})}{D}, \tag{49}$$

where $D = x_{rl}y_{n_{21}} - y_{rl}x_{n_{21}}$,

$w_{rl} = w_r - w_l$,

$x_{n_{21}} = x_{n2} - x_{n1}, y_{n_{21}} = y_{n2} - y_{n1}$ and,

$x_{rl} = x_r - x_l, y_{rl} = y_r - y_l$.

(x_{n1}, y_{n1}) and (x_{n2}, y_{n2}) are the coordinates of the two nodes under consideration. (x_l, y_l), (x_r, y_r) are the coordinate pairs of the left and right cells, respectively.

2.7 Imposition of the boundary condition

For wellposedness of the problem, governing equations are associated with the initial condition of the flow variables in the computational domain as well as the boundary conditions specified on the boundaries of the domain. The computational domain can't extend infinitely and needs the flow variables to be specified on the boundaries for the closure. Effective boundary condition can be helpful in reducing the size of the computational domain and helps in accurate transmission of the waves associated with the flow without undergoing any artificial reflection.

2.7.1 Conditions for the inlet and exit boundaries

2.7.1.1 Boundary condition for the supersonic flow In case of supersonic flow governed by the Euler equations, all the characteristic have positive components in flow direction which is assumed to be from the left to the right direction of the computational domain. So, if the flow is entering into the domain then all the variables are obtained from the free stream condition. If the outflow boundary is turned out to be supersonic, then all the variables are obtained from the interior of the computational domain.

2.7.1.2 Characteristic method for subsonic condition When the flow field is governed by the Euler equations, not all the characteristic direction vectors have positive components in the flow direction. The solution variables are determined by the Riemann invariants propagating along characteristics moving at the characteristic speeds. Away from the highly active regions, near the boundary, these characteristic lines intersect each other to uniquely determine the flow variables. In the absence of any strong shock, under the isentropic flow condition, the method of characteristics can be used to specify the boundary conditions as described below.
At the inflow boundary face, the right running characteristic variable coming from the free stream condition intersect with the left running characteristic variable coming from the interior of the domain to detect the left side state variables of the boundary face as denoted as (L) in the Fig. 12.

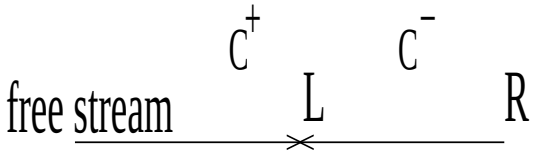

Figure 12: Spatial component of the characteristics at the inflow boundary

C^+ characteristic coming from the free stream and responsible for propagating the positive Riemann invariant,

$$u_\infty + \frac{2a_\infty}{\gamma-1} = u_L + \frac{2a_L}{\gamma-1}$$

C^- characteristic coming from the computational domain and responsible for propagating the negative Riemann invariant

$$u_R - \frac{2a_R}{\gamma-1} = u_L - \frac{2a_L}{\gamma-1}$$

Using the above two equations, the unknown left side state variables of the boundary face is calculated.

$$u_L = \frac{u_R + u_\infty}{2} + \frac{2}{\gamma-1}(a_\infty - a_R)$$

$$a_L = (\gamma-1)\frac{u_\infty - u_R}{2} + (a_R + a_\infty)$$

The other components of the velocities,

$v_L = v_\infty, \quad w_L = w_\infty$

The treatment of the outflow boundary is similar except that the directions of the characteristics have changed their role with respect to interior and far stream.

On the C^+ characteristic, $u_R + \dfrac{2a_R}{\gamma-1} = u_L + \dfrac{2a_L}{\gamma-1}$

On the C^- characteristic, $u_\infty - \dfrac{2a_\infty}{\gamma-1} = u_L - \dfrac{2a_L}{\gamma-1}$

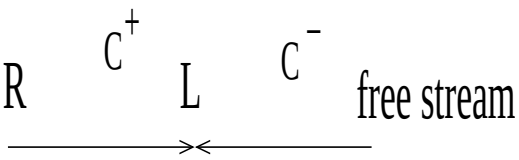

Figure 13: Spatial components of the characteristics at the outflow boundary

From these two equations we have,

$$u_L = \frac{u_R + u_\infty}{2} + \frac{2}{\gamma-1}(a_R - a_\infty)$$

$$a_L = (\gamma-1)\frac{u_R - u_\infty}{2} + (a_R + a_\infty)$$

The other components of the velocities, $\quad v_L = v_R,\ w_L = w_R$

Temperature at the boundary is obtained using the above obtained sonic speed.

$T_L = \frac{1}{\gamma R} a_L^2$

C^o characteristic represent the material wave moving with the fluid. Assuming isentropic condition on the characteristic, we have

$$\rho_L = (\frac{T_L}{T_R})^{\frac{1}{\gamma-1}} \rho_R$$

Pressure is computed using the ideal gas equation, $P_L = \rho_L R T_L$.

2.7.1.3 Extrapolation method for subsonic boundary condition Viscous flow is associated with long free shear layers, specifically in the presence of large scale flow separation, which may extend to the boundary of the computational domain. The flow in the shear layer is dominated by viscosity and assumption of isentropic flow condition becomes invalid in that region. Hence, an extrapolation type boundary condition is used in dealing with the viscous flow simulation.

Free stream Mach number, temperature and the angle of attack are specified from the external condition and the pressure is interpolated from the interior of the computational domain, at the inlet boundary. At the outflow boundaries, density and velocity are interpolated from the interior domain and the free stream static pressure is prescribed.

2.7.1.4 Flow angle specification in 3D Two angles are specified to uniquely define the free stream velocity field at the inlet boundary for three-dimensional flow simulation. The angle specified with Z-axis (θ) is used to project the flow velocity on X-Y plane, which is further divided into sub-components along X and Y axis by specifying the angle with X-axis(α).

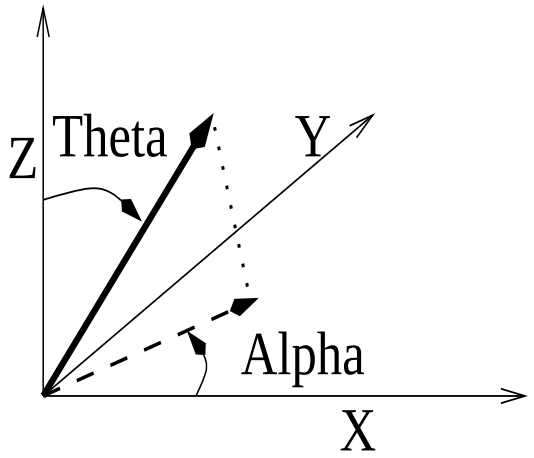

Figure 14: Specification of inlet flow angles for three-dimensional flow simulation

2.7.2 Vortex correction for the lifting bodies

Vortex correction [85] is used at the far–field boundaries in order to improve the imposition of the boundary condition for the flow field generated due to the lifting bodies. The flow variables at the far–field boundary are specified by a solution according to the full potential flow theory. The corrected velocity components are prescribed by

$$\begin{aligned} u &= |V_\infty| cos\alpha + V_\Gamma sin\theta\,, \\ v &= |V_\infty| sin\alpha - V_\Gamma cos\theta\,. \end{aligned}$$

The vortex induced velocity magnitude V_Γ is given by,

$$V_\Gamma = \frac{\Gamma}{2\pi r} \frac{\sqrt{1-M_\infty^2}}{(1-M_\infty^2 sin^2(\theta-\alpha))} \tag{50}$$

where the circulation Γ of the vortex is determined by, $\Gamma = 0.5 c_{ref} |V_\infty| C_L$.
c_{ref} denotes the chord length and C_L is the lift coefficient. r, θ are the radius and the polar angle measured from the quarter–chord location to the individual boundary face at the far–field boundary, respectively. α is the angle of attack.

2.7.3 Boundary condition on the viscous wall

Normal component of the velocity is set to zero for the inviscid flow computation, but the tangential velocity components are non-zero. No-slip wall boundary condition is imposed on

the solid wall for viscous flow simulation. Heat flux term in the energy equation is set to zero under the assumption of adiabatic boundary condition on the solid wall. Total internal energy is set according to the specified wall temperature for the isothermal wall boundary condition. Eddy viscosity is set to zero on the solid wall, when solving the turbulent flow equation.

2.8 Evaluation of Jacobian

The linearisation process of the residual in the implicit formulation of the Navier-Stokes equations results in the creation of the Jacobian matrix, which along with the residual forms the system of linear equations. The section explains the formulation of the Jacobian matrix, which is comprised of inviscid and viscous fluxes contributing to the residual.

2.8.1 Inviscid Jacobian

Inviscid Jacobian is computed analytically from the approximate Riemann solver using Automatic Differentiation tool, ADIFOR [78]. The subroutine for the approximate Riemann solver to compute the inviscid fluxes is given as the input to the tool, and the chain rule of differential calculus is used to automatically generate the Jacobian matrix as the output routine. The analytical method of computing the Jacobian is more stable and allows high CFL number to be used in the computation compared to the Jacobian calculated numerically. Referring to the Eqn. (11) in section 2.4.1,

$$\Delta Q^n = -J^{-1} Res(Q^n)$$

Where the Jacobian "J" is defined as

$$J = [\Gamma_c \frac{I}{\Delta t}\Omega + \frac{\partial}{\partial Q} Res(Q^n)]$$

The residual is defined as

$$Res(Q^n) = \oint_{\Omega_t} F(Q_l, Q_r).nds = \sum_{r=1}^{N} F_n(Q_l, Q_r)\Delta S_r$$

"r" is the index of N number of neighbouring cells surrounding the cell under consideration (represented as the index "l"). Q_l, Q_r are the conservative variables at the centers of the left and right cells sharing the face, having the surface area represented as ΔS_r. The interface flux is computed using the approximate Riemann solver (HLLC) given by Eqn. (43).
The Jacobian matrix is

$$\frac{\partial}{\partial Q}(Res(Q^n)) = \sum_{r=1}^{N} \frac{\partial}{\partial Q_l}(F_n(Q_l, Q_r)\Delta S_r)I + \sum_{r=1}^{N} \frac{\partial}{\partial Q_r}(F_n(Q_l, Q_r))\Delta S_r \tag{51}$$

The first term in the right hand side of Eqn. (51) represents the self contribution of the inviscid fluxes and is placed as the diagonal terms in the Jacobian matrix. The second term represents

the contribution of the inviscid fluxes from the surrounding neighbour cells and are located as the off-diagonal term in the Jacobian matrix. Addition of the self contributing terms in the diagonal position provides the diagonal dominant nature to the Jacobian matrix.

2.8.2 Viscous Jacobian

The method of computing the Jacobian matrix contributed from the viscous flux is described below. Inclusion of the Jacobian matrix contributed from the viscous flux provides robustness to the numerical scheme in using comparatively larger CFL numbers during the temporal evolution.

Viscous flux at the face center is a function of the primitive variables and their corrected gradients computed using the Eqn. (47). As the Jacobian matrix signifies the dependency of the flux with respect to the cell-centered conservative variables, an analytical method based on the chain rule of differential calculus is employed.

$$J_v = \frac{\partial F_v}{\partial Q} = \frac{\partial F_v}{\partial w_v}\frac{\partial w_v}{\partial w}\frac{\partial w}{\partial Q}. \tag{52}$$

w_v is a function of the gradients of the primitive variables at the face centers. F_v, w, Q represent the diffusive flux, primitive state variables and the conservative state vector, respectively.

$\frac{\partial F_v}{\partial w_v}$ represents the dependency of the viscous flux terms on the gradients of the primitive variables. $\frac{\partial w}{\partial Q}$ is the transformation matrix relating the primitive variables to the conservative variables.

w_v can be expressed,

$$w_v = func(\frac{\partial w}{\partial x}, \frac{\partial w}{\partial y})$$

Using Eqn. (48), for the left state

$$\frac{\partial}{\partial w}(\frac{\partial w}{\partial x}) = \frac{-y_{n_{21}} - y_{rl}(\frac{d_{n2}}{d_2} - \frac{d_{n1}}{d_1})}{D}$$

where,

$$d_{n1} = \frac{1}{\sum_{i=1}^{n^1}\frac{1}{d_i}},$$

$$d_{n2} = \frac{1}{\sum_{i=1}^{n^2}\frac{1}{d_i}}$$

d_i is the distance of the node from the cell center. n^1 and n^2 are the numbers of the neighbour cells surrounding the nodes n1 and n2, as shown in the Fig. 11.

2.9 Linear equation solver and local time-stepping

Implicit approach with inexact Newton iteration method has been employed to solve the non-linear equation. It is given by,

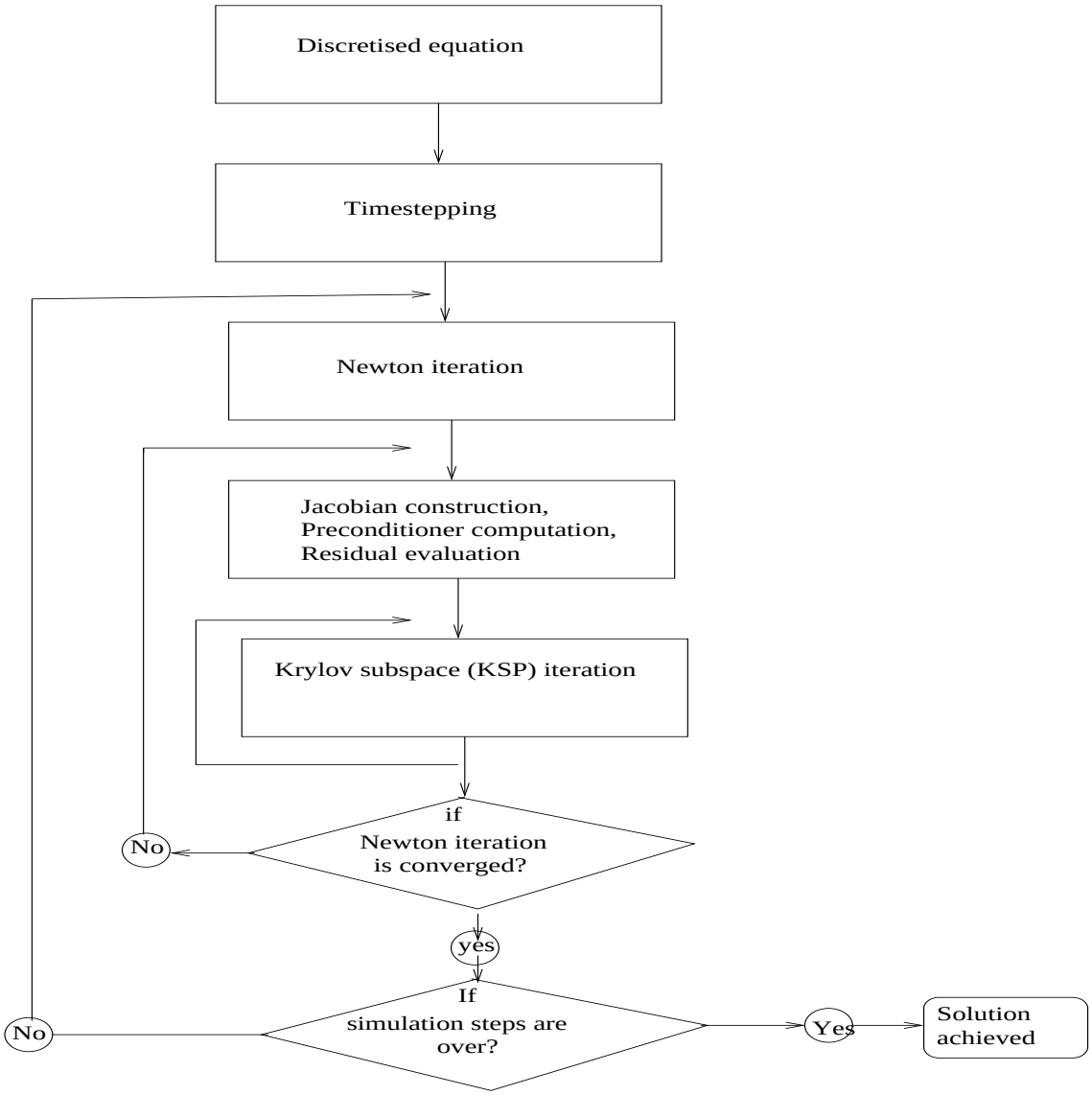

Figure 15: Sequence of iterative loops for unsteady flow simulation

$$\|F(Q_k) + A(Q_k)\triangle Q_k\| \leq \eta_k \|F(Q_k)\|,$$

where η_k is fixed to 10^{-4} .

k is the index of Newton iteration. At the beginning of each Newton iteration the non-linear equation is linearised and solved by a system of linear equations solver. In this work, restarted GMRES with ILU(2) preconditioner [77] has been used.

2.10 Non-linear Full Approximation Storage Multigrid scheme

In order to improve the convergence behaviour of the explicit time integration scheme in Quadflow, a Full Approximation Storage non-linear V-cycle Multigrid method [68, 69] is implemented. Multigrid method is based on the principle of capturing the components of the solution

attributed to a particular spatial frequency with the equivalent grid size. Solution from a well posed initial-boundary value problem results in the superposition of the spectral components with the wavelengths ranging from the size of the computational domain to the lowest being the Kolmogorov scale [29]. Solution components from the larger wavelengths are quickly captured by the comparatively coarser grid, whereas the high frequency components are better captured with the finer grids. So, instead of employing the finest grid to capture all the components of the solution which results in increasing the cost of computation, Multigrid uses smoothing iterations with the exchange of information on a sequence of grid levels. Iterations over the coarser grids with reduced number of cells provides benefit in the form of computational expenses, and faster convergence is achieved due to the improved capturing of the solution. The solution accuracy remains undeteriorated as the level of convergence on the finest grid level is used as the criterion to stop the simulation process.
We have implemented the algorithm to perform the sequential operations over the grid levels obtained through the grid coarsening strategy, described below.

2.10.1 Grid coarsening algorithm

A grid coarsening strategy is developed which functions for both the structured as well as the adapted grids. The concept is particularly advantageous with the grid adaptation, as the level and neighbourhood information of the cells are available through the multilevel indices set up during the grid adaptation. The four neighbouring cells belonging to the same quadrangle at the finest level of the currently available adapted grid are identified and combined together to generate the coarser level grid. No cells belonging to the different levels are grouped together during the process in order to avoid the complexity. This process of coarsening is carried out till the coarsest level (grid level with the level index=0) is achieved. So during any phase of computation, the number of available coarse grid sets is one more than the number of grid adaptation level. To trade-off the cost of computation for coarsening and to achieve the benefit in convergence from the Multigrid algorithm, the number of coarse grid sequences is restricted to four levels.

2.10.2 V-cycle

V-cycle is employed with the computation starting from the finest level gradually moving towards the coarsest grid level. The solution and residual from the finer level are restricted to the next coarser grid level after a pre-determined number of smoothing iterations. The governing equation at the new coarse level is modified to take into account the computed relative truncation error during the smoothing iterations. The process is continued till the coarsest level is achieved. The correction term at the coarser level is computed and prolonged to the next finer level. No smoothing iterations are carried out after the prolongation step. Certain number

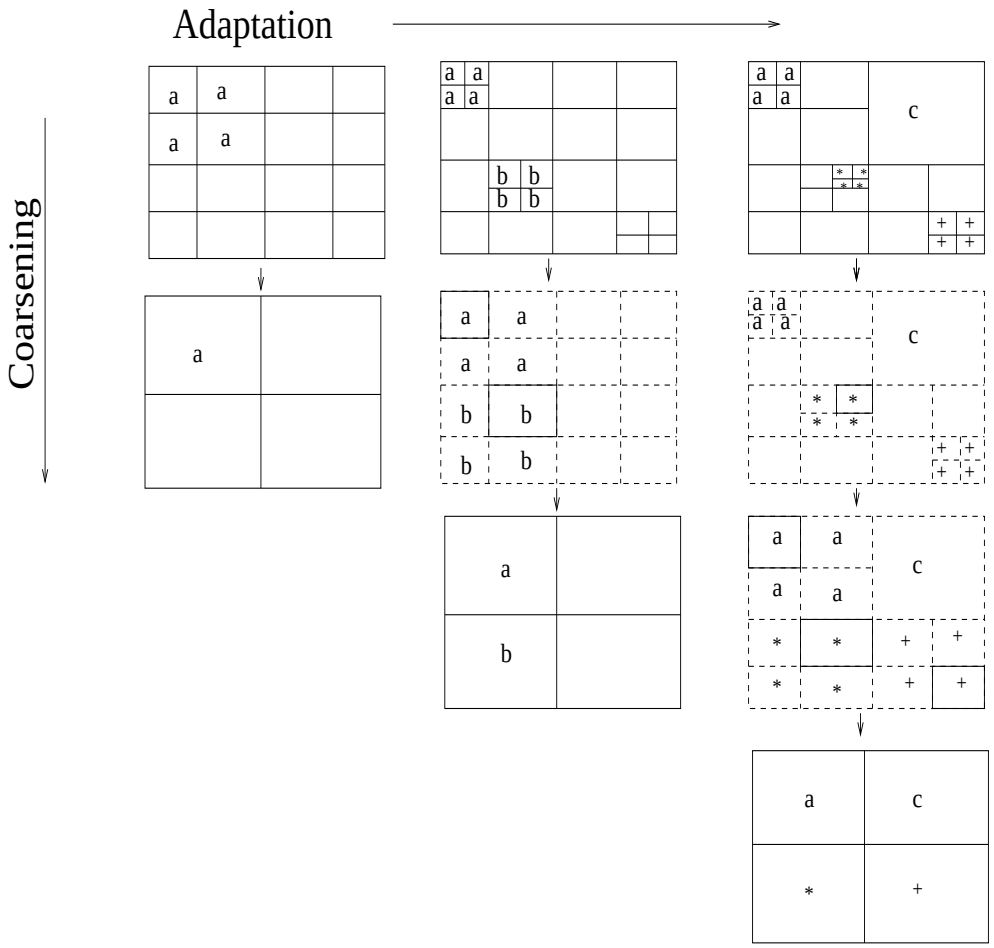

Figure 16: Hierarchy of coarse grids in adaptive Multigrid computation

of Multigrid cycles are conducted till the convergence level at the finest level has achieved a pre-set value.

2.10.3 FAS algorithm

Volume weightage averaging is used during the restriction process to transfer the solution and residual from the finer grid to the next coarser grid level.

$$Q_k^n = I_{k+1}^k(Q_{k+1}^n) = \frac{1}{\Omega_k}\sum_{finecells} Q_{k+1}^n \Omega_{k+1}, \tag{53}$$

$$Res_k^n = I_{k+1}^k(Res_{k+1}^n) = \sum_{finecells} Res_{k+1}^n. \tag{54}$$

The identity information of the finer cells constituting the coarser cells obtained during the grid coarsening process is used during averaging.

The governing equations on the coarser grid levels are modified with the *relative truncation error*

$$\int_{\Omega(t)} \frac{\partial Q_k^n}{\partial t} d\Omega + R(Q_k^n) - \tau_k = 0. \tag{55}$$

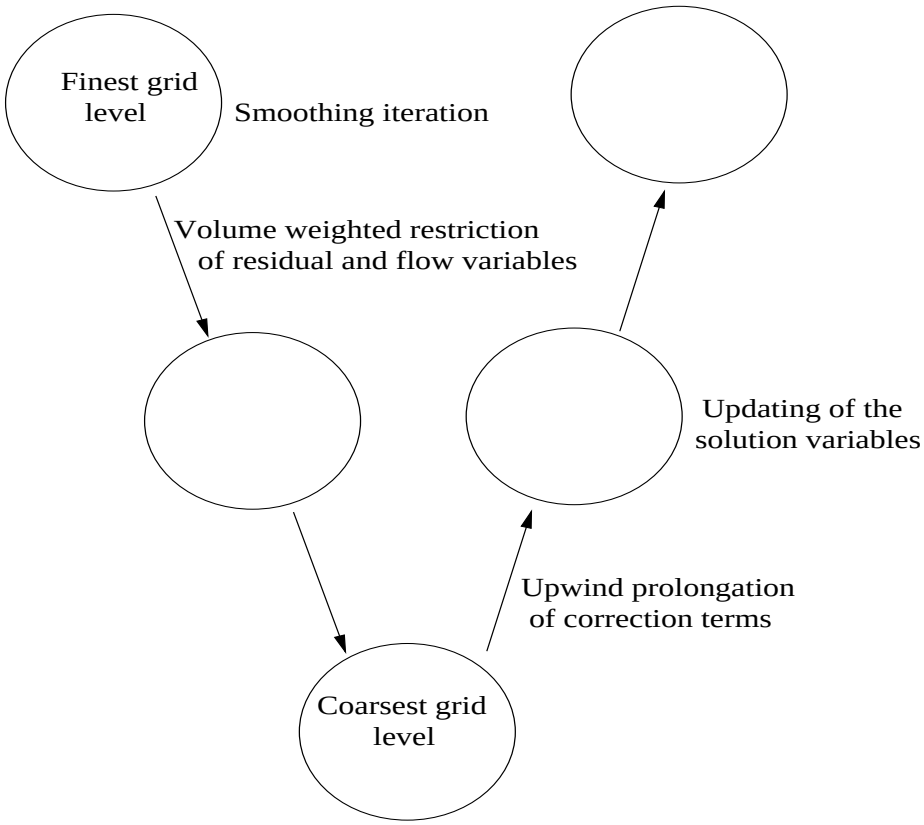

Figure 17: V-cycle employed for Multigrid algorithm

The *relative truncation error* is defined as

$$\tau_k = Res(Q_k^n) - Res_k^n - I_{k+1}^k(\tau_{k+1}) \tag{56}$$

Upwind prolongation [70] is used for transferring the correction from the coarser to next fine level grid in order to improve the stability and convergence behaviour of the Multigrid method.

$$\frac{\partial}{\partial t}\Delta Q_{k+1}^n + \nabla F(Q_{k+1}^n + \Delta Q_{k+1}^n) - \nabla F(Q_{k+1}^n) = 0 \tag{57}$$

The correction term used to update the solution on the finer grid level is defined by

$$Q_{k+1}^{n+1} = Q_{k+1}^n + \Delta\tilde{Q}_{k+1}^n. \tag{58}$$

3 Results and Discussion

3.1 Simulation of the flow field over SFB profile in cruise configuration

3.1.1 European Transonic Wind-tunnel (ETW) Experiment

In the framework of the High Reynolds Number Aero-Structural Dynamics project (HIRE-NASD), an experimental set up has been configured to conduct aeroelastic wind tunnel testing over a supercritical wing with the flow parameters in the realistic flight regime corresponding to the cruise condition [11, 20, 21].
The objectives of this experiment are to understand;

- the transonic flow field about aeroelastic equilibrium configuration of the elastic wing model,
- aero-structural dynamic processes during vibration excitation,
- aerodynamic damping mechanisms,
- unsteady interaction between shock and boundary layer,
- unsteady flow separation leading to the onset of shock buffet.

Geometrically, the elastic wing model is created by staggering of the BAC 3-11/RES/30/21 cruise flight profile. The pressure surface of the profile at the root is relatively thicker to achieve 15% of the chord length. The profile is gradually tapered in the first wing section along the span direction and conforms with the two-dimensional profile in the rest part of the wing. The maximum thickness is 11% of the chord length [11].
High Reynolds number flow condition is achieved in the European Transonic Wind tunnel under cryogenic conditions. The flow parameters affecting the aeroelastic behaviour such as Mach number, Reynolds number and dynamic pressure can be varied independently. The detailed geometrical shape and size of the wing model with its material characteristics, the wind tunnel experimental set up, dynamical qualifying of the model, flow conditions set during the experiments and the data acquisitions process are explained in Ballmann *et al.* [11]. Before the tests with the described wing model, pre-tests were performed with an airfoil in the KRG cryogenic tunnel at DLR Goettingen.
The experimental data of the surface static pressure distribution recorded in these pre-tests in the mid-section of the model from the sensors and the aerodynamic coefficients (C_L, C_d) over the profile are used to validate the results from the computational simulations described in the subsequent subsections. The computational model used for the simulation is two-dimensional.

3.1.2 Validation with the KRG experimental data

Case 39: $M_\infty = 0.749$ $\alpha = +1.0^\circ$ $Re = 20.17 Million$

Computational domain and grid

The computation is performed at the flow condition corresponding to the configuration No. 39 of the KRG experiment. The free stream Mach number, angle of attack are set to $M_\infty = 0.749$ and $\alpha = +1.0^\circ$, respectively. The Reynolds number based on the chord length is 20.17Million. The computational domain is discretised with a relatively coarse grid using "C" topology which comprised twelve blocks. The domain is extended to 20 chord lengths away along the leading and trailing edges of the profile to reduce the effect of the wake at the boundary for possible improvement in the imposition of the boundary condition. The upper and lower wind tunnel walls are not numerically modelled and free stream boundary condition with auto-detection is imposed at the corresponding computational boundaries. The domain is initially discretised with a number of 3452 quadrilateral cells. The initial grid is unstructured due to the presence of non-matching grid points between the grid blocks at the block interfaces. The presence of hanging nodes at the initial level grid and their subsequent generation during grid adaptation can be efficiently dealt with the solver, Quadflow.

3.1.2.1 Computational set up The flow is assumed to be fully turbulent, without tripping point for transition being specified. Turbulence is modelled using the original one equation Spalart-Allmaras model, as previously described in the numerical modelling section 2.3.2. Imposition of the characteristic boundary condition is found to be ineffective in achieving a desired level of convergence due to the presence of wakes reaching the boundary, generated during viscous flow simulation. Hence, extrapolation type boundary condition as described in section 2.7 is imposed. A transonic flow field with the presence of a strong shock and boundary layer is expected in the computational domain. Flow variables are reconstructed using the Green-Gauss method to achieve a second order spatial accuracy for improved resolution of the flow features. The limiter designed by Venkatakrishnan [75] described in the numerical modelling section is used to satisfy the Total-Variation-Diminishing (TVD) condition during numerical simulation. The limiter is frozen after the residual is dropped to three orders from the initial level in order to prevent its flipping for achieving a converged solution. Convective flux discretisation is carried out using the upwind HLLC scheme. Viscous flux is estimated using the central scheme with corrected gradient as outlined in the subsection 2.6.2. Implicit time integration scheme (B2) formulated by Batten & Leschziner [45] is used for temporal discretisation. The Jacobian matrix originated during the linearisation process is computed using the analytical scheme, as described in the subsection 2.8. First order reconstruction is used to evaluate the convective fluxes during the formulation of the Jacobian matrix. The maximum CFL number to be evolved in the computational domain during the simulation is limited to 50, with the initial value set to

1. The CFL number is geometrically progressed with a factor of 1.2. Higher CFL number at the initial phase is observed to be creating numerical instability in the computation. A single Newton iteration is applied within the timestep during the linearisation of the non-linear system of equations arisen from the implicit formulation. The resulting system of linear equations is solved by applying preconditioned restarted GMRES method by providing for Quadflow an interface to an external mathematical library (PETSC) [77]. Preconditioning matrix is formed from the Jacobian matrix using Incomplete Lower-Upper (ILU (2)) technique with second level of filling. Maximum number of search vectors for the KSP iteration is limited to 20 with 2 levels of restart. The targeted convergence level of the residual for the linear iteration is set to 10^{-4}. The convergence is always achieved within the prescribed GMRES steps in all the computations described in the subsequent section.

Seven levels of grid adaptation are carried out in order to obtain the fully converged mesh-independent solution. The criterion is set such that the adaptation is activated, when the residual in density reaches five orders decrease with respect to the initial value.

The computations are performed in the High Performance Sun Cluster of the Rechenzentrum, RWTH, Aachen.

3.1.2.2 Solutions Figs. 18 a) and b) show the convergence behaviour and the variation of number of cells in the domain of adaptation. Seven levels of grid adaptation are performed with grid being adapted after every successive drop of residual to a prescribed value at the current grid level. The indicator to monitor the convergence behaviour is computed at every iteration

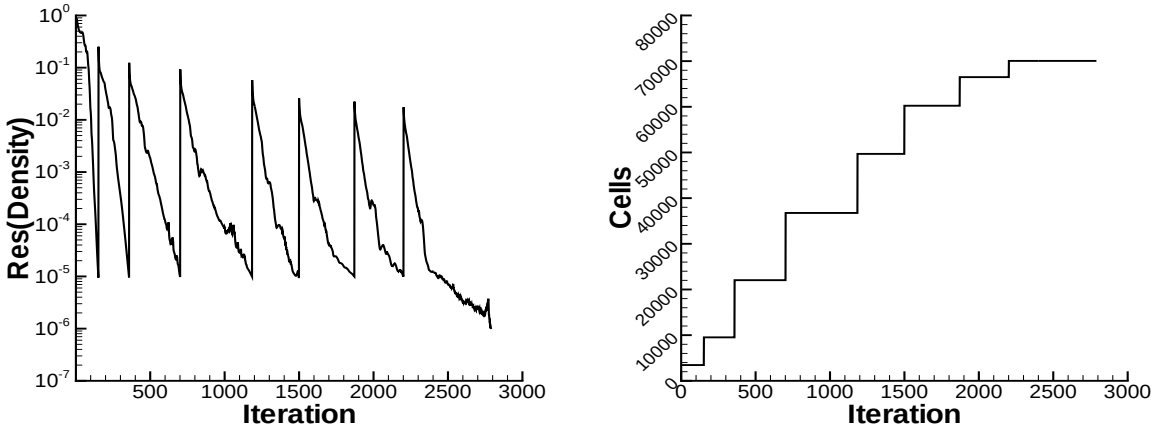

a) Residual fall b) Variation of cell number

Figure 18: Convergence behaviour, variation of cell number in the computational domain

based on the root mean square value of the density residual of the control volume cells in the computational domain. Solution at the intermediate grid level is obtained after five levels fall of the initial residual, which is set as the required intermediate convergence level in the form of input parameter to the adaptation module. The final solution is converged sufficiently on the

finest grid level.

A monotonous decrease in the residual is achieved during the computation. The residual jumps back to a relatively large value after every grid adaptation, as it is reinitialised and keeps on decreasing when the flow solution is gradually developed at the current grid level. Approximately 2700 iterations are required to obtain the final converged solution for the case under consideration, as shown in Fig. 18 a).

Fig. 18 b) shows the variation of the number of cells in the computational domain due to the grid adaptation during the simulation. The number varies significantly as the flow develops during the initial phase of computation and gradually achieves convergence at the final phase of the simulation. The grid at the initial level has 74 cells on the airfoil profile. Cells in the high activity regions of the computational domain are refined and the final level grid has 2621 cells on the profile.

The utilisation of grid adaptation method drives the computation in achieving a grid independent solution, as observed with minimal increase in the number of cells achieved during the final stage.

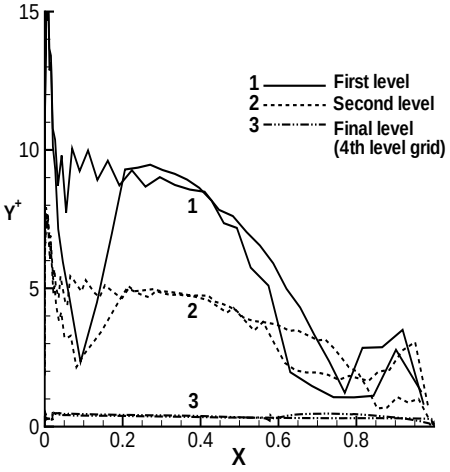

Figure 19: y^+ variation

Fig. 19 shows the gradual reduction of y^+ at different grid levels as the flow solution is developed. The value of y^+ at the initial grid level with the coarse mesh remains close to ten and gradually decreases with adaptation before reaching a value below unit along the profile at the finest grid level.

Lift and drag coefficients obtained from the computation are compared with the experimentally obtained data [23]. Lack of pressure sensors at the leading edge of the airfoil prevents an accu-

Method	C_L	C_d
Exp.	0.4412	0.0090
Comp.	0.4858	0.0097

Table 1: Surface integral parameters

rate capture of the peak in the surface pressure distribution during the experiment [11]. Hence, some deviation in the computationally predicted value with the experimental data is observed.

Part of the observed variation can be attributed to the difference in the results from a two-dimensional computational model and neglecting the modelling of the upper and lower wind tunnel walls. The drag coefficient estimated from the computation is closer to the experimental

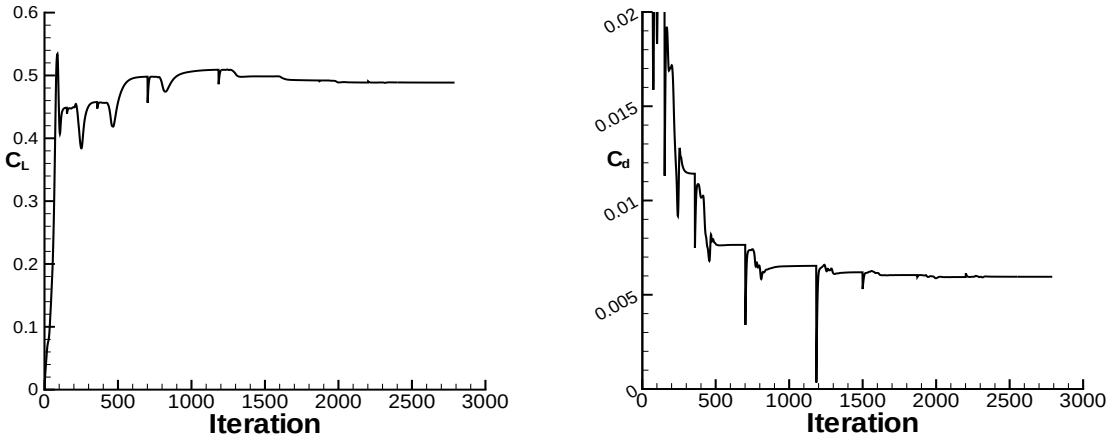

a) Lift coefficient b) Drag coefficient

Figure 20: Convergence of C_L, C_d during simulation

value within 1% variation.

Evolution of the lift coefficient (C_L) and drag coefficient(C_d) with iteration are shown in the Fig. 20 a) and b), respectively. The integral aerodynamic coefficients undergo significant change during the initial phase before achieving steady converged values at the final stage of the computation.

The finest grid level and the corresponding surface y^+ distribution are shown in the Figs. 21 a) and b), respectively. Achievement of profile y^+ value below unit is required to accurately capture the flow field as low reynolds number model approach is used for resolving the boundary layer flow.

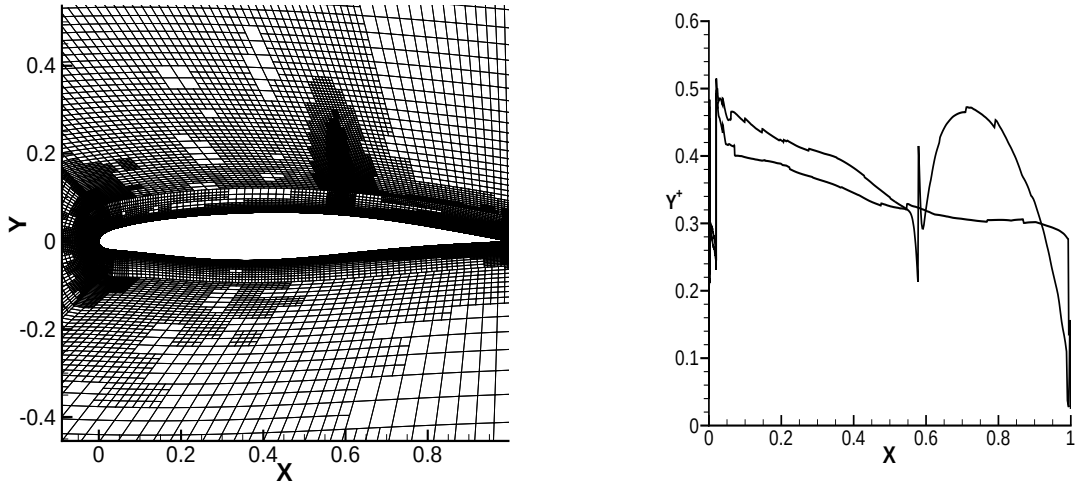

b) Final level adapted grid a) y^+ variation at the finest level

Figure 21: y^+ distribution and final adapted grid in the computational domain

Grid is adapted in the regions containing the flow features with large scale spatial variation. These high-activity regions include the stagnation region closer to the leading edge, the boundary layer, the shock on the suction surface and the viscous wake behind the trailing edge. The localities of the flow features generated due to different mechanisms (inviscid phenomenon, e.g. shock and viscous flow feature, e.g. boundary layer) are accurately detected by the adaptation module. This shows the effectiveness and reliability of the multiscale algorithm based on the wavelet analysis, used as the basis of adaptation criterion for properly detecting the flow features in the domain and adapting the grid subsequently.

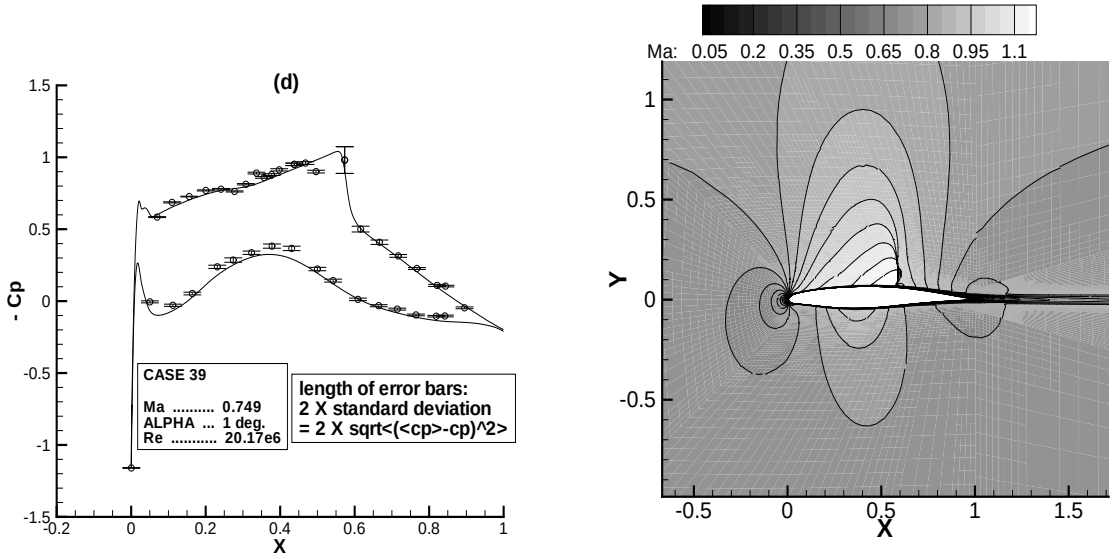

a) Cp distribution

b) Mach number variation in the domain

Figure 22: C_p distribution and Mach number contours in the computational domain with the finest level grid

Fig. 22 compares the variation of surface static pressure coefficient along the profile with the experimental data [23]. Sensor data points obtained during the experiment are in excellent agreement with the computational result. Variation of Mach number in the computational domain in the finest level adapted grid is shown in the Fig. 22.

Computations are performed in a similar manner to resolve the flow field generated under different flow conditions and are compared with the experimental data.

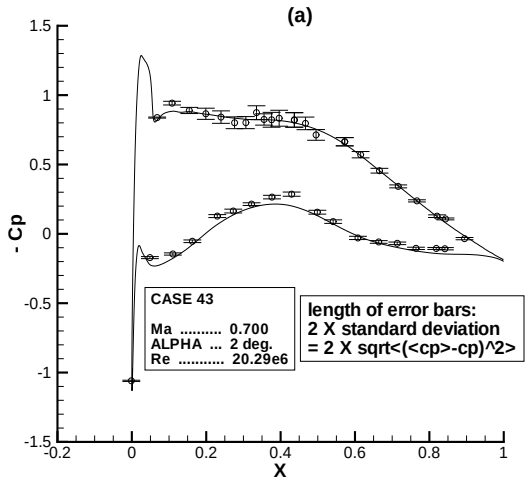

Case 43

$M_\infty = 0.7$, $\alpha = 2^\circ$,

Re=20.29e+6

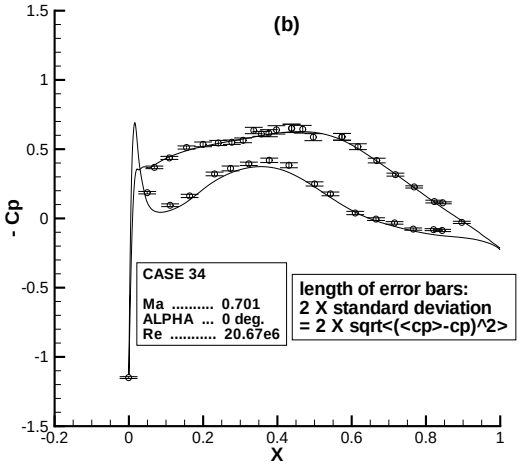

Case 34

$M_\infty = 0.701$, $\alpha = 0^\circ$,

Re=20.67e+6

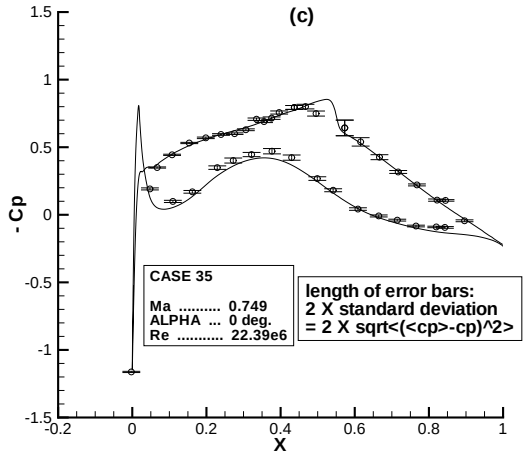

Case 35

$M_\infty = 0.749$, $\alpha = 0^\circ$,

Re=22.39e+6

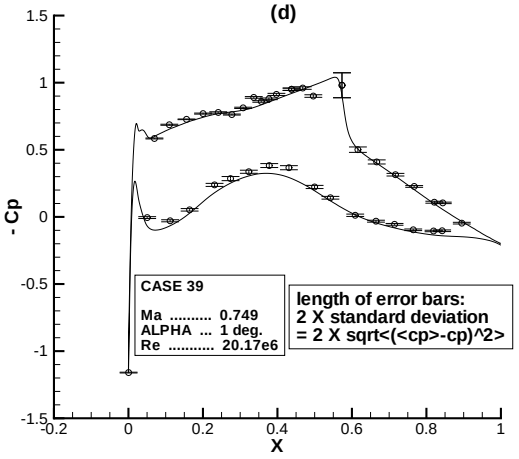

Case 39

$M_\infty = 0.749$, $\alpha = 1^\circ$,

Re=20.17e+6

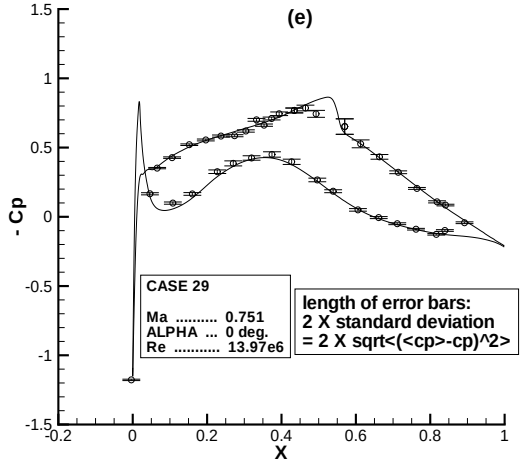

Case 29

$M_\infty = 0.751$, $\alpha = 0^\circ$,

Re=13.97e+6

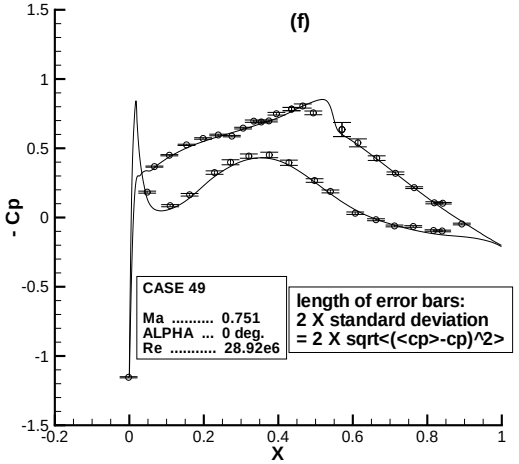

Case 49

$M_\infty = 0.751$, $\alpha = 0^\circ$,

Re=28.92e+6

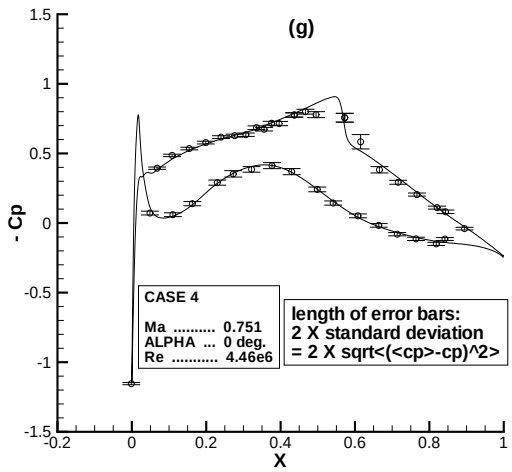

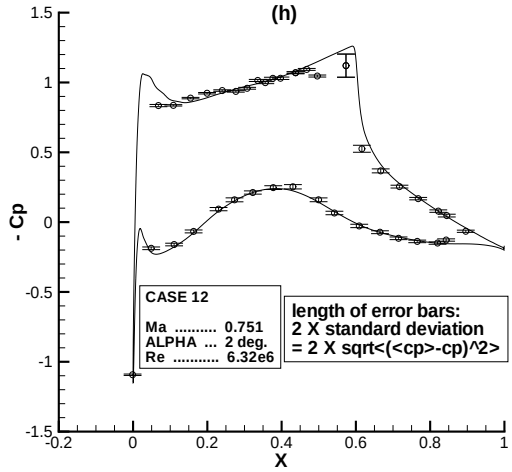

Case 4
$M_\infty = 0.751$, $\alpha = 0^\circ$,
Re=4.46e+6

Case 12
$M_\infty = 0.751$, $\alpha = 2^\circ$,
Re=6.32e+6

Consistent results are obtained throughout the computations as shown in the above figures. The computational results obtained using adaptive numerical simulation are in excellent agreement with the experimental data. The results shown in this section validate the application of adopted numerical modelling techniques implemented in the flow solver, Quadflow for simulating the flow field over the airfoil profile in cruise configuration.

3.1.3 Simulation of the flow field with Zonal DES

3.1.3.1 Convergence acceleration with Zonal DES Computational results shown in the subsection 3.1.2 are obtained with the turbulent flow structures modelled using the one equation originl Spalart-Allmaras model. The accuracy of the modelling schemes and their implementation in Quadflow is demonstrated through validation with the experimental data. Further computations carried out using the DES model in order to compare with the original S-A simulations are described in the current section. The implementation detail of the DES model is outlined in the numerical modelling section 2.3.4 of this thesis.

Simulations are carried out using the original S-A model and the DES model corresponding to the flow configuration of the Experiment No. 20 of the KRG experimental set up. The free stream Mach number, angle of attack and the Reynolds number of the flow are set to 0.682, $+0.0^\circ$ and 8.2 Million, respectively. The set of input parameters such as convergence level, number of grid adaptation and the initial grid are kept identical in both the cases. Converged solutions corresponding to the finest grid level are obtained in both the computations. The number of iterations required to achieve the corresponding level of adaptation, number of cells in the computational domains and converged integral aerodynamic coefficients obtained during the computations are shown in the tables 2 and 3.

It is observed from the numerical experiment that the DES model significantly improves the convergence acceleration as compared to the RANS simulation, for an identical set of input parameters.

Adaptation modifies the number of cells in the computational domain depending on the solution in the flow field. A small difference in the solution obtained using DES and S-A RANS formulations causes a different evolution of cell numbers. Hence, instead of comparing the number of iterations for determining the efficiency of computations, a parameter called *workunit* is defined, which provides a rough estimate of the amount of total computational work required during the simulations. It is defined by aggregating the multiplication of the number of cells in the domain with the number of iterations required during every adaptation.

$workunit = \frac{1}{n+1}\sum_{i=0}^{i=n} Cell[i] * (itn[i+1] - itn[i] + 1)$, where itn[0]=1 ..., n= number of adaptations

Case 20: $M_\infty = 0.682 \qquad \alpha = +0.0^\circ \qquad Re = 8.2Million$

Experimental Result: $C_L = 0.2377, C_d = 0.0076$ [23]

Adap.	Itn.	Cell	C_L	C_d
1	140	3452	2.854112e-01	1.367596e-02
3	672	26000	2.962130e-01	7.543762e-03
5	1504	75848	2.943549e-01	8.331507e-03
8	3177	147188	2.852171e-01	8.294309e-03

Table 2: Original SA model, Workunit=33263511.8750

Adap.	Itn.	Cell	C_L	C_d
1	119	3452	2.851499e-01	1.371125e-02
3	490	26039	2.942121e-01	7.535204e-03
5	903	72800	2.924266e-01	8.277477e-03
8	1487	135785	2.863193e-01	8.274408e-03

Table 3: DES model, workunit=13156495.500, 2.5 times faster

For the case shown above, the workunit required for RANS simulation is 2.5 times higher compared to the DES simulation. Similarly, for all other computations carried out (not shown in the thesis) during the comparison, it is observed that computational expense for the RANS simulation as expressed in the work units is at least a factor of 1.8 times higher than the DES simulation.

Another point worth noting that, the variation between aerodynamic coefficients obtained from a fully converged finally adapted mesh with RANS and DES simulations are insignificant, as the flow field is steady and the boundary layer remains attached to the airfoil surface.

3.1.3.2 Effect of zonal dimension parameter of DES on convergence and solution accuracy The formulation of Zonal DES as outlined in the numerical modelling section of the thesis (section 2.3.5), contains a free parameter (K_w) expressed as the percentage of the chord length to separate the regions of the domain where RANS modelling remains active from the localities modelled with the modified RANS. Any cell with a wall distance larger than the limit set by the free parameter has its wall distance modified according to the maximum size of the grid in the coordinate directions and becomes part of the domain modelled with modified RANS model. The cell staying inside the defined boundary close to the surface stays unmodified and the turbulence is modelled with the original RANS formulation.

In the absence of such a boundary demarcated to separate the above mentioned two regions, the modified wall distance ($\max(\Delta x, \Delta y)$) becomes smaller with every grid adaptation, as the dimension of the cells decreases due to the refinement. The dependency of the wall distance solely on the grid size would lead to an under-estimation of the wall distance in the presence of highly refined cells in the boundary layer close to the surface. The stretched cells with high aspect ratio in the vicinity of the surface wall prevents the occurrence of the above phenomenon to a certain extent. As the aspect ratio of the cells decreases when moving away from the wall, there is a possibility of the modified RANS model entering into the boundary layer close to the surface wall. The situation creates an erroneous model with the wall distance of the cells very close to the surface is reduced significantly, creating an increase in the destruction term of the RANS model. In this scenario, the eddy viscosity becomes too small (due to the increase in the destruction term in RANS modelling) and the numerically predicted aerodynamic coefficients become small. Hence, the turbulence modelling is neither RANS nor LES, as the grids in the localities close to the surface are not originally designed for the Sub-Grid-Scale modelling. Therefore, in order to avoid the modified RANS model entering into the boundary layer domain, it is necessary to demarcate the boundary in order to separate the two regions.

The current section is devoted to study the effects of the size of the specified boundary on the computational convergence and solution accuracy.

Experiment No. 43 from the KRG experimental set up is considered as a case study for the investigation. Simulations are carried out with the flow parameters corresponding to experiment No. 43. Case 43: $M_\infty = 0.700 \qquad \alpha = +2.0^\circ \qquad Re = 20.29 Million$

Experimental Result: $C_L = 0.5136, C_d = 0.0080$ [23]

Three different values of the zonal boundary specification parameter (expressed as the percentage of the chord length) are considered in the numerical testing, as shown in the table 5. The cells in the computational domain out of the presecribed distance from the airfoil surface are treated for the wall distance modification. Any cells within the imposed boundary near to the airfoil surface are considered as part of the boundary domain and kept unmodified.

Computation carried out using original S-A RANS model with similar computational parameters are obtained for comparison. Fig.23 shows the comparison of the convergence behaviour

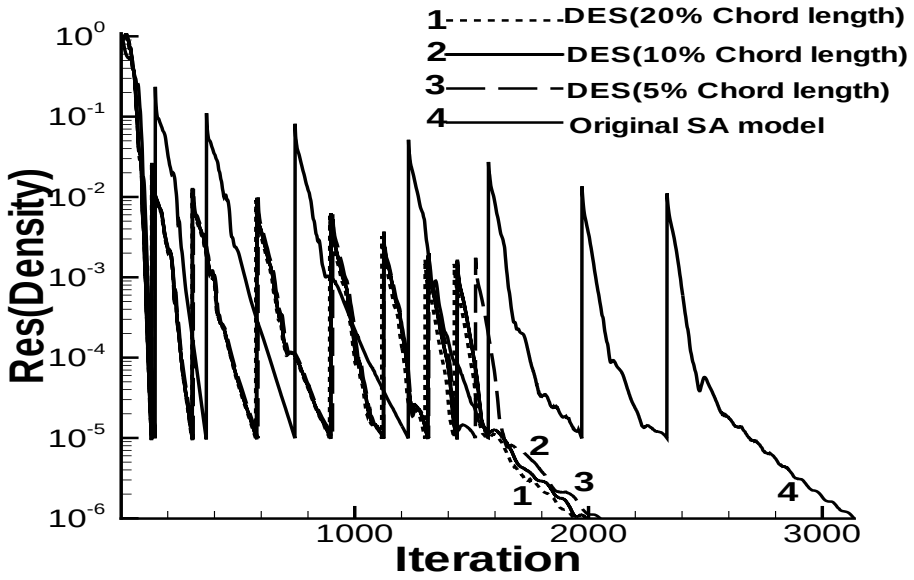

Figure 23: Effect of zonal boundary parameter in DES model on the convergence

Dim.	Itn	Cell	C_L	C_d
20%	1937	128621	0.5928	8.407e-03
10%	1989	129941	0.5925	8.394e-03
5%	2050	129824	0.5920	8.388e-03

Table 4: DES model with varying boundary zone specification parameter

achieved using modified formulations with the original S-A model. It is observed that the number of iterations required to obtain a final converged solution with the modified formulations are smaller than the original formulation.

Itn	Cell	C_L	C_d
3136	138266	5.929e-01	8.427e-03

Table 5: Original SA model

The number of iterations required to obtain a fully converged solution at the finest level grid is not significantly affected by the length of the demarcation domain. The number of iterations required to obtain the converged solution, number of cells in the final level grid and converged aerodynamic coefficients obtained at the finest level are shown in the table 5. The boundary zone dimension has very minor effect on the solution accuracy and convergence behaviour.

3.1.4 Aerodynamic characteristics of the SFB profile in cruise condition

Several computations have been performed with 3 different Mach numbers, 6 different angles of attack and 4 different Reynolds numbers for studying the aerodynamic characteristics of the SFB 401 airfoil.

Free stream Mach number is chosen among the range, $M_\infty \in [0.65, 0.70, 0.75]$ in steps of 0.05,

Angle of attack is chosen from the set, $\alpha \in [-1.0^\circ, -0.50^\circ, 0.0^\circ, 1.0^\circ, 2.0^\circ, 2.5^\circ, 3.0^\circ]$,

Reynolds number, $Re \in [4.0 \times 10^6, 12.0 \times 10^6, 20.0 \times 10^6, 30.0 \times 10^6]$.

Numerical simulation is performed over the initial grid using the computational parameters identical to the cases discussed in the previous subsection. Spalart-Allmaras turbulence model with modification for DES is used to model the effect of turbulence.

3.1.4.1 Effect of flow parameters on the maximum Mach number in the computational domain Table 6 shows the maximum Mach number achieved in the computational domain during the computations. This gives an idea of the strength of the shock in the computational domain.

α/Mach	0.65		0.70		0.75	
	4.0×10^6	30.0×10^6	4.0×10^6	30.0×10^6	4.0×10^6	30.0×10^6
-1.0	1.08	1.095	1.292	1.329	1.386	1.409
+1.0	0.912	0.926	0.993	1.008	1.263	1.268
+2.0	1.144	1.174	1.213	1.229	1.319	1.353
+2.5	1.240	1.260	1.278	1.295	1.342	1.381

Table 6: Maximum Mach number in the computational domain

Maximum Mach number in the domain increases with the increase in the free stream Mach number (M_∞). At a particular M_∞, inertial force becomes dominant with the increase in the Reynolds number and the local Mach number in the computational domain is increased. At a specific Mach number and Reynolds number, with positive increase in the angle of attack, the flow gets accelerated on the suction surface of the profile and a supersonic region is created. The maximum Mach number achieved on the suction surface increases with the increment in the angle of attack. The termination of the supersonic region on the suction surface is exhibited in the form of a shock in the flow field and the shock strength increases with the increase in the angle of attack. The surface profile curvature on the pressure surface near the leading edge creates a mild shock to appear on the pressure surface near the leading edge at negative angle of attack of the free stream flow.

Study of dependency of the lift coefficient(C_L) on α with variation in M_∞ at a specific Reynolds number

C_L shows an expected linear trend with α in the lower range of the angle of attack. The increase

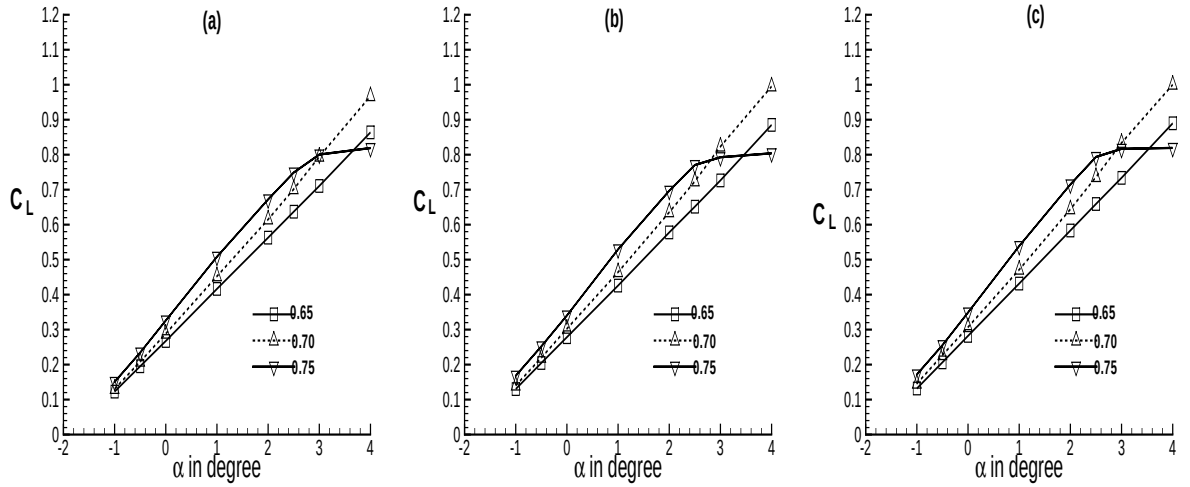

a) $Re = 4.0 \times 10^6$ b) $Re = 12.0 \times 10^6$ c) $Re = 30.0 \times 10^6$

Figure 24: Dependency of the lift coefficient(C_L) on angle of attack (α) at different free stream Mach numbers(M_∞) and a specific Reynolds number

in the inertial force in the flow field as a result of increase in the M_∞ and Reynolds number at a particular angle of attack creates a positive shift in the C_L. The influence of the free stream Mach number on the lift coefficient is predominant compared to the effect of the Reynolds number. The flow separation and associated decrease in the lift coefficient is observed at a higher α. The loss of lift at the inception of the stall is observed at a larger M_∞. Corresponding computations are characterised with non-convergence of the flow field and periodic fluctuation of the C_L. Mean value of the lift coefficient is observed to be reduced.

Study of drag polar with variation in M_∞ at a specific Reynolds number As expected, higher

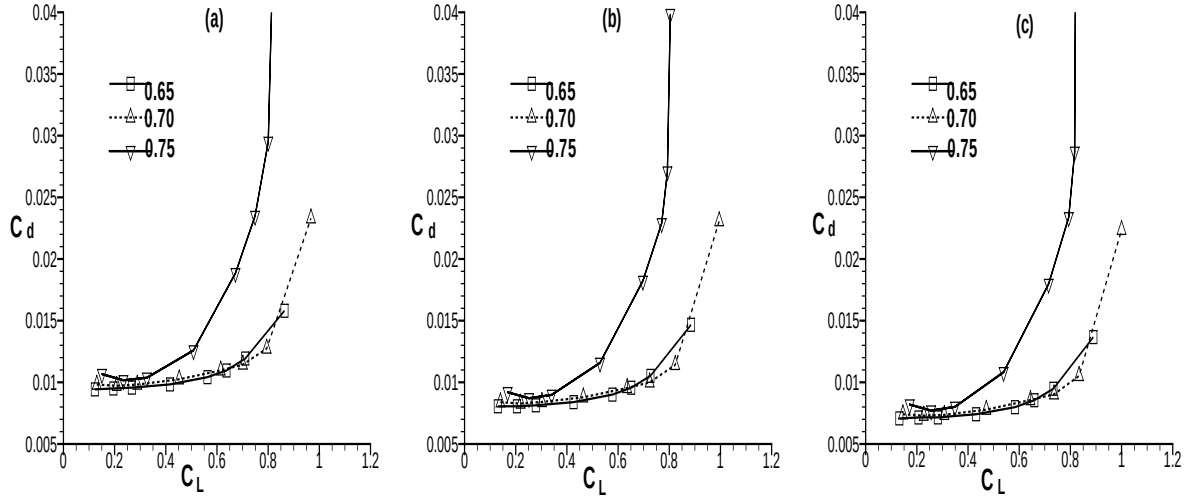

a) $Re = 4.0 \times 10^6$ b) $Re = 12.0 \times 10^6$ c) $Re = 30.0 \times 10^6$

Figure 25: Drag polar

M_∞ causes simultaneous increase in C_L and C_d. The variation of C_L with C_d is in agreement with

the usual trend. The rapid increase in C_d at a relatively high M_∞ is due to the flow separation associated with the inception of stall causing an increase in the wave drag.

Study of dependency of Lifting efficiency (L_e) on α with variation in M_∞ at a specific Reynolds number

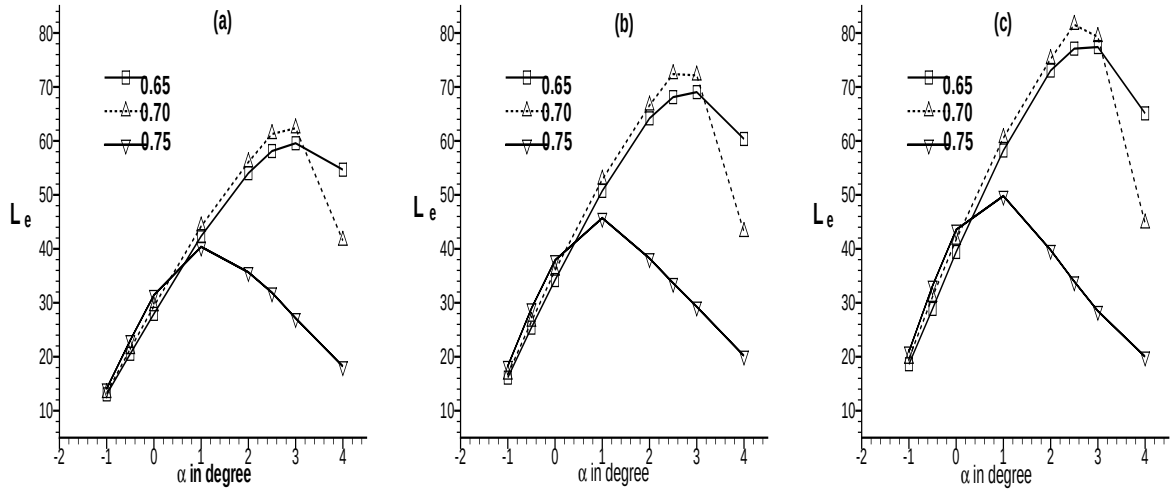

a) $Re = 4.0 \times 10^6$ b) $Re = 12.0 \times 10^6$ c) $Re = 30.0 \times 10^6$

Figure 26: Dependency of the Lifting efficiency on α at different M_∞ and a specific Reynolds number

Lifting efficiency(L_e) is defined as the ratio between C_L and C_d. In the region of relatively smaller α, L_e is higher with high M_∞. Increase in α causes rapid increase in C_d compared to C_L at a higher M_∞. This causes L_e undergoing a drastic reduction at a relatively higher angle of attack.

Study of dependency of C_L on α with variation in Reynolds number at a specific M_∞

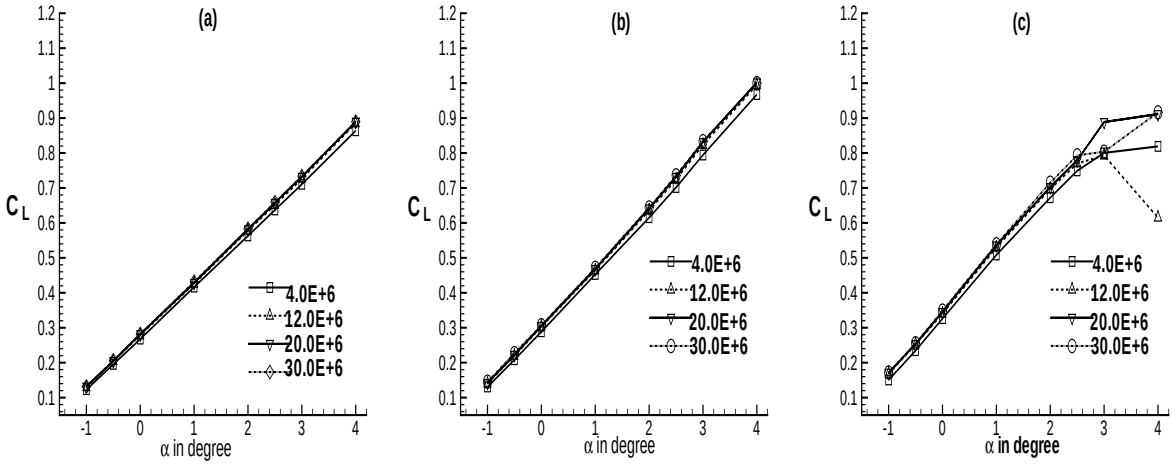

a) $M_\infty = 0.65$ b) $M_\infty = 0.70$ c) $M_\infty = 0.75$

Figure 27: Dependency of the lift coefficient on α with variation in Reynolds number at a specific M_∞

The inertial effect of the flow field increases with the rise in the Reynolds number. Hence, C_L increases with increase in Reynolds number, albeit to an insignificant amount. The effect of Reynolds number on the lift coefficient is negligibly small, except at higher angle of attack.

Study of Drag polar with variation of Reynolds number at a specific M_∞

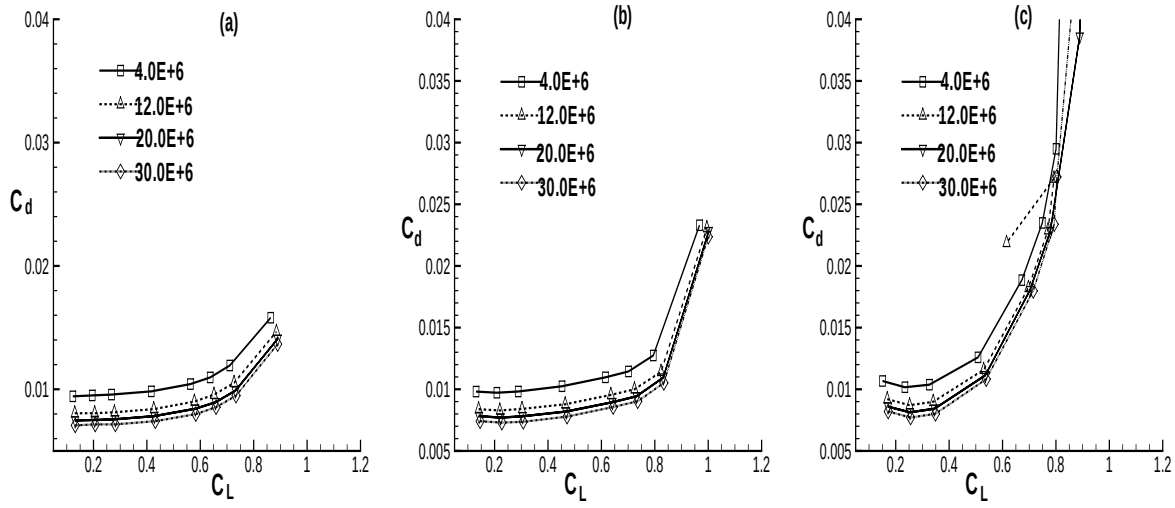

a) $M_\infty = 0.65$ b) $M_\infty = 0.70$ c) $M_\infty = 0.75$

Figure 28: Drag polar with variation of Reynolds number at a specific M_∞

Decrease in the Reynolds number increases the viscous effect for any flow configuration with a specific lift coefficient. The increase in the viscous drag causes an overall increase in the drag coefficient. Hence, decrease in the Reynolds number is associated with the increase in the total drag coefficient for any M_∞.

Study of dependency of L_e on α with variation in Reynolds number at a specific M_∞

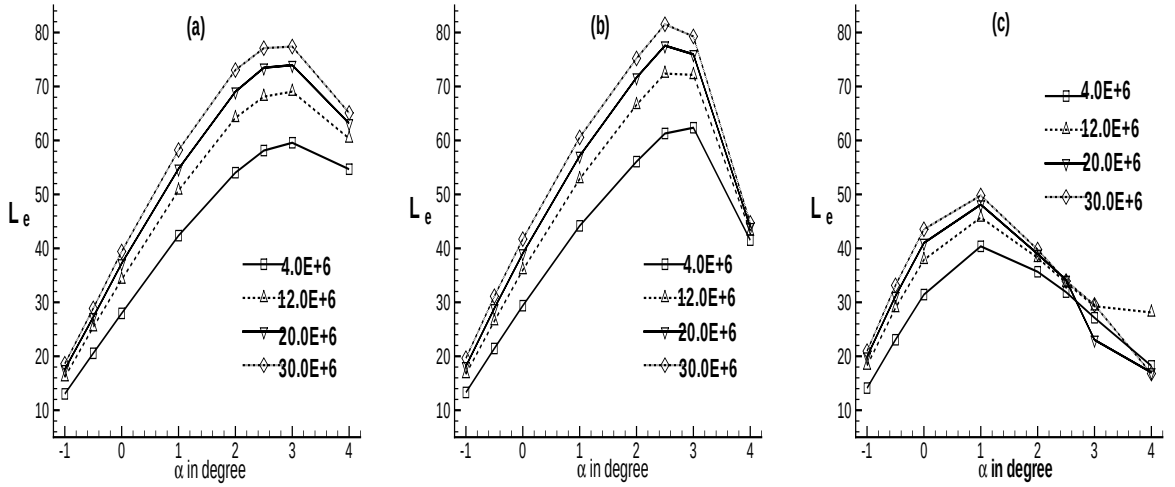

a) $M_\infty = 0.65$ b) $M_\infty = 0.70$ c) $M_\infty = 0.75$

Figure 29: Dependency of L_e on α with variation in Reynolds number at a specific

Higher Reynolds number increases the dominance of the inertial force in the flow field over

the viscous force. Inertial force contributes positively to the lift coefficient. Drag coefficient undergoes a reduction due to the decrease in the viscous effect. Both the factors complement each other at a higher Reynolds number in increasing the lifting efficiency. Hence, for a flow configuration with specific M_∞, increasing the Reynolds number has a positive effect on lifting efficiency(L_e).

The trend is reversed at a higher angle of attack. Separation of the flow field at a higher angle of attack results in reducing C_L and increasing C_d. The combined effects is observed as the sudden downward fall of the curve at the higher angles of attack. The early departure of the curve at a relatively higher M_∞ shows the early onset of flow separation.

Study of dependency of skin friction coefficient (C_f) on Reynolds number with variation of α *at a specific* M_∞

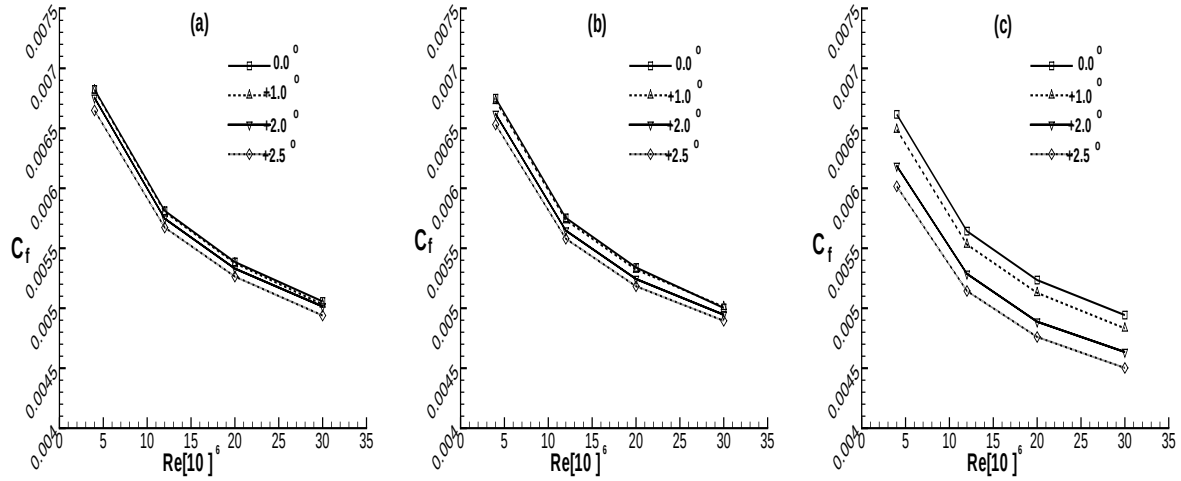

a) $M_\infty = 0.65$ b) $M_\infty = 0.70$ c) $M_\infty = 0.75$

Figure 30: Dependency of skin friction coefficient (C_f) on Reynolds number with variation of α at a specific M_∞

Increase in the Reynolds number results in the decrease in the profile drag and the trend is clearly observed. The curves show an expected closeness to the hyperbolic trend.

3.2 Simulation of the flow field over three element airfoils in high lift configuration

3.2.1 Adaptive flow simulation

This section describes the numerical simulation of the flow over multi-element high-lift profile BAC3-11/RES/30/21, which is defined as the reference configuration in the Collaborative Research Center (SFB401) for high lift investigations. It comprises a leading edge slat, the main airfoil and a single slotted flap with geometrical dimensions as described in the report by Moir [71]. The slat and flap are deflected at 25° and 20° respectively and the configuration is used to provide lift in the low speed operating regime of the aircraft during take-off and landing. The criticality in designing the configuration and complicated flow field have instigated numerous researchers [18, 47–49] to accurately predict the flow features for improved understanding of the physical phenomena. The five ideas envisaged by A.M.O. Smith [46] to characterise the flow physics over the high-lift configuration are

- The slat effect
- The circulation effect
- The dumping effect (Attaining higher discharge velocity at the trailng edge of the forward element)
- Off-the-surface pressure recovery
- The fresh boundary layer effect

Fluid at low freestream Mach number undergoes a rapid acceleration over the highly deflected slat to create a localised supersonic region at the suction surface thus producing a mixture of subsonic and supersonic regions in the computational domain. Significant variation of Mach number creates a large range of condition number in the computational domain affecting the stiffness of the numerical scheme. The wake generated from the preceeding element interacts with the boundary layer and wake of the successive elements to create a complex flow field. This mutual interaction of the wake and boundary layer depends on the angle of attack of the flow. Thus, accurate simulation and prediction of the flow over this configuration poses a significant computational challenge. Additionally, the current study uses grid adaptation during flow simulation. The initial H-grid shown in Fig. 31 is comprised of 61 blocks with 16740 quadrilateral cells. The initial level coarse grid has 408 cells located on the surface of the airfoil elements with a maximum y+ of 30. The grid is extended to 25 chord lengths along the upstream and downstream directions in order to reduce the effect of the wakes at the boundaries for improved imposition of the boundary conditions. The freestream Mach number (M_∞) and Reynolds number based on the chord length are set to 0.197 and 3.52 Million, respectively. Computations

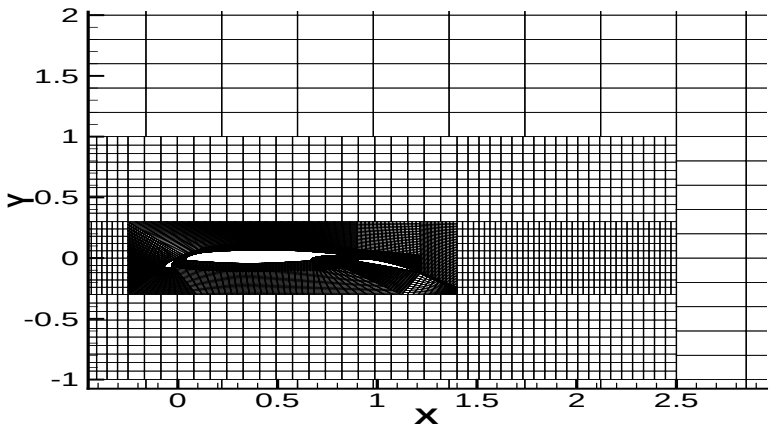

Figure 31: Initial grid in the computational domain for the high-lift configuration

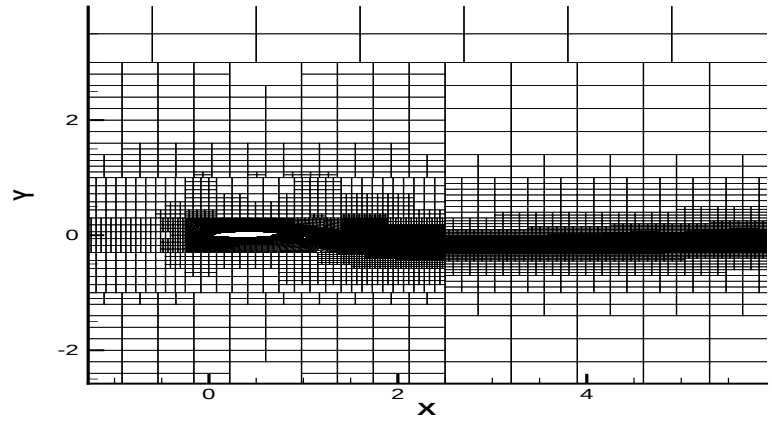

Figure 32: Final level grid, $\alpha = 4.01^{\circ}$

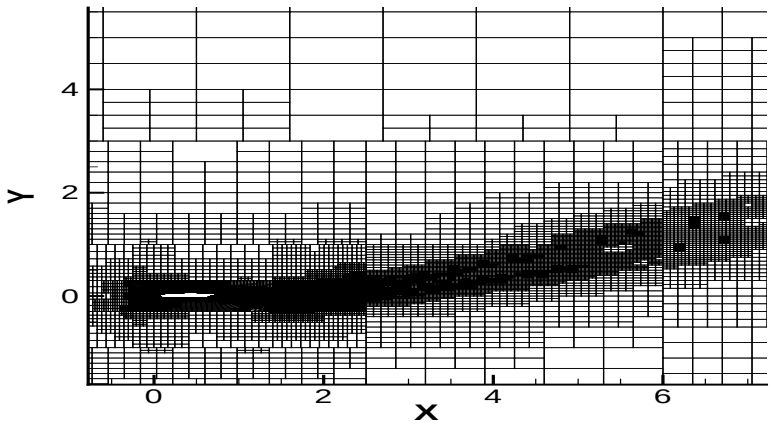

Figure 33: Final level grid, $\alpha = 20.18^{\circ}$

are carried out with turbulence modelled using original Spalart-Allmaras and Detached Eddy Simulation models. Computatiopnal domain is refined and coarsened during grid adaptation

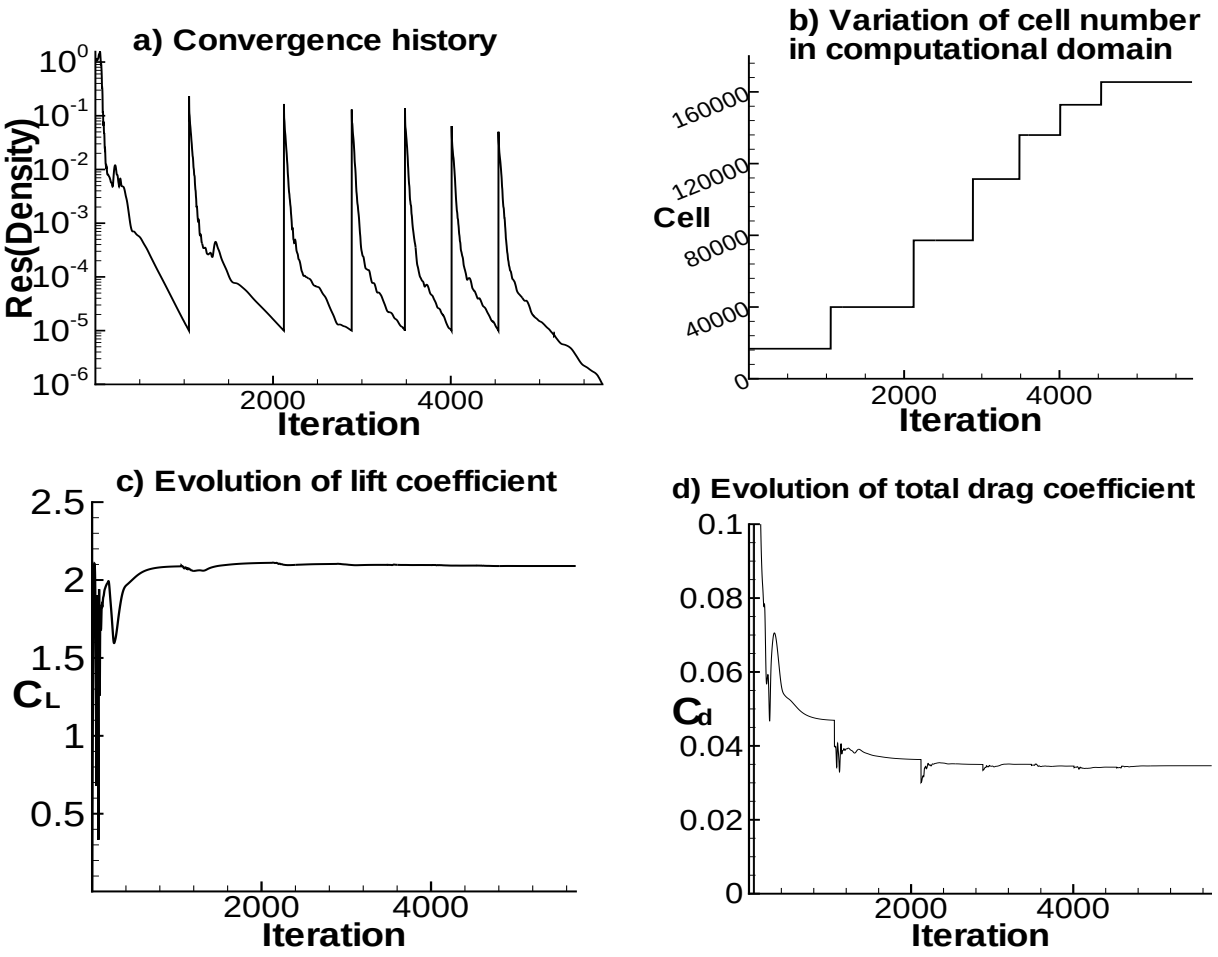

Figure 34: Convergence of simulation: $\alpha = 4.01^\circ$

depending upon the developed flow field. Figs. 32 and 33 shows the final level adapted grid in the computational domain at two different angles of attack. Though, the initial level grids for both the computations are identical, the difference in the development of the boundary layer and wake region due to the variation in the angle of attack creates a conspicuous difference in the final level grids. Grid adaptation is carried out during the iterative process when the residual in density falls five order below the initial value. Six levels of adaptation is carried out to obtain the final converged solution. The grid refinement control parameter (MST_ε) is set to 10^{-3} in order to prevent a rapid increase in the number of cells in the computational domain. Convergence of the density residuum, variation of the total number of cells in the computational domain due to the grid adaptation, evolution of the lift and drag coefficients are shown in the Figs. 34 a), b), c) and d). Fig. 35 shows the comparison of the experimentally obtained surface pressure distribution on the airfoil with the computationally obtained value during adaptive simulation, correspond to the angle of attack, $\alpha = 4.01^\circ$. The computational data are in excellent agreement

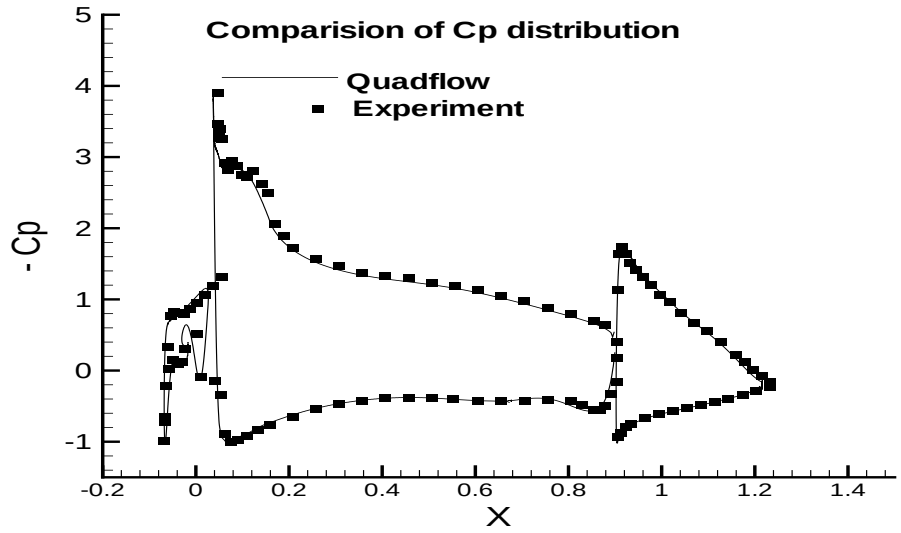

Figure 35: Surface C_p distribution on the finest grid level: $\alpha = 4.01^\circ$

with the experimental value on the slat, main element and flap airfoil surfaces. Figs. 36 a) and

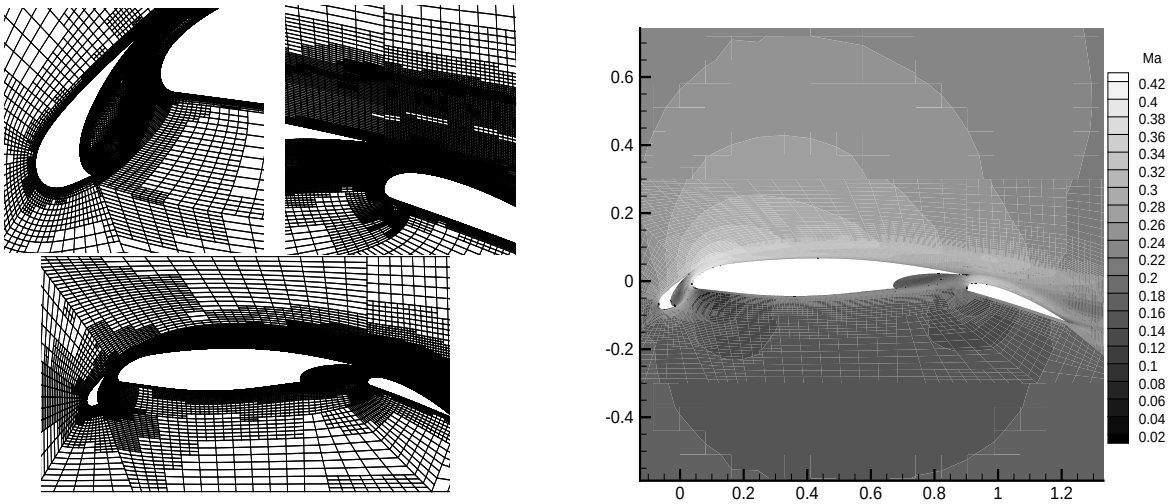

a) Details of adapted final level grid b) Mach number distribution

Figure 36: Adapted grid and flow field over the high-lift configuration at $\alpha = 4.01^\circ$

b) show the final level adapted grid and the variation of the Mach number in the computational domain at $\alpha = 4.01^\circ$. The grid is highly refined in the boundary layer and in the free shear regions along the wakes of the airfoil elements. Maximum Mach number achieved in the domain is 0.46.

An additional computation is performed at the angle of attack $\alpha = 20.18^\circ$. The residual is adequately converged to obtain the fully converged steady state solution. The convergence

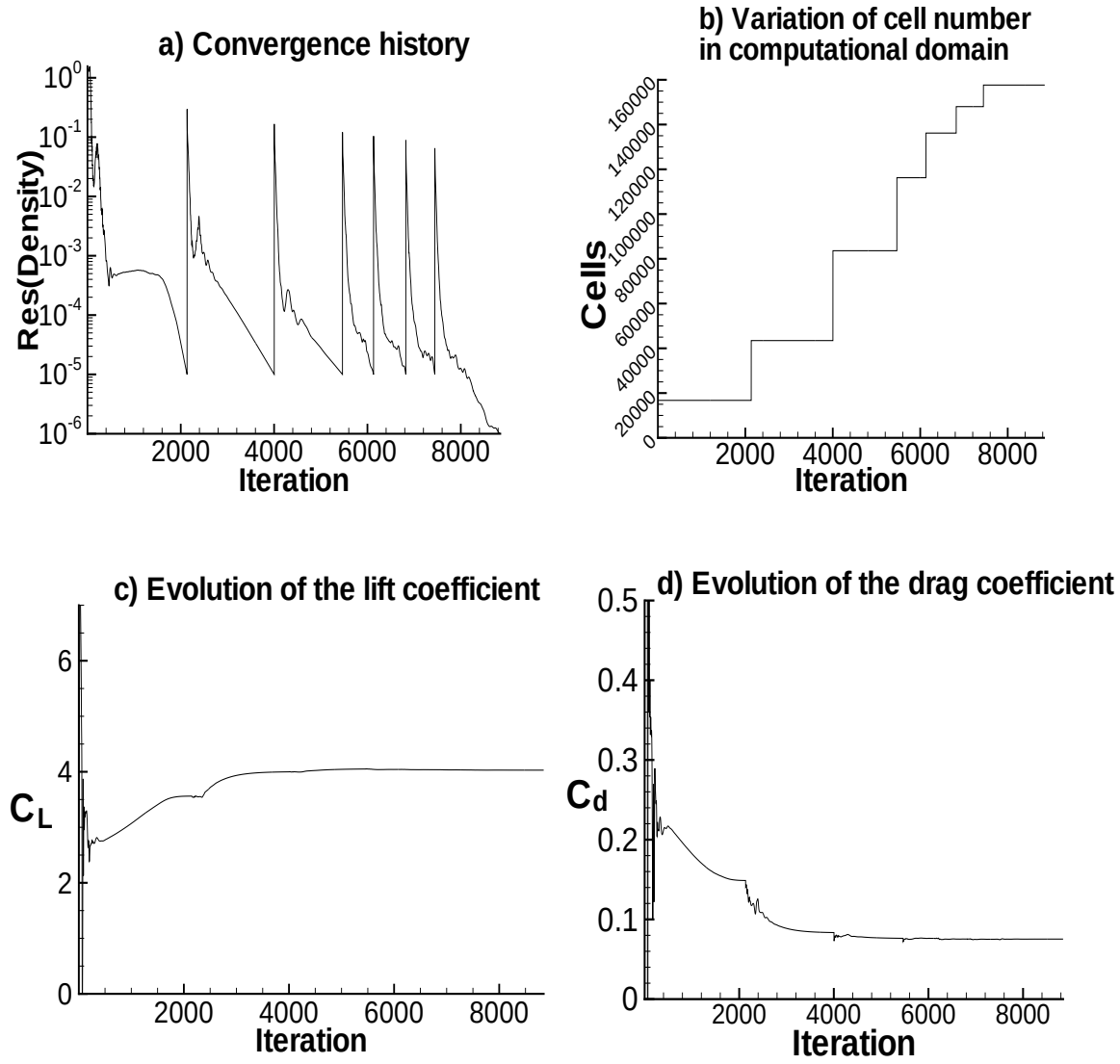

Figure 37: History of computation: Convergence, cell numbers and aerodynamic Coefficients

behaviour of the computation is shown in Figs. 37 a), b), c) and d). A rapid change in the number of cells in the computational domain is observed during initial levels of grid adaptation, as the solution gradually develops creating a significant change in the flow field. During the later phase of computation, the total number of the cells in the domain varies slowly as the solution becomes settled. Number of cells in the computational domain at the finest grid level is approximately 180000 with 1900 cells on the airfoil surface. Refinement of the cells in the boundary layer during adaptation reduces the y+ distribution on the airfoil surface and at the finest level a variation below unit is achieved. Exact number of the cells in the domain depends on the angle of attack of the flow which eventually regulates the flow field.

Excellent agreement of the surface static pressure coefficient with the experimental data are observed as shown in the Fig. 38.

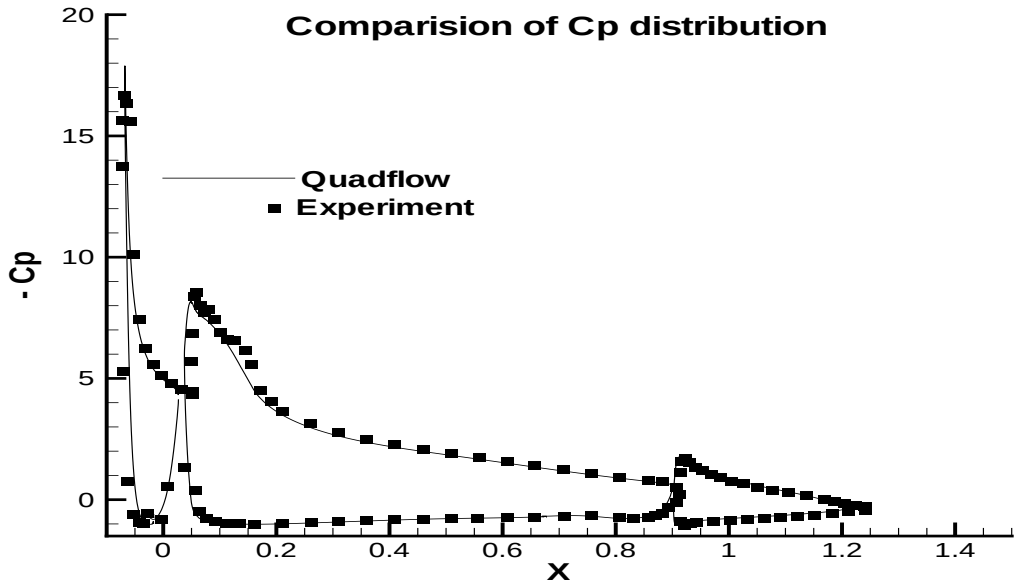

Figure 38: Surface C_p distribution on the finest grid level: $\alpha = 20.18^\circ$

Figs. 39 a) and b) show the final level grid and the variation of the Mach number in the computational domain, respectively. At the angle of attack, $\alpha = 20.18^\circ$, the flow undergoes a rapid acceleration along the suction surface of the slat and a small patch of supersonic region is created. This can be prominently distinguished by the presence of a large and slender peak on the

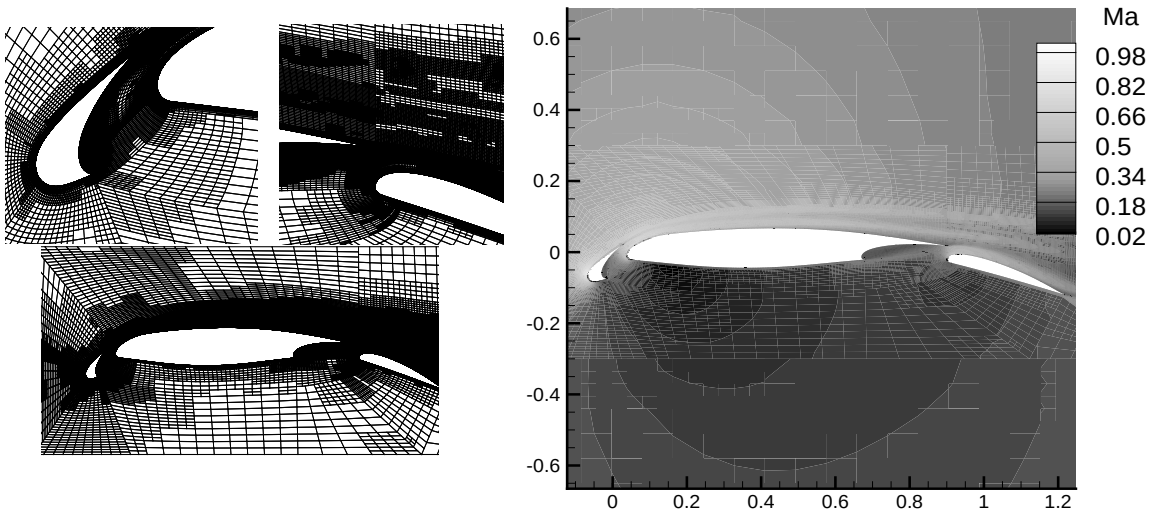

a) Details of adapted final level grid b) Mach number distribution

Figure 39: Adapted grid and flow field over the high-lift configuration at $\alpha = 20.18^\circ$

surface pressure distribution (Fig. 38) at the leading edge. Maximum Mach number of slightly above unit is achieved in the domain.

3.2.2 Accurate capturing of the inception of stall for high-lift configuration

The investigation of the lifting characteristic of the high-lift configuration with varying angle of attack is carried out in this section. The ability of the DES model to accurately predict the stall over the RANS modelling is demonstrated. Computations are performed on an identical initial grid with a set of input parameters as previously described in the section 3.2.1. Simulations are carried out using both S-A RANS models at angles ranging from $0^\circ - 30^\circ$ in steps of 2° with steady Backward Euler time integration scheme. The grid is refined successively during adaptation depending on the developed flow field which is eventually determined by the angle of attack. As expected, the lift coefficient increases linearly (as shown in Fig. 49 a))

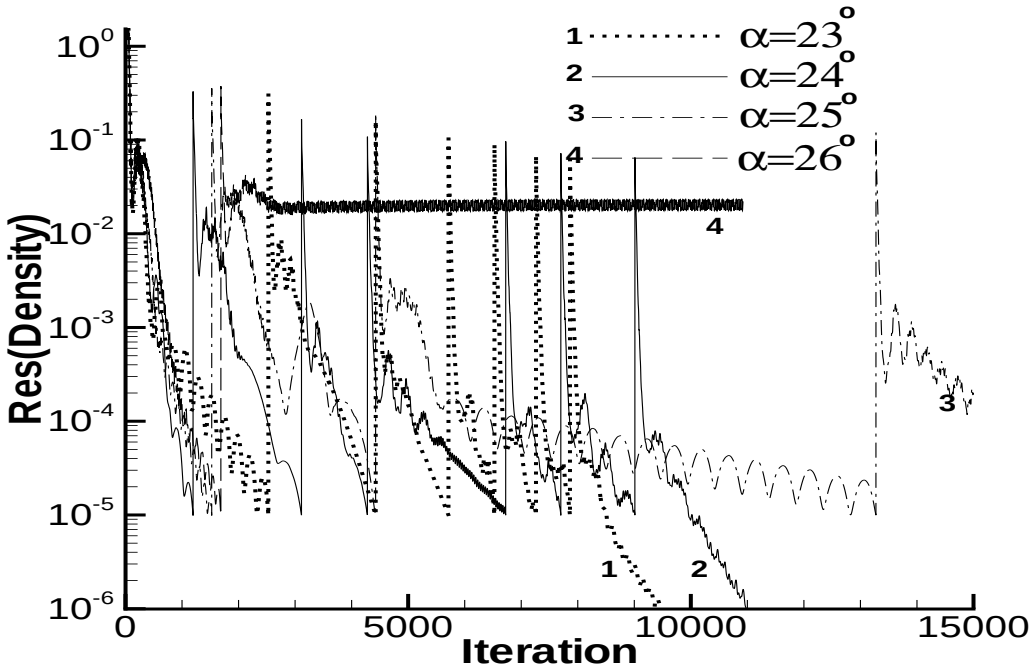

Figure 40: Stall inception angle, computation with the S-A turbulence model using steady time integration scheme in Quadflow

with the increase in the angle of attack till the stall phenomenon is encountered. The computation at this point is characterised by the non-convergence of the residual as shown in the Fig. 41. Numerically converged flow solution is obtained for the input parameter, corresponding to the angles of attack below 25° (see fig. 40). Any subsequent increase in the angle of attack as shown in Figs. 41 a), exhibits an oscillatory behaviour of the residual with no converged solution. The non-convergence of the flow field is also illustrated by the corresponding lift coefficients, which (Fig. 41 b)) fluctuate about a mean value. Similar computations are performed over the configuration with identical set of input parameters and initial grid using turbulence modelling using DES model. The trend of the computational results is similar to the previously

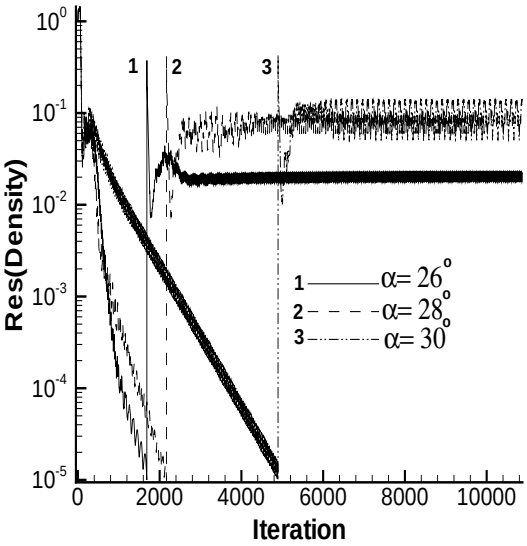

a) Residual history

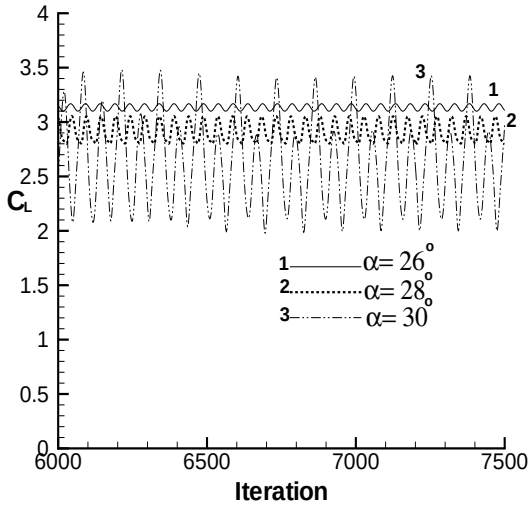

b) Fluctuation of lift coefficient

Figure 41: Numerical prediction of the stalling angle with S–A RANS model
Computations performed with steady time integration scheme

obtained solution using S-A model, but the fluctuation of the residual is encountered earlier at an angle of attack, $\alpha = 23^{\circ}$, as shown in the Fig. 42. Corresponding lift coefficients showed fluctuation about a mean value during non-convergence and converged steady solutions are not achieved. Simulations are carried out with DES modelling in time accurate manner to confirm

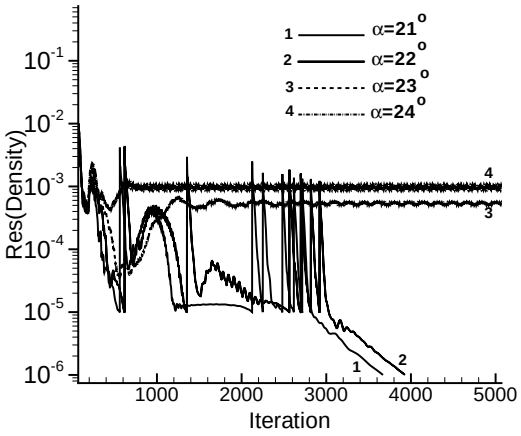

a) Residual history

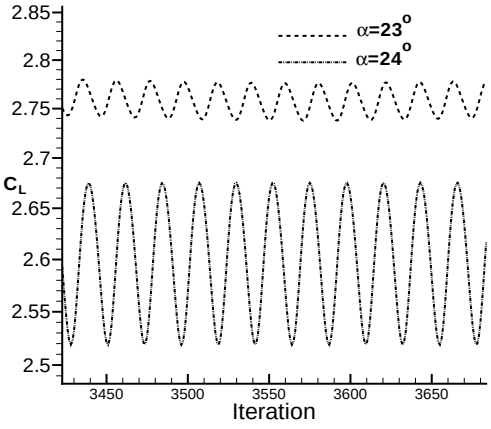

b) Lift coefficient fluctuation

Figure 42: Numerical prediction of the stalling angle with DES model
Computations performed with steady time integration scheme

the unsteadiness, to understand its cause and to resolve unsteady flow features in the domain. Backward difference method described in the numerical modelling section is used as the time integration scheme. The angle of attack for the computation is set to 23°. The criterion for grid

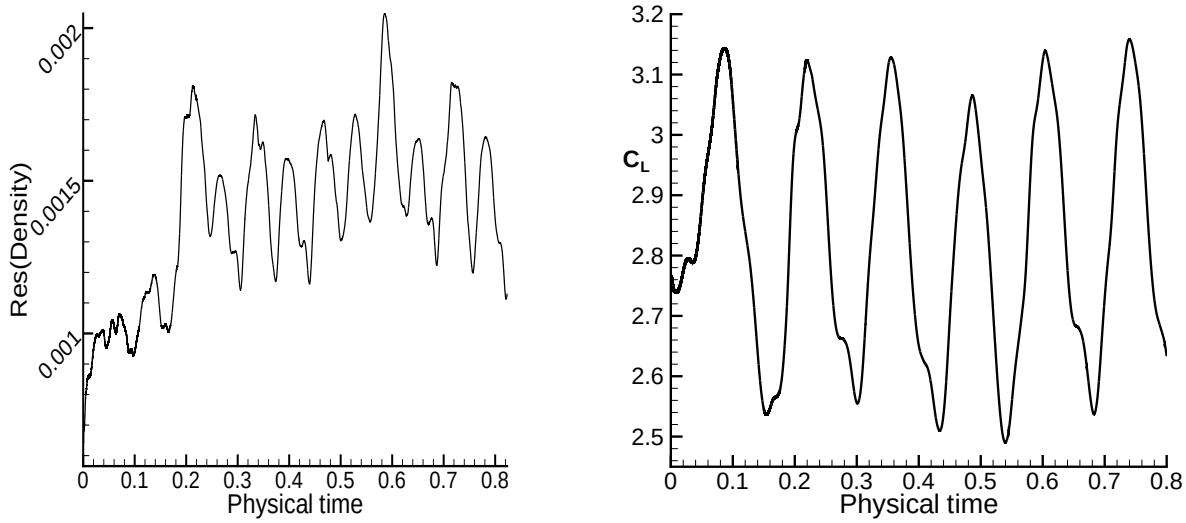

a) Residual history b) Lift coefficient fluctuation

Figure 43: Unsteady flow simulation with DES model at $\alpha = 23^{\circ}$

adaptation is modified to activate the mesh refinement as a function of number of unsteady steps during the time integration process. Figs. 43 a) and b) show the periodic fluctuation of C_L and

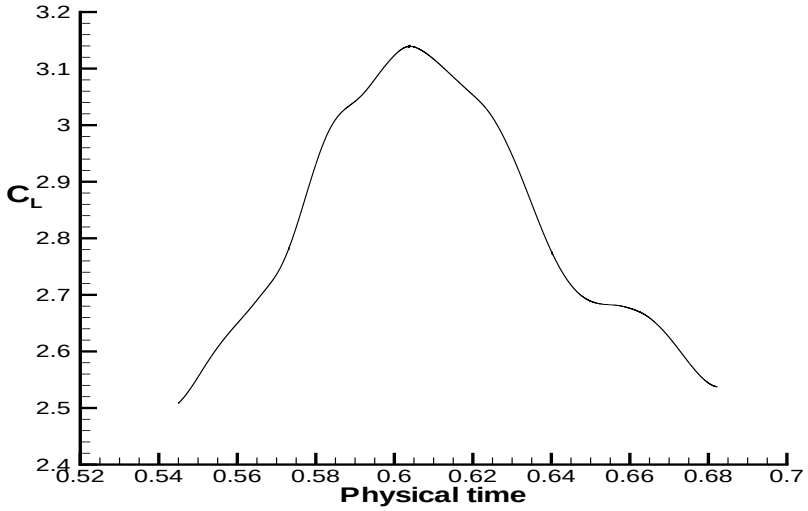

Figure 44: Variation of lift coefficient

the residual at $\alpha = 23^{\circ}$, obtained using unsteady simulation with DES modelling. It is observed that the temporal variation of the lift coefficient after certain initial phase of computation is periodic with a time period of approximately 0.14 seconds. Fig. 44 shows the variation of the lift co-efficient with physical time for a single time period of oscillation, extracted at the final stage of the computation. Figs. 45 a), b), c) and d) show the instantaneous Mach number distributions in the domain at a specific time for $\alpha = 23^{\circ}$ during the single time period of oscillation. The

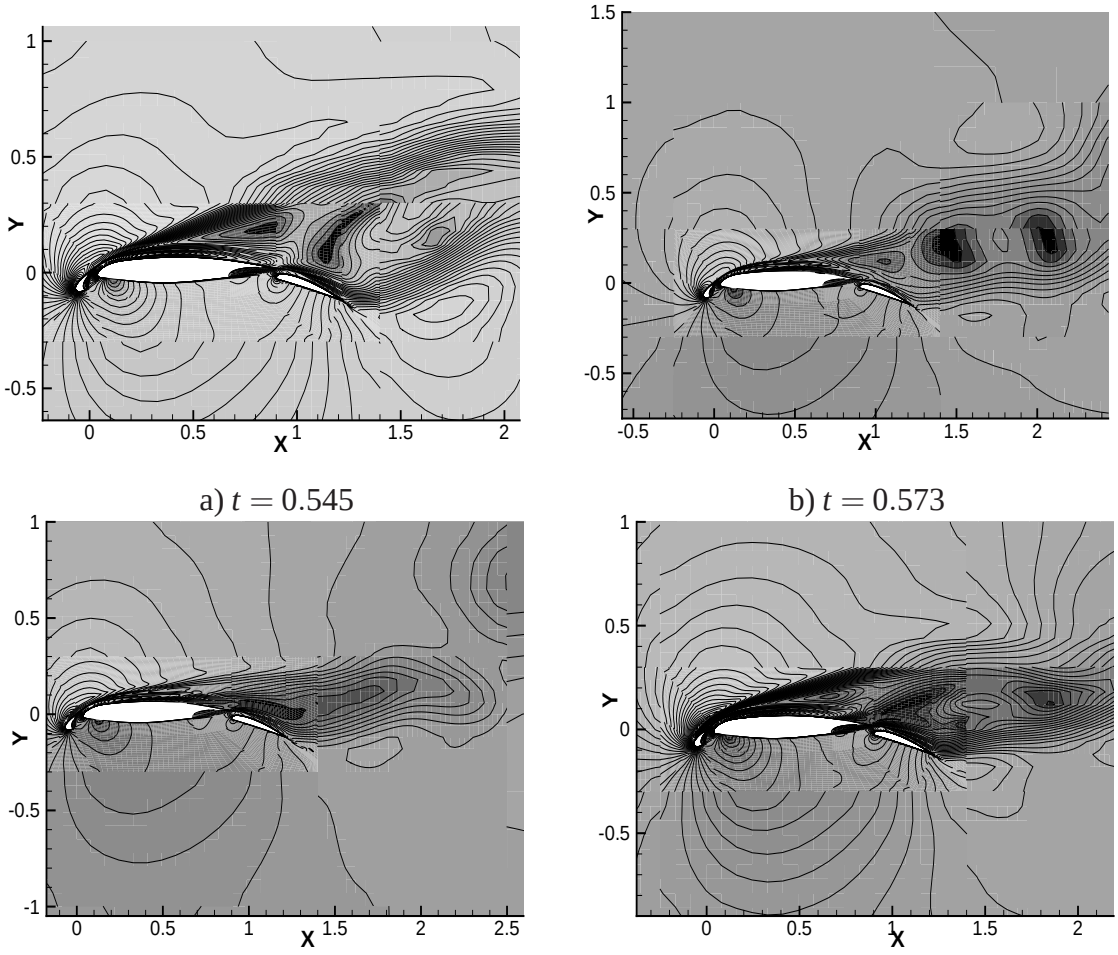

Figure 45: Instantaneous Mach number distribution in the flow field showing vortex shedding captured with DES at $\alpha = 23^{\circ}$

figures show the instantaneous Mach number variation in the flow field as the vortical structures passes through build-up phase, coalition and shedding from the suction surface of the airfoil elements. At $t = 0.545$, the vortices shed from the main element and from the flap in the vicinity of the airfoil are observed to be coming close to each other. The flow field is marked by large scale but partially separated vortices at the suction surfaces of the main element and the flap. The formation of these structures is associated with the loss of lift and is observed by the dip in the value of C_L corresponding to the time $t = 0.545$. When moving further away from the airfoil, these vortices merged together to give rise to a single and dominant vortical structure at $t = 0.573$.

The flow field at time $t = 0.6035$, is characterised by moving of the vortical structures away from the suction surface of the main element, corresponding to the achievement of the maximum lift in the C_L t curve. Flow field at $t = 0.6402$ shows the inception of the vortex near the surfaces of the main element and the flap. The vortices gradually grow during the rest of the time period

until their sizes are large enough to come physically in contact with each other which leads to merging as observed at $t = 0.545$.

The above described sequence of events is repetitive over the time period and the vortices going through the continuous process of formation, merging and shedding give rise to a nearly periodic behaviour to the flow field. At the angle of attack 24°, the flow field exhibits comparatively

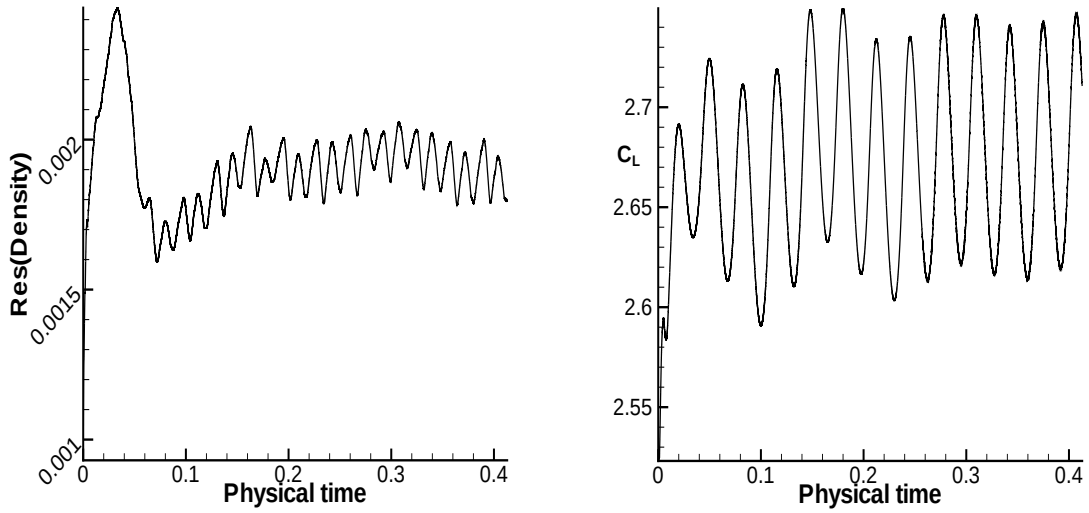

a) Residual history b) Lift coefficient fluctuation

Figure 46: Unsteady flow simulation using DES model at $\alpha = 24^\circ$

larger unsteadiness and a final converged solution is not achieved. The fluctuation of the residual and the lift coefficient are shown in the Fig. 46 The lift coefficient (C_L) goes through a periodic

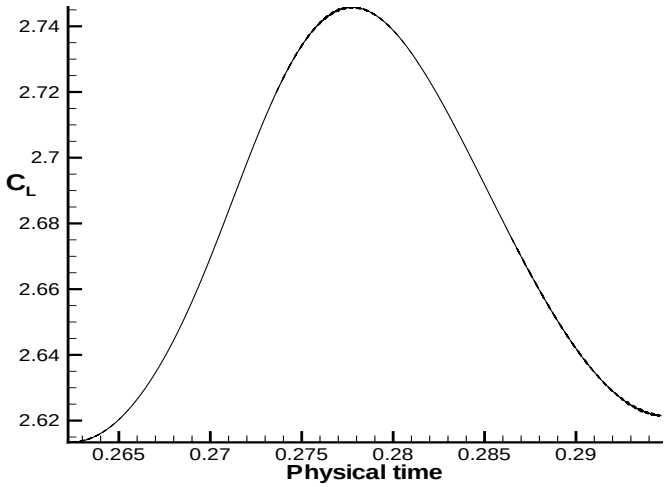

Figure 47: Variation of the fit coefficient during the last cycle using DES model at $\alpha = 24^\circ$

oscillation of time-period $T = 0.03$, corresponding to a frequency of about 33 Hz. Fig. 47

shows fluctuation of the lift coefficient at the final stage of the computation corresponding to the last cycle of oscillation. The flow field occurred at different time is shown by the variation of Mach number in the computational domain in Figs. 48 a) and b). The wake behind the main element and the flap are completely merged together in the vicinity of the solid surface. Vortex shedding is highly conspicuous and the phenomenon is similar to the wake generated behind a bluff body. Lift and drag coefficients are evaluated from the converged solutions obtained

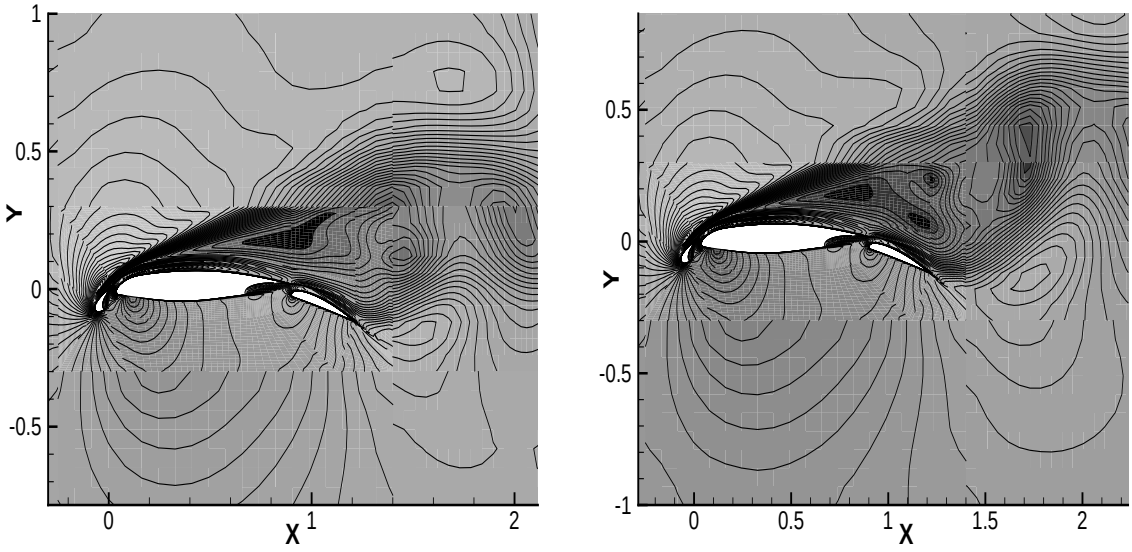

a) $t = 0.26225$ b) $t = 0.27114$

Figure 48: Instantaneous Mach number distribution in the flow field showing vortex shedding captured with DES at $\alpha = 24^{\circ}$

with above mentioned computations for both the DES and S-A RANS modelling. Pre-stall computations in both the modellings yield converged aerodynamic coefficients. Time averaged values of the fluctuating aerodynamic coefficients are used for stall and post-stall conditions.

Figs. 49 a) and b) compare the variation of aerodynamic coefficients at different angles of attack obtained using DES and S-A RANS modelling with the experimental data [71]. The results obtained using S-A RANS and DES modelling have an excellent agreement with the experimental data in the pre-stall region. The stalling angle obtained using S-A RANS model tends to over-predict the experimental data. The solution obtained using the DES computation agrees well. Similar trend of the variation of C_L with α and over-prediction of the stalling angle compared to the experimental data has been observed by other researchers [47] with S-A RANS model on this configuration. Numerically estimated time averaged aerodynamic coefficients obtained using unsteady time-stepping scheme with DES model are close to the experimental data.

The over-prediction in the stall margin using the RANS model is as a result of inaccuracy in modelling the turbulent flow in the regions dominated by large vortical structures associated

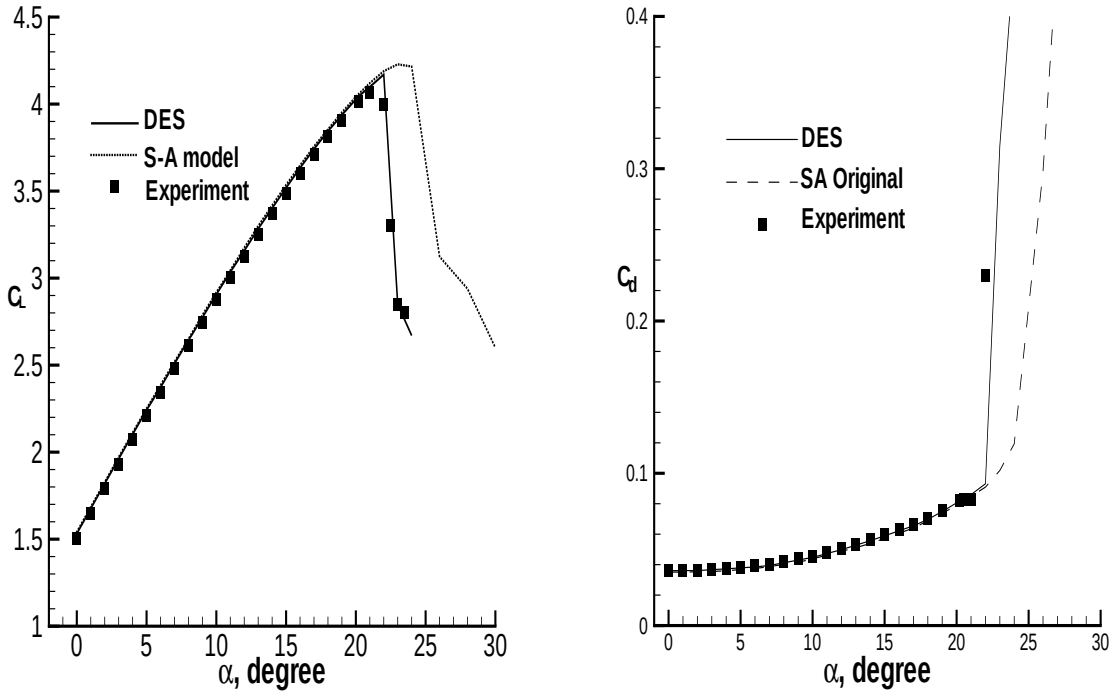

a) Variation of lift coefficient with α

b) Variation of drag coefficient with α

Figure 49: Accurate capturing of stall with DES model in comparison to S–A RANS model

with massive flow separation. The modelling inaccuracy stems from the overestimation of the eddy viscosity, is as a result of the dual inclusion during its explicit modelling from the mean components and partial inclusion of the fluctuating components in the mean flow components through grid resolution. Modification of the wall distance in the DES model according to the grid cell size increases the destruction term of the turbulence modelling to prevent an overestimation of the turbulent viscosity, as explained in the numerical modelling sections (sections 2.3.4 and 2.3.5). The modification is effective in the regions away from the airfoil, where the flow field is dominated by the large scale vortical structures arising due to the large scale separation. Hence, DES model is obviously superior to the original Spalart-Allmaras turbulence model in capturing the separated flow phenomena.

3.3 Low Mach number preconditioning

The section describes the application of the Low Mach number preconditioning technique, as described in the numerical modelling section of the thesis (Section 2.5) on the cruise as well as on the high lift configurations. The application of the method is demonstrated on the inviscid, laminar and turbulent flow regimes. The method is shown to function accurately in domains having predominant low Mach number regions with localised supersonic flow. Testcases with analytically or experimentally available aerodynamic data are chosen to validate the modelling and application of the method. Improvement in the accuracy of the simulated flow field at a relatively lower Mach number is observed. Convergence behaviour is shown to be improving with increase in the low Mach number region in the computational domain.

3.3.1 Inviscid flow simulation

3.3.1.1 Flow over 4% bump Inviscid simulation using preconditioning technique is carried out in the computational domain containing a bump with a maximum thickness, 4% of its length. Free stream Mach number of the flow is set to 0.001. The simulation is carried out without grid

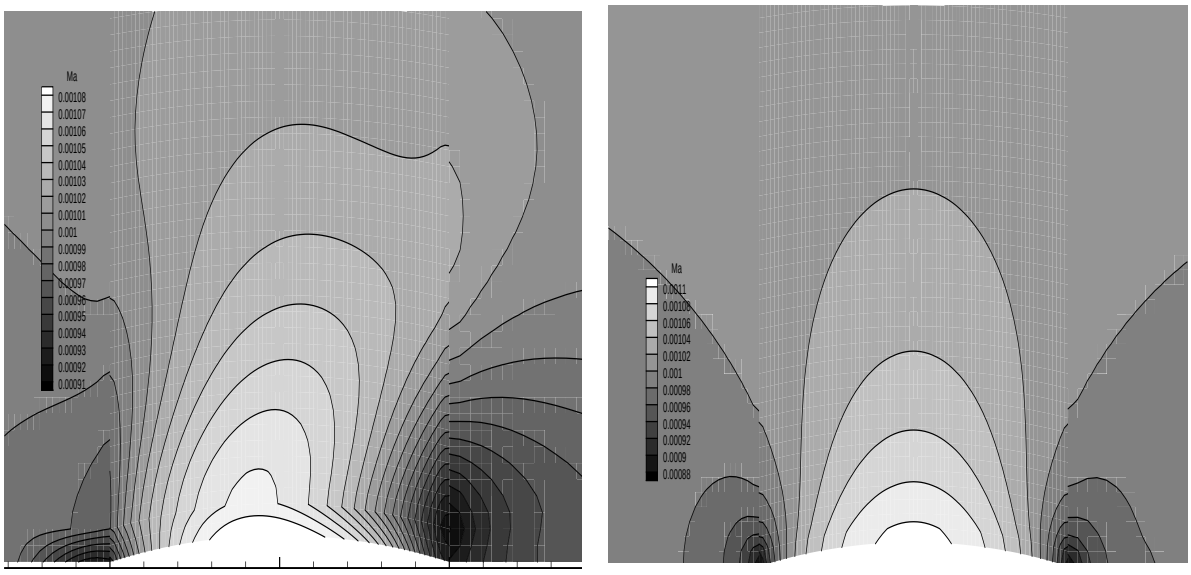

a) Unpreconditioned solution b) Preconditioned solution

Figure 50: Steady flow field with Mach number variation over the bump at $M_\infty = 0.001$

adaptation. The computational domain comprises three blocks with 40 cells along the flow direction and 25 cells along the cross flow direction. Inviscid wall boundary condition with zero normal velocity of the flow is imposed on the bump surface. Extrapolation type boundary condition is applied at the inflow and outflow boundaries. Implicit time integration scheme is used for temporal evolution of the solution. HLLC scheme with modified eigenvalues is used to evaluate the convective fluxes for the preconditioned scheme. Original HLLC scheme is used in the flux computation for the unpreconditioned scheme. The comparison of the Mach number

variation in the computational domain between the solutions obtained using unpreconditioned and preconditioned formulations is shown in the Fig. 50.
The convergence is achieved faster with the use of preconditioner compared to the unpreconditioned scheme. It is observed that the preconditioning improves the smoothness of the solution. The resulting Mach number variation in the computational domain is observed to be symmetric over the bump. In contrast, the solution obtained without preconditioning is observed to be associated with glitches in the Mach number contour plot in the domain. The pressure recovery associated with low Mach number flow forces a symmetric solution over the bump configuration, which is accurately captured using the preconditioned computation.

3.3.1.2 Flow over NACA0012 profile Flow is simulated over NACA0012 profile at freestream Mach numbers 0.001 and 0.01, with angle of attack 2°. Eight levels of grid adaptation is conducted to obtain a converged final flow solution. The multiscale control parameter for the grid adaptation has been set to a lower value, as the spatial variation of the flow solution is relatively smaller in magnitude. Number of iterations required to achieve corresponding

Adap	Timestep	Cell number	C_L	C_d
1	37	400	0.206865	0.0334168
3	125	6352	0.23376	0.00195
5	236	26368	0.24083	0.000082
7	340	36514	0.241049	0.000037
9	572	39076	0.241040	0.000033

Table 7: Inviscid flow simulation over NACA0012 profile with preconditioning, $M_\infty = 0.001, \alpha = 2^\circ$

levels of grid adaptation, number of cells in the computational domain and the aerodynamic coefficients are given in the table 7 and table 8.

Adap	Timestep	Cell number	C_L	C_d
1	35	400	0.205542	0.033456
3	116	6400	0.222238	0.003940
5	219	44332	0.238695	0.000202
7	336	84274	0.241133	$2.17E10^{-6}$
9	431	94960	0.241266	$-1.5E10^{-8}$

Table 8: Inviscid flow simulation over NACA0012 profile with preconditioning, $M_\infty = 0.01, \alpha = 2^\circ$

The converged lift coefficients obtained from the computation is observed to be independent of the Mach number. The drag coefficient decreases with each grid adaptation till a value close to

zero is obtained. The computational results satisfy the D'Alembert's paradox. Comparison of

C_L	C_d
0.241	0.0

Table 9: Aerodynamic coefficients over NACA0012 profile, panel method (Turkel)

the aerodynamic coefficients are in excellent agreement with the computational results obtained by Turkel (Table 9).

3.3.1.3 Flow over SFB profile Similar computations are performed on the SFB profile with eight levels of grid adaptation. The free stream Mach numbers of the flow are set to 0.001 and 0.01. The aerodynamic coefficients achieved at the intermediate grid levels, variation in the

Adap	Timestep	Cell	C_L	C_d
1	35	400	0.18972	0.02401
4	165	16948	0.237111	0.001009
7	332	74794	0.235498	$-4.9E10^{-6}$
9	448	91339	0.235381	$-4.9E10^{-6}$

Table 10: Preconditioned simulation over SFB profile, $M_\infty = 0.001, \alpha = 0^\circ$

number of cells in the computational domain and the required timestep to achieve the convergence level for both the cases are tabulated in Table 10 and Table 11. The trend of the solutions obtained in the computations is similar to the previous computation over NACA0012 profile. The aerodynamic coefficients are observed to be independent of the free stream Mach number. The drag coefficient is observed to be approaching to zero. The flow field at low Mach number is characterised by the pressure recovery. The pressure drag for a blunt body of any shape is zero as a result of the pressure recovery. The viscous drag attributed to the skin friction on the surface is numerically absent as a result of inviscid flow modelling. Thus, a zero drag is achieved satisfying D'Alembert's paradox. The Mach number independent lift coefficient is converged to

Adap	Timestep	Cell	C_L	C_d
1	35	400	0.189753	0.024048
4	164	22180	0.237133	0.0010183
7	331	150559	0.235532	$-6.7E10^{-6}$
8	388	148318	0.235537	$-6.9E10^{-6}$

Table 11: Preconditioned simulation over SFB profile, $M_\infty = 0.01, \alpha = 0^\circ$

0.235 and the drag coefficient becomes negligibly small in the converged solution at the finest grid level. It is worth pointing out that the drag coefficient predicted by the computation at

C_L	C_d
0.235	$1.0E10^{-6}$

Table 12: Mach number independent aerodynamic coefficients

the initial level of grid with 400 cells is 0.02. The improved resolution of the computational domain through grid adaptation causes the downward shift of the drag coefficient, reaching the value close to zero at the finest level. The adaptation criterion based on the multiscale analysis is proved to be efficiently functioning in the presence of low Mach number flow field.

3.3.2 Laminar flow simulation

Numerical validation and computational efficiency of the preconditioning technique in the laminar flow region is illustrated in this subsection. Flow is simulated over NACA0012 profile at

Adap	Timestep	Cell	C_L	C_f	C_d
1	57	400	0.09398	0.011962	0.10715
3	252	3151	0.047207	0.042036	0.06712
5	517	11407	0.047126	0.047846	0.07188
7	1084	13231	0.047478	0.049467	0.07355

Table 13: Laminar flow simulation over NACA0012 profile with preconditioning, $M_\infty = 0.001, \alpha = 1^\circ, Re = 2500$

the Reynolds number of 2500 and 1° angle of attack. Two freestream Mach numbers, 0.001 and 0.01 are chosen for the computations. The initial level grid, discretising the computational domain is coarse and contains 600 cells. Extrapolation type boundary condition is imposed at the inflow and outflow boundaries. No-slip, adiabatic boundary condition is imposed on the cells on the airfoil surface.

Adap	Timestep	Cell	C_L	C_f	C_d
1	53	400	0.09398	0.011962	0.10715
3	183	3151	0.04715	0.042036	0.06712
5	315	11419	0.04708	0.0478423	0.07188
7	459	13231	0.04747	0.049467	0.073549

Table 14: Laminar flow simulation over NACA0012 profile with preconditioning, $M_\infty = 0.01, \alpha = 1^\circ, Re = 2500$

The CFL number of the computation is geometrically increased with a factor of 1.05 from an initial value set to 0.8, till the maximum value of 500 is reached in the domain. Preconditioned HLLC scheme, described in the numerical modelling section is used to compute the convective

fluxes. Six levels of grid adaptation is carried out to obtain the final converged flow solution. The boundary layer is the most active region in the computational domain owing to a small freestream Mach number. The cells in the boundary layer are observed to be refined with successive level of grid adaptation and the flow features are adequately resolved at the finest grid level.

The tables 13, 14 show the number of iterations required to achieve the intermediate levels of grid adaptation, number of cells in the computational domain and the resulted aerodynamic coefficients achieved during the computations.

C_L	C_d
0.0474	0.0734

Table 15: Mach number independent aerodynamic coefficients

The aerodynamic coefficients are observed to be independent of free stream Mach number. Comparison of the integral surface parameters predicted by Quadflow with the numerically obtained solution by Turkel [59] (table 15) show an excellent agreement.

3.3.3 Turbulent flow simulation

Computation is performed over RAE2822 profile at the freestream Mach number, $M_\infty = 0.01$, angle of attack, $\alpha = 1.89^\circ$ and Reynolds number, $Re = 5.7 \times 10^6$. Spalart-Allmaras turbulence model is used in the computation. The initial grid has 400 cells and the final solution is obtained

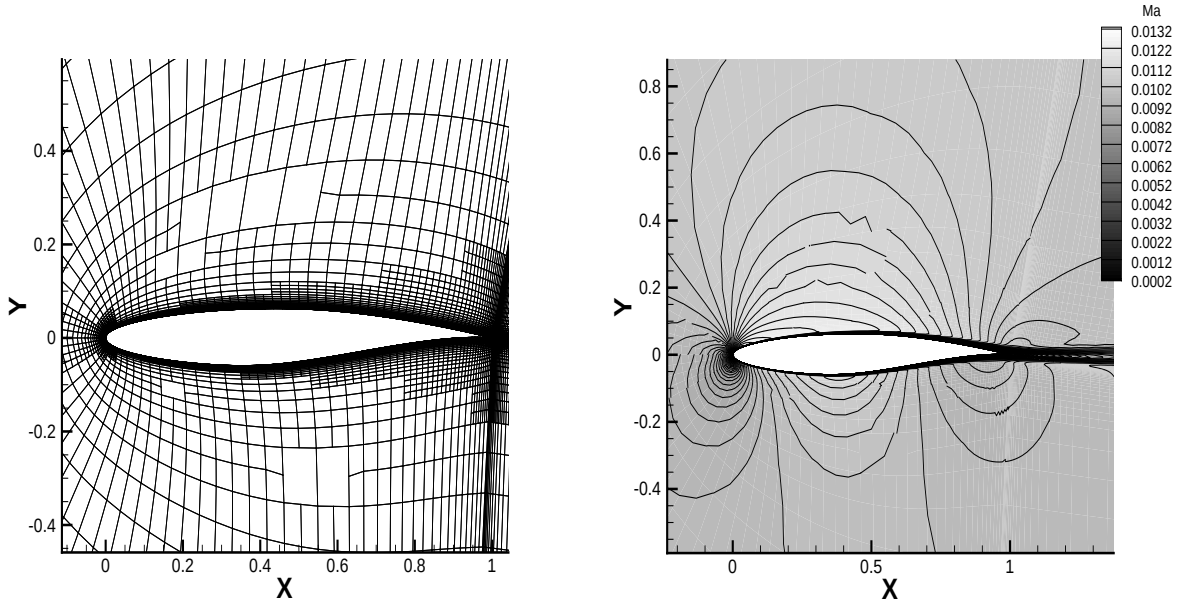

a) Final level adapted grid b) Mach number variation in the domain

Figure 51: Adapted grid and turbulent flow solution over RAE2822 at $M_\infty = 0.01$

after three levels of grid adaptation with the computational domain comprising of 14899 cells.

Surface distribution of y^+ below unit is achieved in the finest grid level.

Fig. 51 shows the final level adapted grid and corresponding Mach number variation in the computational domain. As expected, relatively low value of free stream Mach number restricts the grid adaptation within the boundary layer. No significant addition of number of cells outside the boundary layer is observed. The refinement of the cells in the boundary layer resulted in achieving a surface distribution of $y+$ below unit.

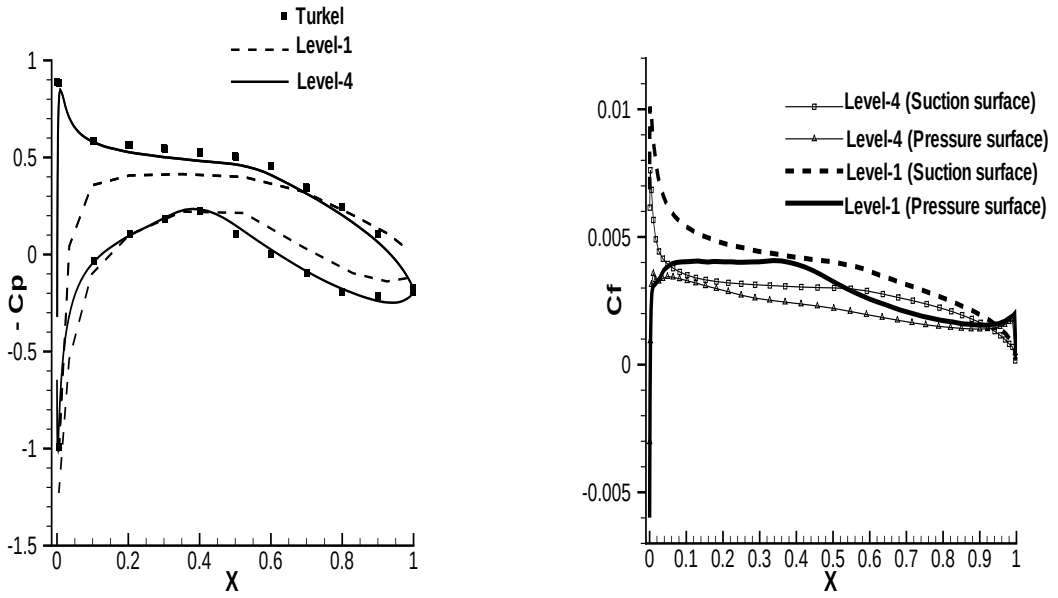

a) Surface pressure distribution b) Surface skin friction distribution

Figure 52: Gradual evolution of the surface flow coefficients with grid adaptation

Fig. 52 shows a gradual improvement in the static pressure and skin friction distribution on the profile with every successive level of grid adaptation. The static surface distribution on the final level grid is plotted and compared with the computationally predicted data by Turkel [59].

The flow in the current simulation is assumed to be fully turbulent, whereas in the computation performed by Turkel the flow is tripped to be turbulent after traversing 11% of the chord length from the leading edge. The transition is considered to be profoundly affecting the estimation of surface skin friction coefficient. Hence, the result from the current simulation is not compared with the variation of wall skin friction coefficient data predicted by Turkel.

3.3.4 Simulation over the high-lift configuration with low Mach number preconditioning

Relatively low freestream flow speed creates a predominant low Mach number region in the computational domain of the high lift configuration. Hence, the preconditioning technique is used to accelerate the convergence speed of the simulation. Flow computations are performed at freestream Mach number, $M_\infty = 0.197$,, angle of attack, $\alpha = 0.0^\circ$, and the Reynolds number based on the chord length, $Re = 3.52 Miliion$. Identical initial grid and set of input parameters

are used in both the simulations with six levels of grid adaptation. Flux is computed using HLLC [62] scheme for the unpreconditioned method. Modified HLLC scheme is used for flux computation during the preconditioned simulation. Cut off parameter (K) is chosen to be 0.80.

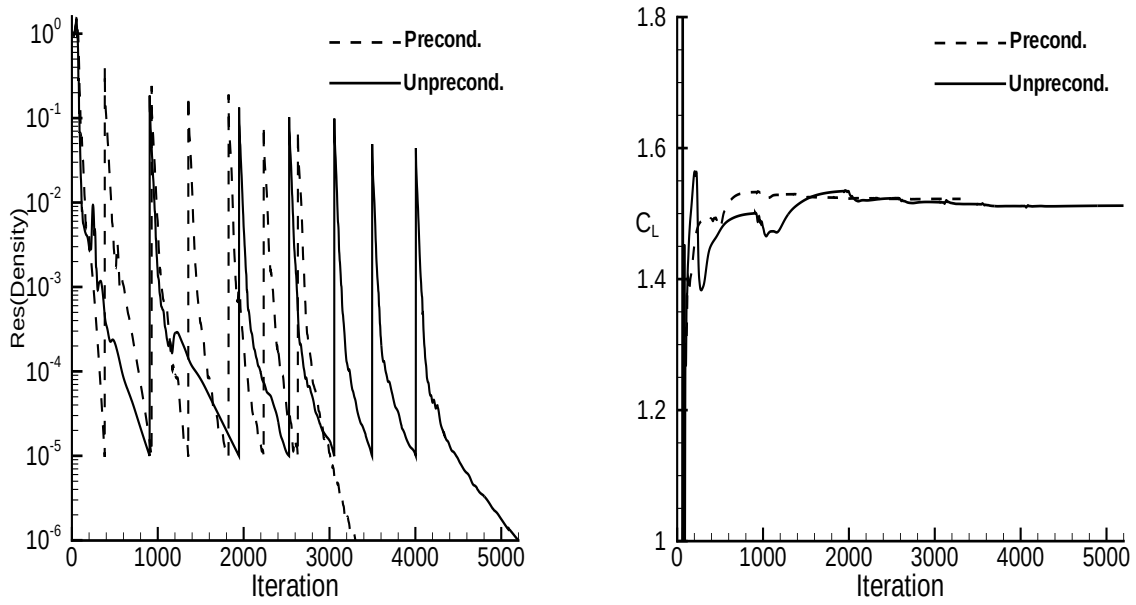

a) Residual history b) Evolution of lift coefficient

Figure 53: Convergence acceleration with preconditioning at $\alpha = 0^\circ$

Fig. 53 compares the convergence behaviour and the solutions obtained using a preconditioned scheme with the result from an unpreconditioned computation. The preconditioned computation is observed to be converging 1.7 times faster compared to the unpreconditioned method. The lift coefficient is rapidly converged to the desired value with the use of preconditioner in comparison to the unpreconditioned simulation.

Similar comparative study between the preconditioned and unpreconditioned schemes has been carried out on the high-lift configuration at the angle of attack, $\alpha = 20^\circ$. The fluid stream at the high angle of attack undergoes a rapid acceleration over the suction surface of the slat and creates a small localised supersonic zone. It is interesting to use and assess the benefit of the preconditioning technique which is effectively designed for the low Mach number regions in a computation with the flow achieving supersonic speed. The Cut off parameter (K) is chosen to be 0.80.

Fig. 54 compares the convergence behaviour and the variation of the lift coefficients with iterations obtained using the preconditioned scheme with an unpreconditioned simulation. In the presence of preconditioner, the convergence is shown to be 1.6 times faster than the unpreconditioned scheme. It is important to note, the factor of improvement in convergence obtained at a lower angle of attack is higher compared to the higher angle of attack. The reasons being; i) the preconditioner stays effective in larger regions of the computational domain for the config-

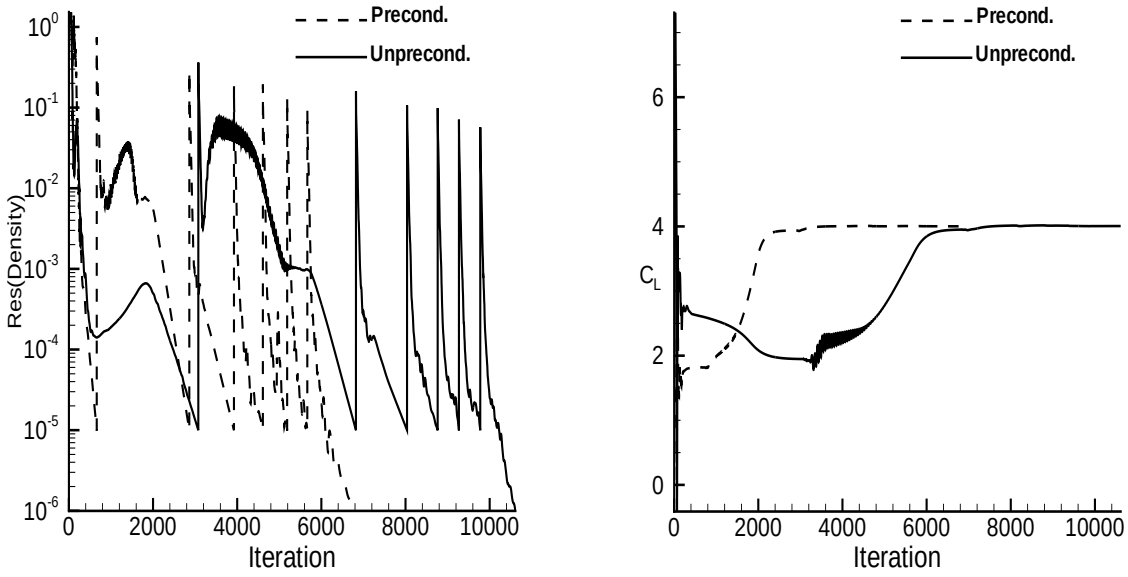

a) Residual history b) Evolution of the lift coefficient

Figure 54: Convergence acceleration with preconditioning at $\alpha = 20^\circ$

uration having lower angle of attack, ii) the presence of relatively low Mach number at $\alpha = 0.0$, providing an improved modification of the condition number compared to the higher angle of attack.

Maximum Mach number achieved in the computational domain with $\alpha = 0.0^\circ$ is 0.46, compared to the maximum Mach number of 1.02 achieved with $\alpha = 20.0^\circ$.

3.3.5 Effect of cut-off Mach number on convergence and solution accuracy

The preconditioning matrix, used to modify the eigenvalues of the Jacobian matrix depends on the preconditioning parameter, which is a function of the Reference Mach number (M_{ref}). The local nature of the preconditioner depends on M_{ref}, which varies with the local normal Mach number in the computational domain. Local Mach number in the stagnation region of the computational domain becomes insignificantly small. Hence, in order to prevent the M_{ref} to become too small, a cutoff limit based on the freestream Mach number M_∞ and a cut-off parameter (K) is prescribed. The effect of the cutoff parameter (K) on the solution field and the convergence is studied in this section. The range of the cutoff parameter lies between zero and unit. Two preconditioned simulations are carried out at $M_\infty = 0.197, \alpha = +0.0^\circ, Re = 3.52$Million over the high-lift configuration with 6 levels of grid adaptation using two different cut-off values ($K = 0.75, K = 0.80$). Similar computations are performed at $\alpha = +20.0^\circ$. Comparison of the convergence behaviour and the aerodynamic coefficients obtained from the computations are shown in the Fig. 55. Table 16 compares the converged aerodynamic coefficients at the final grid level from the computations with two different cutoff parameters. No significant differ-

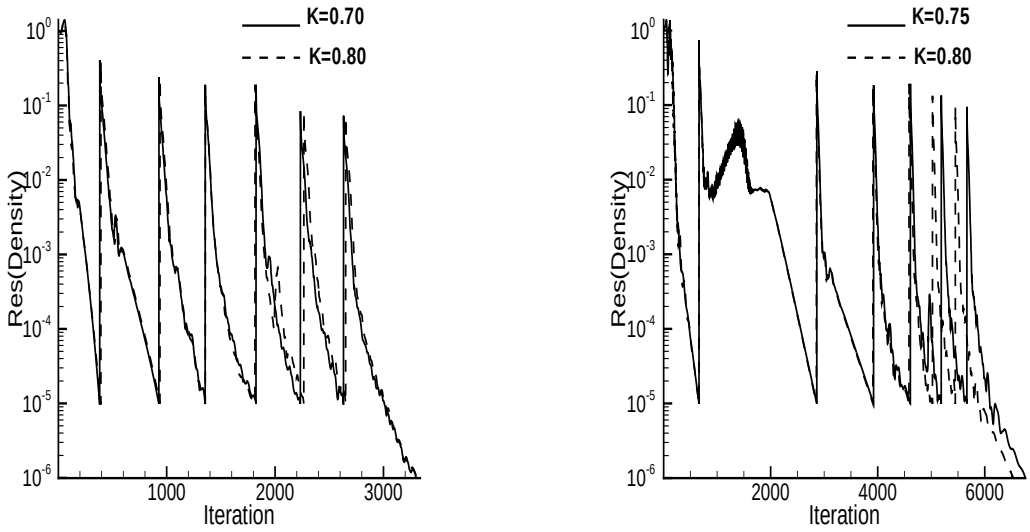

a) $\alpha = 0.0^\circ$ b) $\alpha = 20.0^\circ$

Figure 55: Dependency of the convergence behaviour on the cut-off parameter used in low Mach number preconditioning

Cutoff	C_L	C_d
0.70	1.522423e+00	3.216249e-02
0.80	1.522665e+00	3.217980e-02

Table 16: Dependency of the aerodynamic coefficients on the cut-off parameter, $\alpha = +0.0^\circ$

ence either in the convergence pattern or in the magnitude of the aerodynamic coefficients is observed due to the choice of cut-off parameter. At $\alpha = +20.0^\circ$, the cut-off parameter plays a role owing to the presence of small patch of supersonic region on the upper surface of the slat. Slight increase in the value improves the robustness and accelerates convergence. Flow field remains unaffected by the choice of the cutoff parameter as shown by the comparison of aerodynamic coefficients in the table 17.

Cutoff	C_L	C_d
0.75	4.001844e+00	7.138033e-02
0.80	4.002207e+00	7.139914e-02

Table 17: Dependency of the aerodynamic coefficients on the cut-off parameter, $\alpha = +20.0^\circ$

3.3.6 Detached Eddy Simulation over high-lift configuration with low Mach number preconditioning

Numerical experiments are conducted to asses the convergence efficiency and solution accuracy of the DES in presence of low Mach preconditioner for simulating flow over the high lift configuration. Four different numerical models, i.e. S-A original model, S-A model with preconditioning, Detached Eddy Simulation and DES with preconditioning are used for computations using identical initial grid and set of input parameters. The flow condition is set to $M_\infty = 0.197, \alpha = +0.0^\circ, Re = 3.52$Million. 6 levels of grid adaptation is carried out as shown in the Fig. 56.

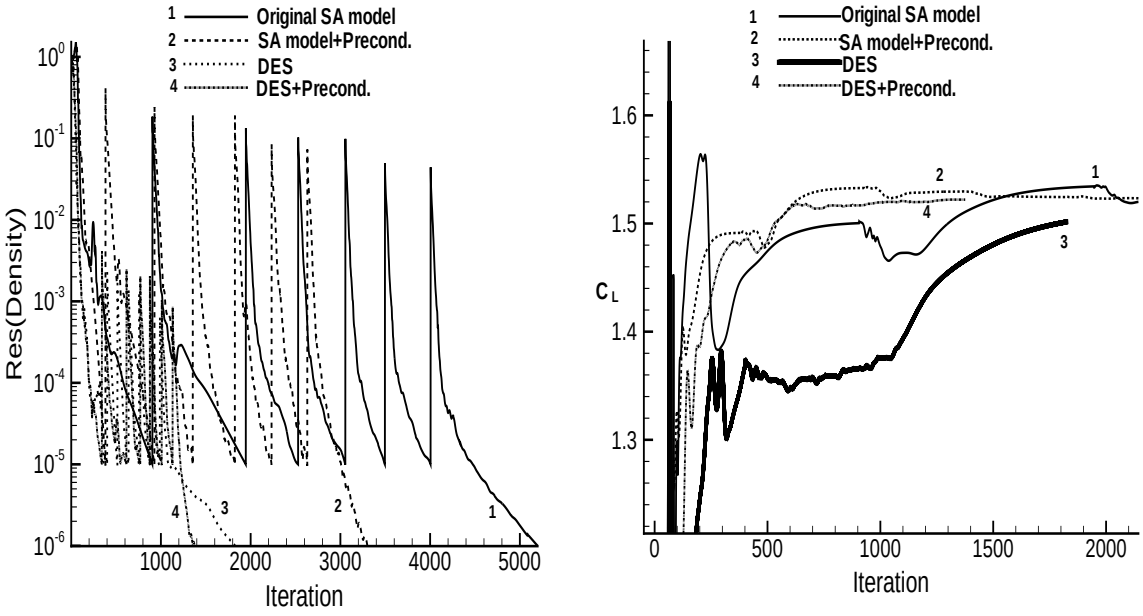

a) Comparison of residual fall b) Evolution of lift coefficient

Figure 56: Convergence acceleration using DES model with preconditioning at $\alpha = 0^\circ$

Figure 56 b) shows the evolution of the lift coefficient (C_L) with iteration obtained during computations.

Model	Itn	C_L	C_d
SA original	5198	1.512109e+00	3.523598e-02
SA+Precond.	3301	1.522423e+00	3.216249e-02
DES	1827	1.501575e+00	3.597372e-02
DES+Precond.	1376	1.522106e+00	3.208049e-02

Table 18: Comparison of aerodynamic coefficients obtained using different computational models

The data in the table 18 shows the number of iterations required to reach the intermediate level of grid adaptation and corresponding aerodynamic coefficients achieved with the use of differ-

ent computational models. The combination of DES with preconditioning is observed to be approximately 4 times faster than the original S-A RANS formulation. The drag coefficients at the final level grid predicted by the preconditioned computations differs by approximately 10% compared to the unpreconditioned simulation. The difference in the solutions is because of the modification of the flux formulation in the low Mach number regions where the preconditioning is activated. The flux formulation is modified to a lower level of numerical dissipation in the regions to improve the solution accuracy.

3.4 Unsteady computations in the presence of grid movement

Inviscid numerical computations on a standard testcase of sinusoidally pitching NACA0012 airfoil about its quarter chord point are carried out with grid adaptation to validate and assess the computational efficiency of the Backward Difference Scheme. The numerical formulation of the scheme and its satisfaction of the geometric conservation law, essential for the moving grid applications are described in the numerical modelling section 2.4.

The temporal variation of the aerodynamic coefficients obtained by the BDF scheme are compared with the available experimental data [86]. The robustness of the scheme is compared with the previously available unsteady time integration scheme (Mid-point scheme) [25].

The pitching motion of the airfoil is described by Eqns. (59). The mean angle of attack and the amplitude of oscillation are set to 0.016° and 2.51° respectively. Reduced frequency of the computation, $\kappa = \omega c/|V_\infty| = 0.1628$. The freestream Mach number and the static temperature of the fluid are 0.755 and 285K respectively. Considering the above set of flow parameters, the time-period of oscillation becomes 0.151 sec for the airfoil of unit chord length.

Initially, the computation is performed using steady time integration scheme to obtain a converged solution to be used as a restart flow field for the unsteady simulation. The use of the converged flow field at the beginning of the unsteady computation helps in reducing the initial instability and allows utilising relatively larger global timestep. The initial C-grid has 400 cells in the computational domain. Characteristic boundary conditions described in the numerical modelling section is imposed at the boundaries interfacing with the freestream. Inviscid slip wall boundary condition is imposed on the airfoil surface.

The movement of the airfoil surface boundary during the oscillation and corresponding spatial relocation of the internal nodes in the computational domain is explained in [7].

$$\alpha = \alpha_0 + \alpha_m sin(\omega t)$$

$$\alpha_0 = 0.016^\circ, \alpha_m = 2.51^\circ \tag{59}$$

The solution is evolved identically in the entire computational domain, through the global timestep, set as an input parameter. The grid adaptation is carried out after every timestep. Several Newton iterations are carried out in a single timestep till the non-linear equation arisen during the discretisation process has converged to the order of 10^{-4}. The system of linear equation inside each Newton step is solved with preconditioned restarted GMRES method. Incomplete Lower Upper (ILU(2)) preconditioner computed from an analytically derived Jacobian matrix is used.

Number of steps required to complete the cycle of oscillation varies depending on the global timestep.

3.4.1 Study of accuracy of the scheme

The number of grid adaptation level is set to five. The flow field in the domain is advanced at 1.5×10^{-4} second during each step. The maximum CFL number achieved in the domain is approximately 395.

Scheme	Adaptation level	Timestep	Max CFL
BDF	5	1.5×10^{-4}	395

Computational parameters

The movement of the airfoil, as a rigid body undergoes a rapid variation of velocity and acceleration during the pitching motion. The angular displacement of the airfoil modifies the angle of attack with relative to the free stream flow. The flow field around the rigid body is observed

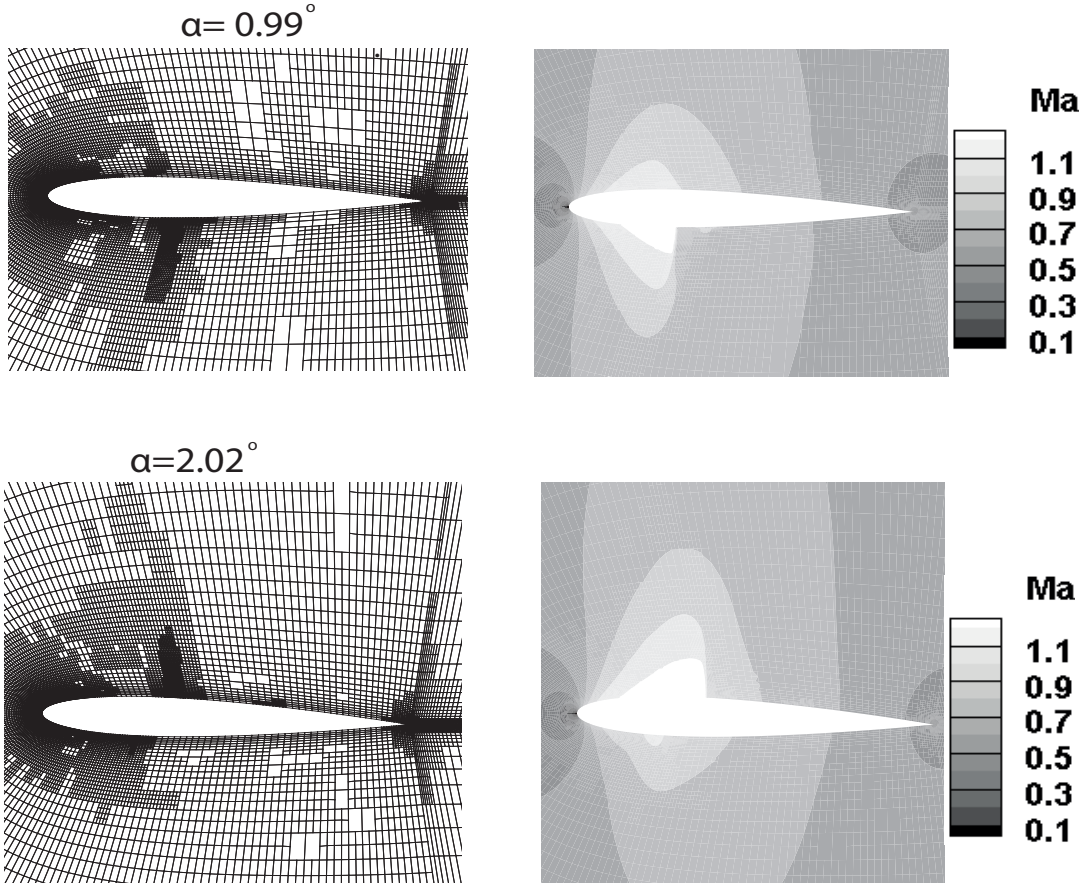

Figure 57: Adapted grid and Mach number distribution in the computational domain during nose-up movement

to undergo significant modification due to the kinematics [50] which is reflected in the variation of the shock location in the domain, as shown in the Fig. 57 and Fig. 58. Fig. 57 shows the instantaneous adapted grids and Mach number distribution in the computational domain during

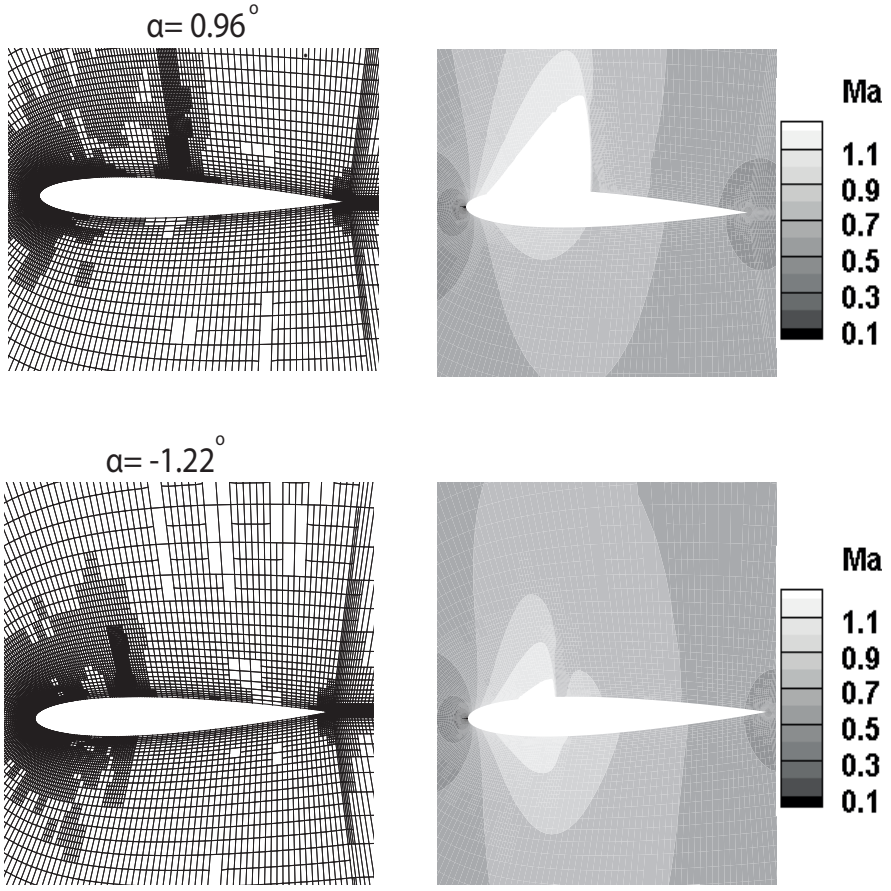

Figure 58: Adapted grid and Mach number distribution in the computational domain during nose-down movement

pitching up movement phase of the oscillation at the angle of attack 0.99° and 2.02°. A mild shock is observed on the pressure surface of the profile at $\alpha = 0.99°$. The strength of the shock is gradually reduced during nose-up movement. The process culminates in the disappearance of the shock on the lower surface and development of a week shock on the suction surface at the peak angle of attack.

Fig. 58 shows the adapted grids and Mach number distribution in the computational domain during pitching down phase of the oscillation. During downstroke the shock on the upper surface of the profile is gradually increased in strength to reach the maximum. Then its strength undergoes a gradual reduction and a shock on the lower surface starts developing.

The fluctuation of the shock between suction and pressure surfaces of the profile creates the topological variation in grid clustering through adaptation as shown in the Figs. 57 and Fig. 58.

Figs. 59 a) and b) shows the variation in the number of cells in the domain with physical time due to grid adaptation. The periodic pattern of fluctuation in the number demonstrates the periodicity of the solution.

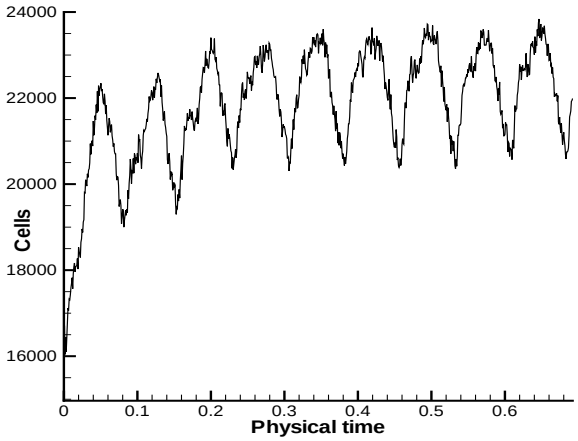

Figure 59: Periodic variation of cell number in the computational domain

The pitching motion results in the temporal variation of the vorticity of the flow around the airfoil. Hence, the aerodynamic coefficients undergoes a periodic change with time as shown in the Fig. 60. The flow solution attends a periodic steady state after experiencing the transience through the initial three quarter of the time period.

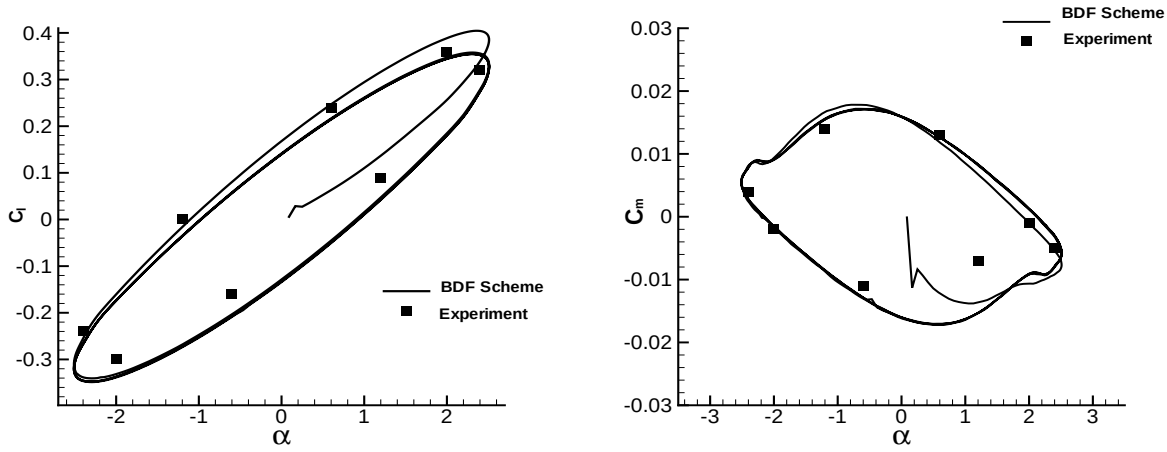

a) Lift coefficient hysteresis b) Moment coefficient hysteresis

Figure 60: Accuracy of Implicit BDF scheme for sinusoidally pitching NACA0012 airfoil

It is observed that the flow pattern experienced by the airfoil at the mean position depends on the orientation of the airfoil movement. This change in the flow field is observed in the difference of the aerodynamic coefficients, which take the form of hysteresis curves. The velocity of the rigid body plays a significant role in determining the surrounding flow structure, even though the flow incidence angle remains identical. At the extreme end positions of the motion, the velocity becomes zero and the flow field is governed by the angles of attack.

The plotted lift and moment hysteresis curves are compared with the experimental data [86].

3.4.2 Comparison with the midpoint scheme

The computational parameters, e.g. levels of grid adaptation, global timestep used in the simulation and the corresponding maximum CFL number achieved in the domain are shown in the Table 19. Three sets of computations are performed with different number of grid adaptation and global timesteps. Increasing the number of adaptation level decreases the smallest size of the cell in the computational domain. Thus, the maximum CFL number in the domain is in-

Scheme	Adaptation level	Timestep	Max CFL
BDF & midpoint	4	2.0×10^{-4}	230
BDF & midpoint	4	5.0×10^{-4}	560
BDF & midpoint	5	2.0×10^{-4}	500

Table 19: Cases simulated for assessing robustness of the numerical scheme

creased by an approximate factor of two with every successive level of adaptation. Increase in the global timestep acts as a scaling factor in increasing the CFL number. Computations are per-

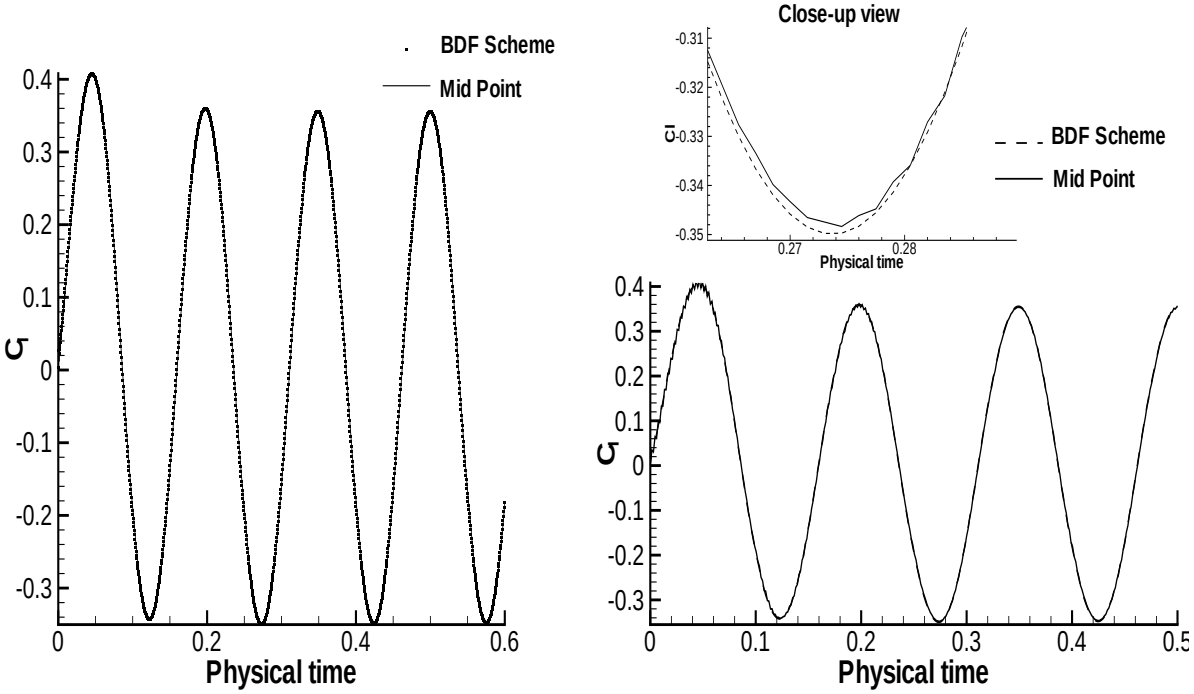

a) Global timestep $2x10^{-4}$ b) Global timestep $5x10^{-4}$

Figure 61: Comparison of the effect of timestep on convergence for the schemes with a 4 level adapted grid

formed using the currently implemented backward difference scheme and with the pre-existing Mid-point scheme for comparison.

Simulations carried out with 4 levels of grid refinement and the global timestep of 2×10^{-4}, are used as the base for assessing the solution accuracy of the recent scheme with respect to

the pre-existing method. Maximum CFL number achieved in the domain is approximately 230. Fig. 61 a) compares the temporal variation of the lift coefficient using the above mentioned schemes. Excellent aggrement in the form of superimposition of the curves verifies the validity of the recently implemented BDF scheme. In the next computation, the global timestep is increased keeping the grid refinement level fixed. The Mid-point scheme is diverged at the global timestep of 6×10^{-4} in comparison to the backward difference scheme, which is observed to be functional with the same set of input parameters. Hence, a global timestep of 5×10^{-4} is chosen for both the schemes in order to draw comparison between the solutions. A maximum CFL number of approximately 560 is achieved in the domain. Fig. 61 b) compares the variation of the lift coefficients with the physical time obtained from both the computational models. The solution from either of the schemes is periodic in time and matches to a certain degree of tolerance. The solution from the model using the Mid-point scheme has appeared to be oscillatory in nature with wriggles in the initial phase of the computation. The duration of computational time required for the simulation to pass through the initial transience in order to achieve the periodic steady state of the solution is larger for the Mid-point scheme compared to the BDF method. The stability of the BDF scheme is demonstrated in the comparison of the lift coefficient curves between the schemes at close-up view in the trough. The solution obtained using the Mid-point scheme exhibits the presence of conspicuous wriggles compared to the smoothness in the solution with BDF. The improvement in the numerical stability of the time integration scheme in Quadflow with the use of recently implemented BDF scheme is beneficial in resolving the flow field at a higher CFL number due to larger global timestep. Eventually, the improvement is manifested in achieving a smaller unsteady simulation time. Finally, the global timestep of 2.0×10^{-4} and 5 levels of grid adaptation are chosen for the numerical experiment. The chosen timestep is identical to the first simulation, but the number of grid adaptation level is increased. It results in the creation of smaller sized cells and consequently, increases the maximum CFL number achieved in the computational domain. Maximum CFL number of 500 is achieved in the computations. The solution from the Mid-point scheme is compared with the computational result from the backward difference scheme using the identical set of input parameters. Fig. 62 shows the comparison of the lift coefficients using both the schemes. Similar to the observation with the previous computational test, the deterioration in the evolution of the lift coefficients is observed in using the Mid-point scheme. In this case 30% gain of the CPU time is observed in using BDF scheme over the Midpoint method.

Considering observations from both the numerical experiments, it is inferred that the Backward difference scheme has a higher numerical stability compared to the Mid-point scheme and thus, beneficial to the computations in using higher CFL number. The required increase in the CFL number of the computation can either be due to the increase in the global timestep or as a result of higher level of grid adaptation, which decreases the grid size. The increase in the global timestep helps in reducing the simulation time and the grid adaptation improves the

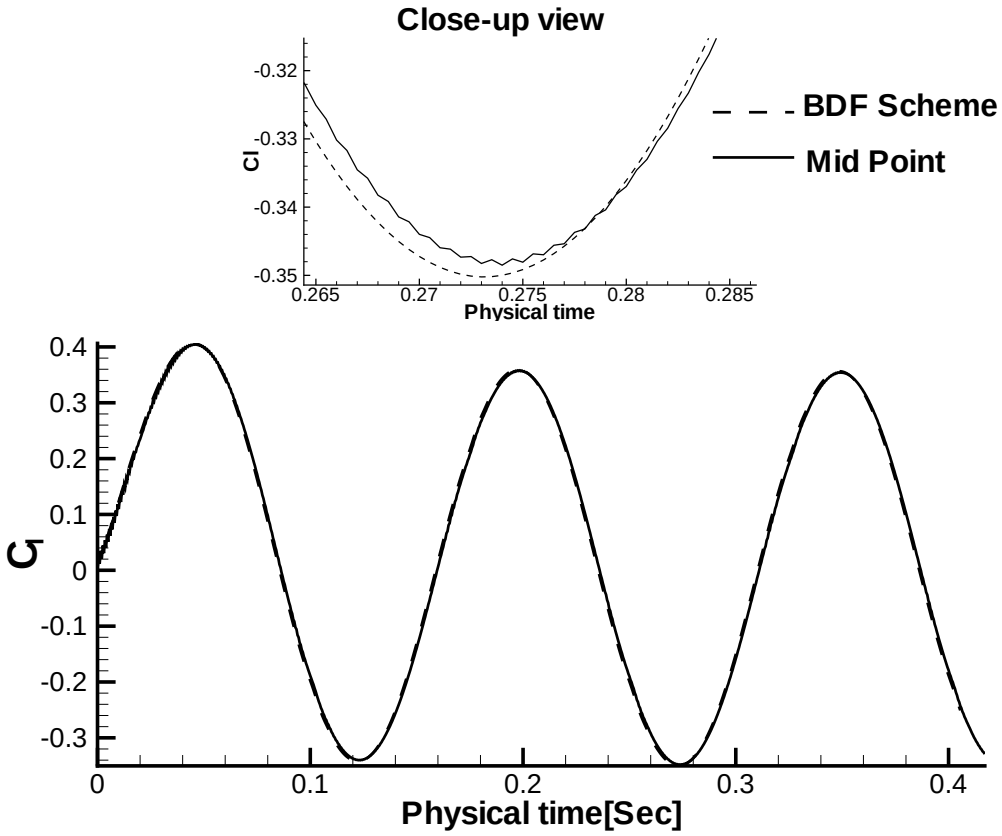

Figure 62: Comparison of the robustness in the schemes for 5 level adapted grid, Global timestep 2×10^{-4}

solution accuracy. Simulations with BDF scheme are able to achieve higher value for both the parameters, which provides benefit to the computations. It is observed that, the solution obtained by using the BDF scheme is in excellent agreement with the Mid-point scheme at a lower CFL number in the computational domain.

3.5 Accelerating convergence of explicit time integration scheme with Multigrid technique

3.5.1 Testing of grid coarsening algorithm

Grid coarsening algorithm described in the numerical modelling section 2.10 is implemented in Quadflow and tested on both the adaptive mesh with hanging nodes and multi-block structured mesh without hanging nodes. A multiblock structured grid, generated using the commerical mesh generation tool ICEM comprising of 512 and 64 cells in the circumferential and cross-stream directions, respectively is considered. The boundary of the computational domain lies approximately at a distance of 20 chord lengths from the airfoil. The grid has no hanging nodes in the computational domain.

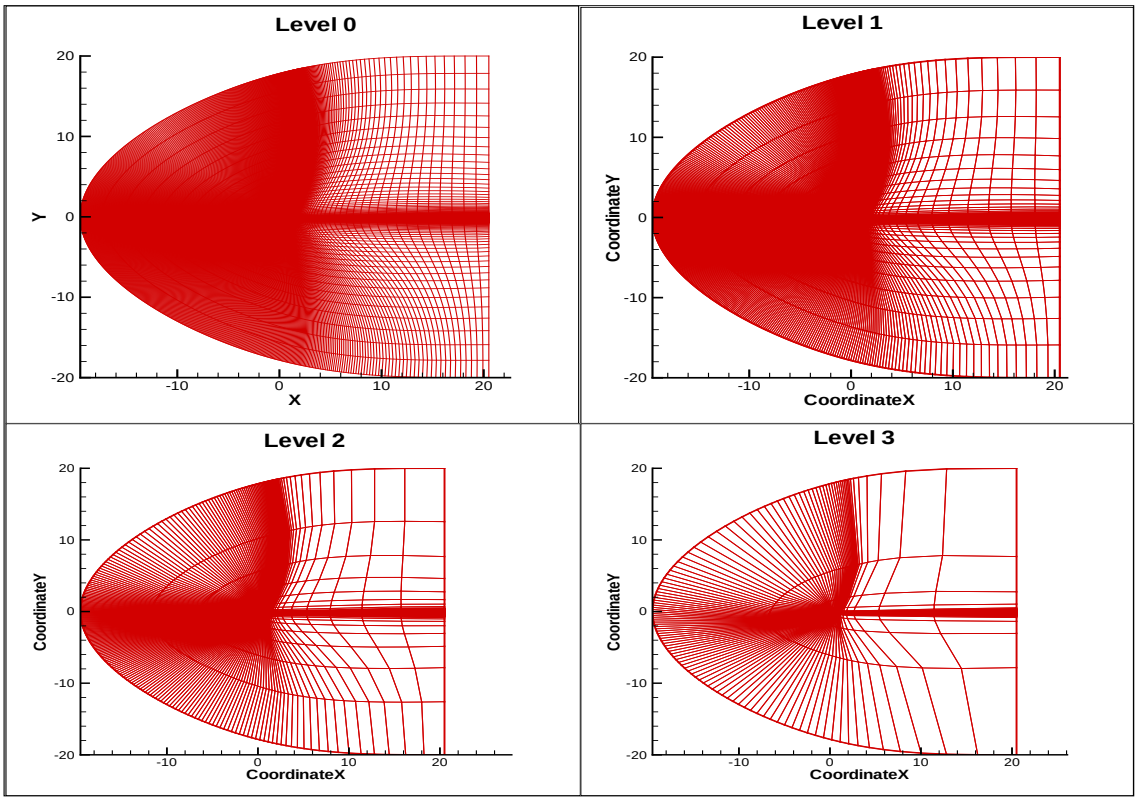

Figure 63: Hierarchy of coarse grids generated from an original grid with ”C” block topology

In order to maintain the consistency of the grid coarsening algorithm, the cells at the initial grid level is assigned with the tags containing the information on their block, level and indices. These information are used during coarsening procedure to detect the cells belonging to the quadruple in the same block and coalesced to generate the coarse mesh. In the absence of gid adaptation, the cells in the finest grid level is assigned with a specific level information, which is decreased during every successive generation of the coarse grid level. Four levels of coarse grids are created from the finest level grid, as shown in the Fig. 63.

3.5.2 Multigrid cycle

The ”V” cycle Multigrid algorithm described in section 2.10, is used to quantify the convergence acceleration achieved for an adptive inviscid flow simulation over the SFB profile. The freestream Mach number and angle of attack are set to $M_\infty = 0.85, \alpha = 0^\circ$.

A sequence of coarse meshes is generated (not shown here) using the adapted grid available at the beginning of the computation after every adaptation as the finest grid level. The number of coarse mesh levels increases with the increase in the grid adaptation level in the computation. Explicit time integration scheme is used to temporally evolve the steady flow field, with the CFL number being fixed at 0.8. Three pre-smoothing iterations are carried out at every grid level before the residual and the conservative solution vector, being restricted to the next coarser level. The restriction of the solution and residual is carried out using volume weightage technique to ensure the conservation of the flow variables in the control volume. One post-smoothing

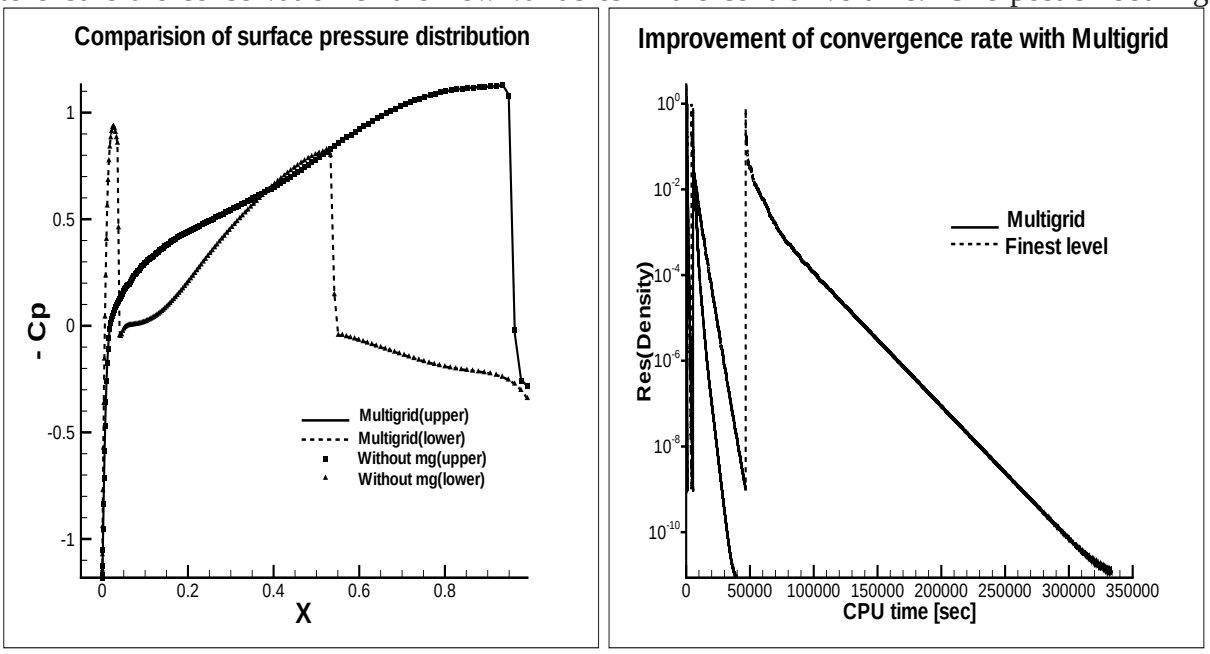

a) Surface static pressure distribution b) Convergence acceleration (Explicit scheme)

Figure 64: Convergence acceleration of the explicit time integration scheme with Multigrid method

iteration is carried out on every coarse grid levels as the algorithm moves towards the finest grid level. The correction of the solution variables on the coarse grid is prolongated using an upwind method, as described in the section 2.10.3, to the next finer grid level for updating the solution. Fig. 64 compares the surface pressure distribution obtained using the Multigrid simulation with the solution from the computation performed at the finest grid level. Multigrid accelerates the convergence by approximately a factor of seven compared with the simulation on the finest grid level without any significant change in the accuracy. Memory requirement during the computations with explicit time integration scheme is much less compared to the implicit time integration scheme.

3.6 Numerical simulation of the shock buffet phenomenon

Shock buffet is an aerodynamic phenomenon characterised by self-sustained shock oscillation over the surface of the profile as a result of the mutual interaction between the shock and the boundary layer. The phenomenon has been observed with different airfoils and wings in the transonic regime [34, 53]. The phenomenon has recently got a significant attention as exhibited by the number of researches conducted during past few years [34, 52, 53, 55].
Understanding of the physical mechanism governing the phenomenon and its accurate numerical simulation is essential as,

- The large scale variation of the lift coefficient associated with the shock buffet imposes a limit on the cruising speed of the aircraft. Hence, limiting the intensity of the shock buffet is essential during the design of the wings.
- The wing is subjected to a periodic fluctuation of the aerodynamic load during the oscillation of the shock, which may trigger aeroelastic vibration.

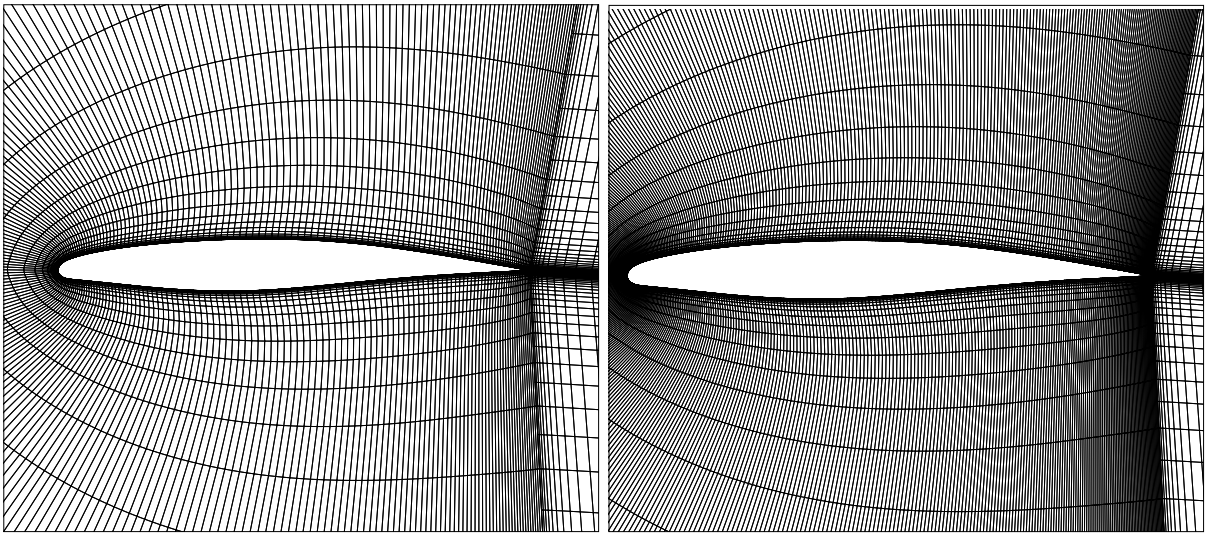

a) Grid A: Coarse grid b) Grid B: Moderately refined grid

Figure 65: Coarser grids used for the computation of shock buffet phenomenon observed in the transonic flow about the BAC3-11 airfoil in KRG Göttingen

In the current study, unsteady numerical simulation without grid adaptation has been performed over a super-critical airfoil using the BDF scheme to investigate the shock buffet phenomenon. The part of the numerical scheme (Eqn. (23) in section 2.4.3.1) accounting for the moving grid simulation is switched off, as the airfoil in the computational domain is stationary.

The critical parameters of the shock buffet flow field namely,

- the onset of the buffet phenomenon

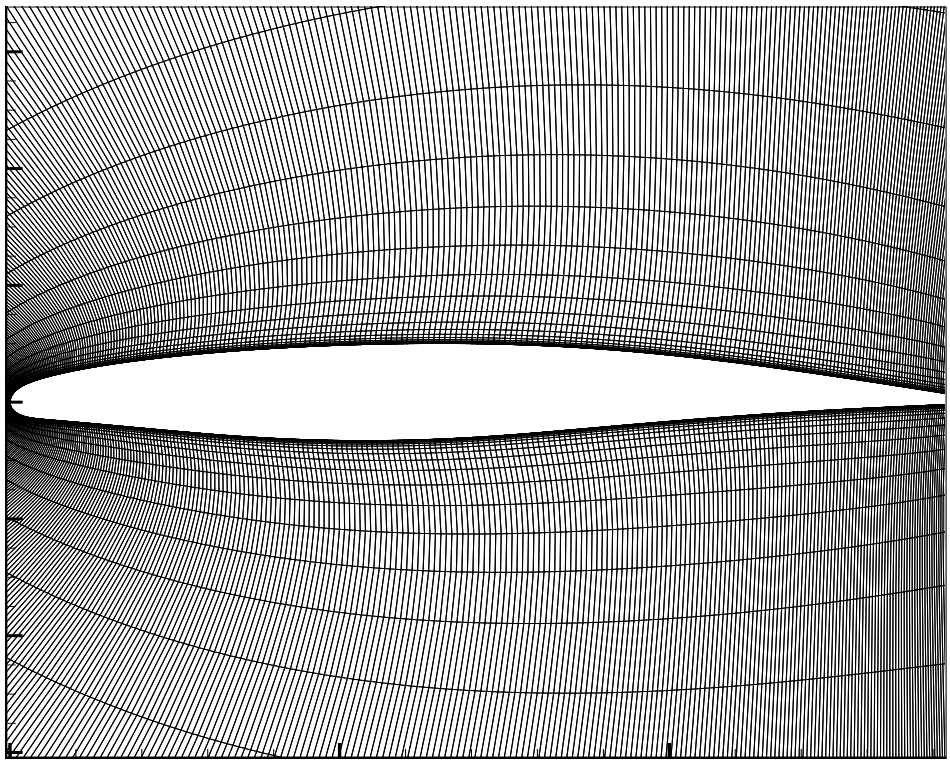

Figure 66: Grid C: Finest grid used for the computation of shock buffet phenomenon

- the time-period of shock oscillation
- the temporal fluctuation of the static pressure coefficient

on the surface of the airfoil are studied during the numerical experiment.

The profile under study is the BAC 3-11/RES/30/21 profile in its cruise configuration with the maximum thickness 11% of the chord length. The chord length of the airfoil used for the simulation is 0.12meter. The inlet flow parameters of the computation correspond to the shock buffet case observed in the experiment conducted at KRG and reported in [11, 23]. The free stream Mach number, angle of attack and the Reynolds number of the computation are set to $M_\infty = 0.75, \alpha = 4^\circ, Re = 4.2 \times 10^6$, respectively. This specific flow condition is used in the simulation as the experimental data can be used for verification in the accuracy.

It is observed by Soda [53,54] that, the computational parameters such as the turbulence model, spatial discretisation scheme and the order of time discretisation in the numerical simulation play important roles in the resolution of the shock buffet. On the basis of the numerical experiments conducted by Soda [53], it is reported that the upwind scheme with one equation turbulence model has the ability to predict the onset of shock buffet over a thick airfoil. Nietzsche [55] has been successful in numerical modelling of the shock buffet using the finite volume URANS solver, DLR-TAU code.

In the current study, the second order spatial discretisation is achieved through reconstruction

using Green-Gauss method and the convective flux is computed using HLLC [62] scheme. The computation is performed assuming the flow to be fully turbulent. Flow is simulated with Unsteady RANS using one equation Spalart-Allmaras model. Second order accurate backward differencing is used for temporal resolution. The effect of grid resolution, particularly in the flow stream direction, on accuracy of simulating the shock buffet has been addressed.

The computational domain is discretised with a C-grid comprising three blocks. Grids with three different spatial resolutions are considered for numerical analysis. Grid ”A” shown in the Fig. 65 is relatively coarse for simulating the shock buffet. The block surrounding the airfoil is comprised of 256 cells along the airfoil surface and 32 cells along the normal direction to the solid surface. The complete domain is constituted of 12288 cells. The grid is clustered near the wall along the normal direction to achieve a y^+ below unit.

Grid ”B” is moderately refined with 512 cells covering the entire surface of the airfoil and constitutes of 32 cells spanning in the cross direction from the airfoil surface to the boundary of the block encompassing the airfoil. Grid ”B” is created with insertion of additional cells along the chord-wise direction on the airfoil profile in Grid ”A”. The number of cells along the cross-stream direction is kept identical with the grid ”A”. The improved clustering along the chord-wise direction in grid ”B” helps in achieving an improved resolution of the flow in the streamline direction. A surface distribution value of y^+ closer to unit is observed with the grid ”A”. Hence, the number of cells in the cross-stream direction is expected to be sufficient for the accurate resolution of the boundary layer and is kept identical in grid ”B” with the grid ”A.

The improved grid resolution as a result of the anisotropic grid refinement aids in an improved capturing the flow field without unnecessarily increasing the computational time. Improving computational efficiency of the simulation is essential as the flow computation needs to be carried out with an unsteady time integration scheme in a time accurate manner. Total number of cells in the computational domain of grid ”B” is 20480.

Grid ”C” is created with further addition of the cells on the airfoil surface along the chord-wise direction. The grid has the finest resolution with 640 cells along the chord-wise direction and 32 cells along the normal direction. The complete domain is comprised of 24576 cells. The boundaries of the computational domain is 24 chord lengths away from the leading and trailing edge of the airfoil, which allows the strength of the wake originated at the trailing edge of the airfoil to be reduced during reaching the boundaries. Extrapolation type boundary condition (section 2.7.1.3) is applied for closure. The global timestep for unsteady simulation is set to 1.0×10^{-6}.

Initially, the computations are performed with the backward-Euler steady time integration scheme without consideration for temporal accuracy. It is observed that the computation with Grid ”A” resulted in a converged solution with a decrease in 5 order of the residual level compared to the initial value, as shown in Fig. 67a). A converged lift coefficient corresponding to the final solution is achieved, shown in Fig. 67b).

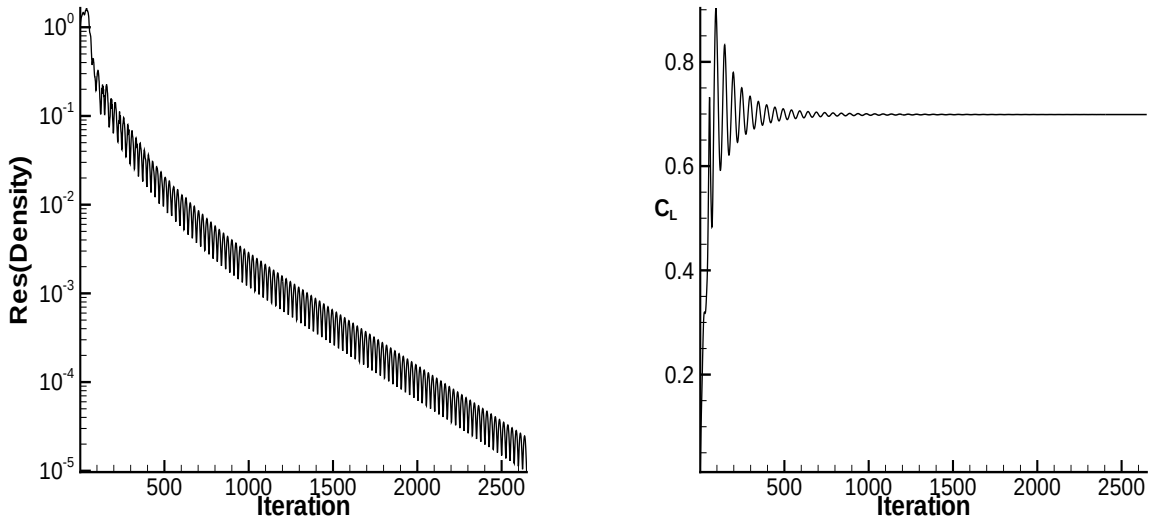

a) Convergence of residual b) Convergence of lift coefficient

Figure 67: Steady solution computed on the grid ”A”

The flow field is initialised with the previously obtained steady solution and computation is performed in a time accurate manner using Backward Difference scheme. Jacobian is obtained using analytical formulation (section 2.8) and the number of Newton steps are set to achieve a convergence of 10^{-4} during the inner iterations.

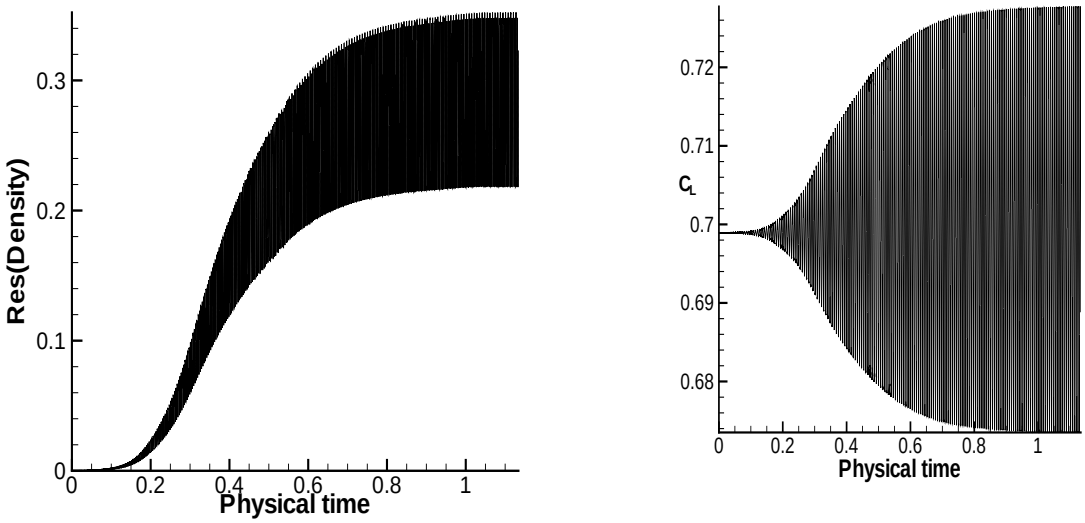

a) Fluctuating residual

b) Fluctuating lift coefficient $\alpha = 4.01^{\circ}$

Figure 68: Unsteady solution computed on the grid ”A”

The linear system of equations arisen during the linearisation process is solved using preconditioned restarted GMRES. Incomplete Lower Upper (ILU(2)) method is applied to create the preconditioning matrix for the linear equation solver. The global timestep is set to 1.0×10^{-6},

which is comparatively smaller than the expected time period of the shock buffet. The residual is observed to be oscillating periodically Fig. 68 (a). Unsteady computation shows a conspicuous oscillation of the lift coefficient with a gradual growth in the amplitude before achieving a periodic steady state as shown in the Fig. 68 (b).

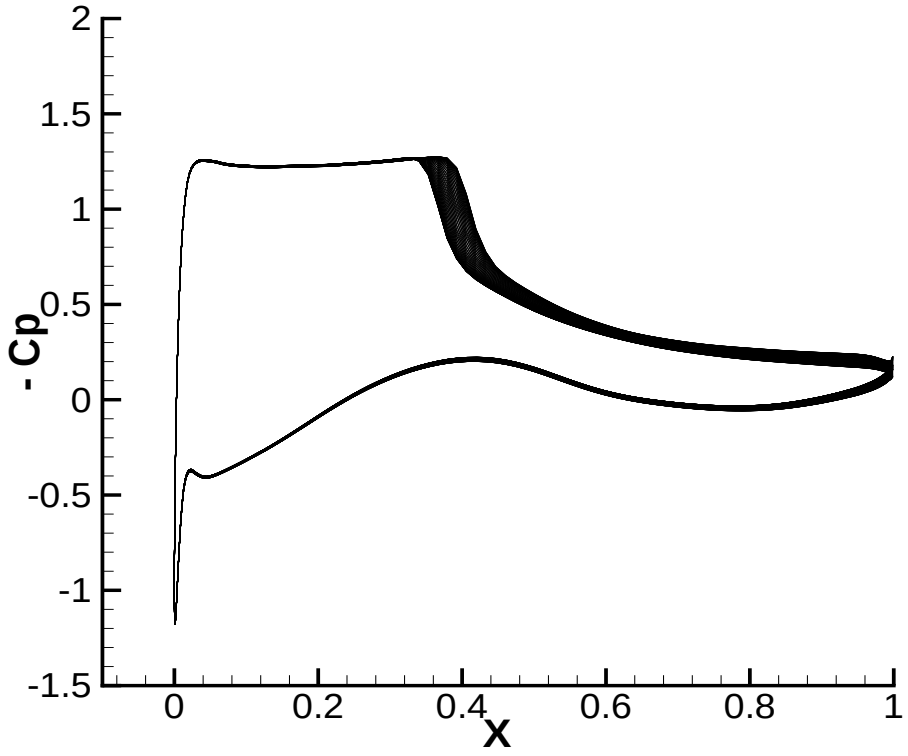

Predicted variation of C_p using grid-A

Figure 69: C_p distribution, Unsteady solution computed on the grid ”A”

The analysis of the flow field explains the reason of the periodic fluctuation, which can be attributed to the movement of the shock on the suction surface of the airfoil. The movement of the shock creates the variation of static pressure coefficient on the surface of the airfoil as shown in the Fig. 69. The distance traversed by the shock predicted by the numerical simulation is smaller than observed in the experimental data. The estimated shock oscillating frequency (144 Hz) is found to be larger than the experimental value (125 Hz).

Computation is performed using steady time integration scheme on the relatively refined grid ”B”. The residual is observed to be fluctuating and a converged solution is not obtained. The variation of the residual and the lift coefficient with timestep are plotted as shown in the Fig. 70. Hence, the further computation has been performed in the time accurate manner to resolve the unsteady flow field. Temporal variation of the residual and the lift coefficient from the unsteady computation are shown in the Fig. 71 a) and b).

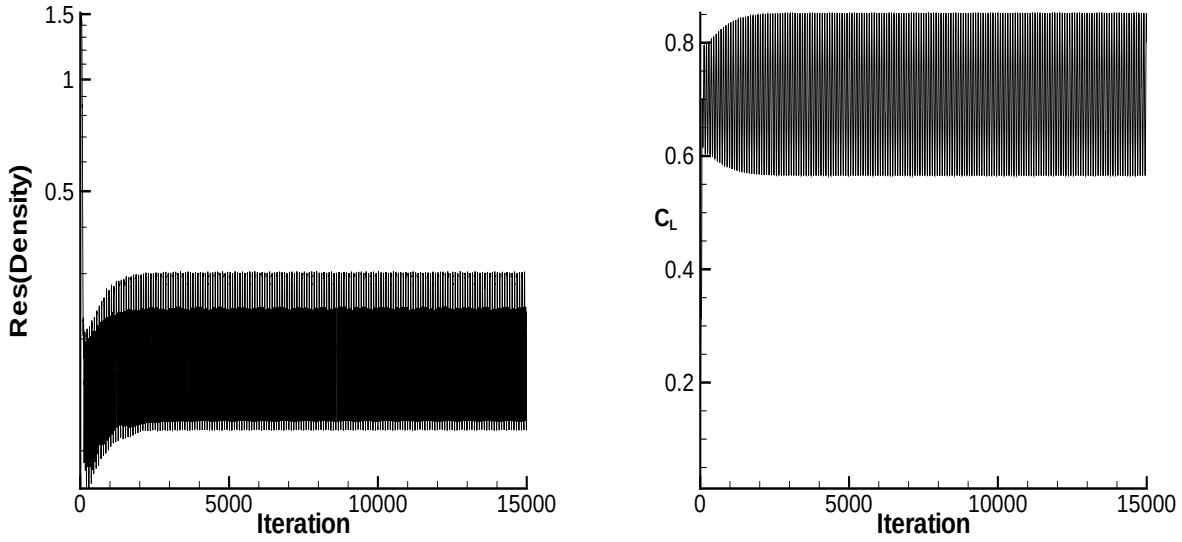

a) Residual history b) Convergence history for the lift coefficient

Figure 70: Steady solution computed on the grid ”B”

The lift coefficient goes through the initial transience (similar to the observation with grid ”B”) to achieve a periodic steady state. Variation of the static pressure on the upper surface of the profile as a result of the shock movement is shown in Fig. 72.

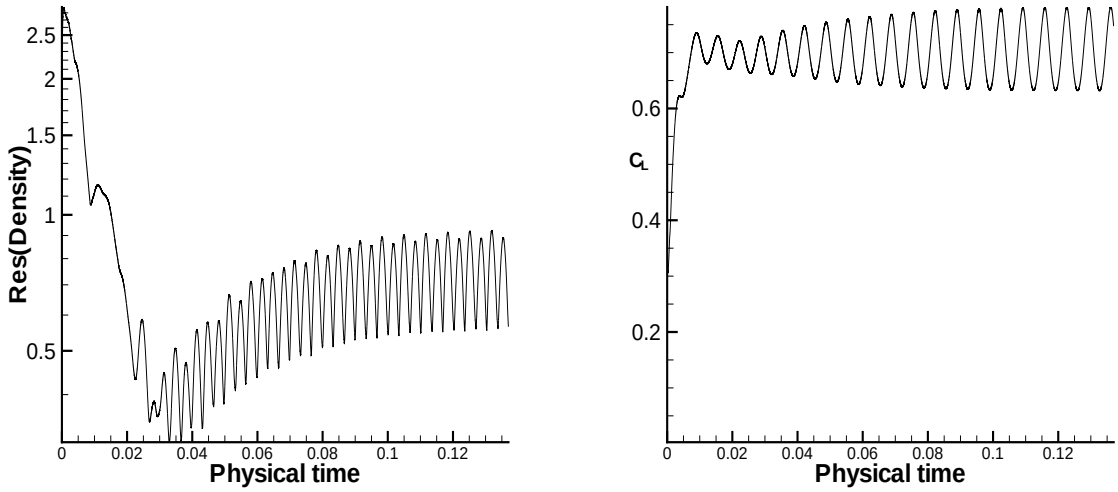

a) Fluctuating residual b) Fluctuating lift coefficient

Figure 71: Unsteady solution computed on the grid ”B”

The traversing distance of the oscillating shock is visibly larger than the value estimated with computation on grid ”A”. This improvement can be attributed to the improved accuracy in the resolution of the flow along the chord-wise direction.

The frequency of the shock movement is estimated to be 140, which is closer to the experimental

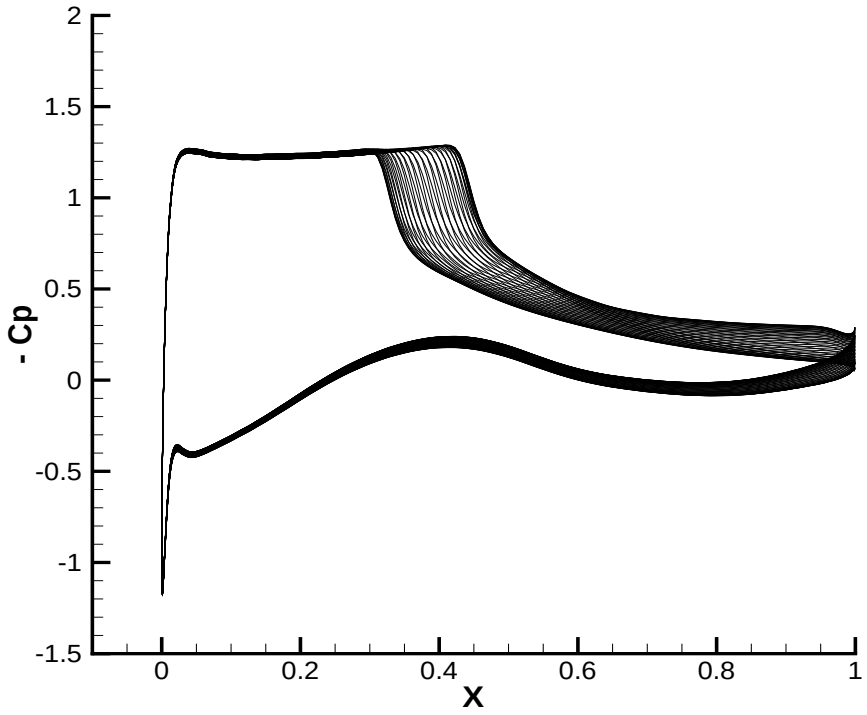

Figure 72: C_p distribution, Unsteady solution computed on the grid "B"

value (125) compared to the previously estimated frequency with grid "A".
The near wall grid cells with large aspect ratio, used in the turbulent flow simulation are usually designed to capture the boundary layer. Therefore traditionally, grid clustering along the normal direction for achieving the right y^+ distribution on the surface and the number of grid cells inside the boundary layer are the factors usually targeted during the grid generation process.
As accurate resolution of the shock buffet needs simultaneous improved capturing of the shock, moving along the airfoil profile and the viscous boundary layer, present normal to the surface profile; the grid design criterion has to be modified to provide a better clustering in both the directions. The improvement in the numerical prediction of the shock oscillating frequency achieved using grid "B" is as a result of increased grid resolution in the chord-wise direction to capture the flow phenomenon of the shock movement, demonstrates the proposition.
Further computation is performed with a highly refined grid "C". Similar to the previous computation, convergence to the steady state can't be achieved with a steady time integration scheme. The low Reynolds number model used in the simulation necessitates achieving a value of y^+ below unit in order to resolve the boundary layer flow structures. Fig. 73 a) shows the distribution of y^+ on the suction and pressure surfaces of the airfoil. The refinement of the cells along the cross-stream direction helps in achieving the maximum value of y^+ below unit along the surfaces.

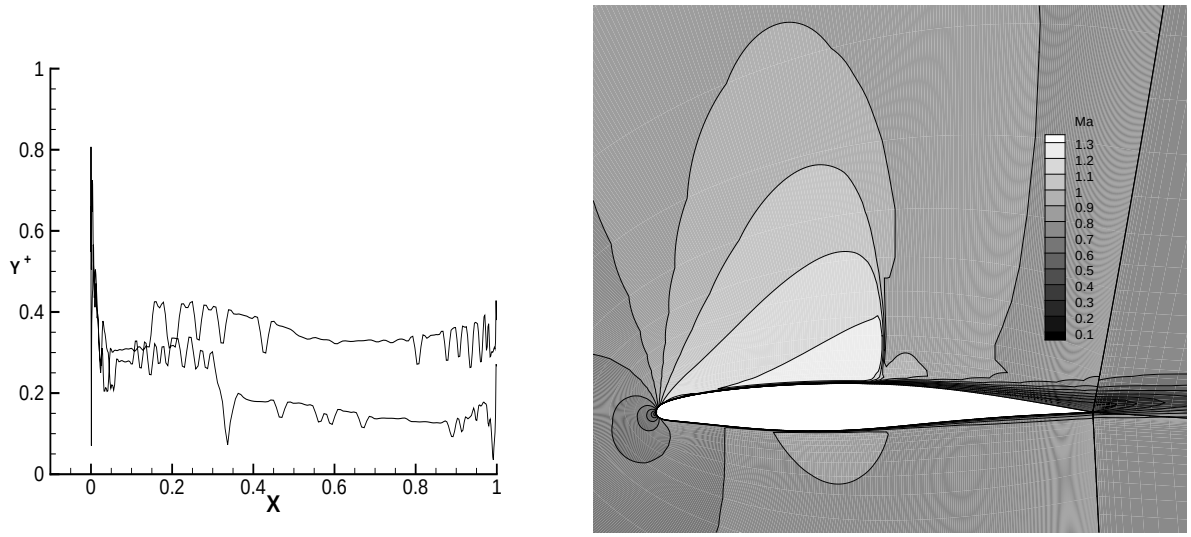

a) Surface y^+ distribution b) Instantaneous Mach number distribution

Figure 73: Unsteady solution computed on the grid ”C”

Unsteady simulation is conducted in order to capture the time accurate flow features. Periodic fluctuation of the residual and the lift coefficient obtained from the time accurate computation are shown in the Fig. 74 a) and b).

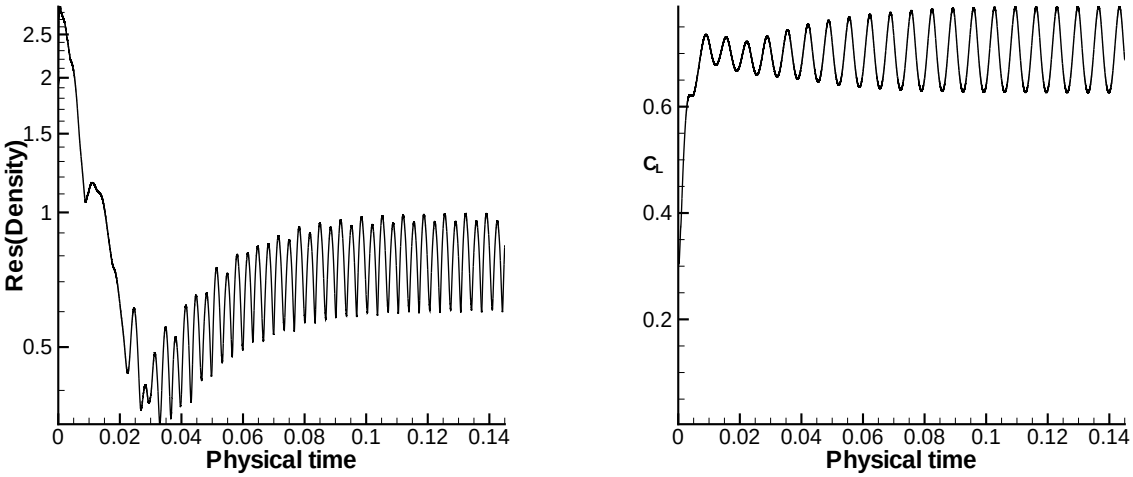

a) Fluctuating residual b) Fluctuating lift coefficient

Figure 74: Unsteady flow parameters computed on the grid ”C”

An instantaneous Mach number distribution in the computational domain is shown in the Fig. 73 b). The flow physics leading to the onset of the shock buffet is explained by Deck [34]. The flow is accelerated over the suction surface of the airfoil to create a patch of supersonic region in the computational domain which is termined by the creation of a shock. The fluid across the shock undergoes compression and a high pressure region is developed in the downstream of the shock.

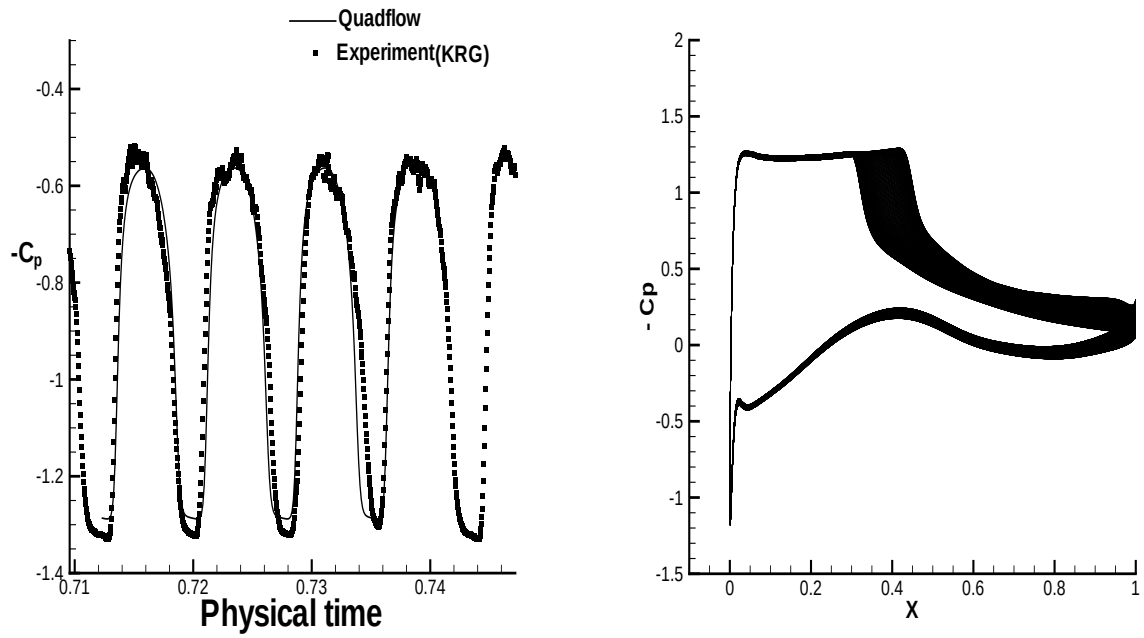

a) Temporal variation of Cp at $x = 0.46$ b) Variation of Cp along the profile

Figure 75: Unsteady solution computed on grid ”C”

A small scale flow separation is occurred when the the fluid overcomes the adverse pressure gradient created as a result of decreasing thickness of the airfoil. The presence of the supersonic region on the suction surface of the profile is terminated with the shock and a small separation bubble trailing the shock is observed in Fig. 73b). The flow parameters, e.g. the free stream Mach number and the angle of attack, leading to the creation of the separation bubble through controlling the acceleration of the fluid on the suction surface determines the onset of the buffet phenomenon. The thickness of the profile and its variation towards the trailing edge are the critical geometrical parameters in detecting the onset. As the phenomenon involves viscous-inviscid interaction, the Reynolds number plays an important role in determining the buffet onset. The pressure signal transmitted from the fluctuating wake in the presence of the separation bubble along the upstream direction causes the oscillation of the shock. The frequency of oscillation and the distance traversed by the shock during periodic fluctuation, computed using grid ”C” are close to the values obtained using grid B, confirms the grid independence of the numerical simulation.

Temporal variation of the surface pressure coefficient for a point situated at 46% of the chord length is compared with the experimentally obtained value as shown in Fig. 75a). The excellent agreement of C_p between the computational values with the experimental data confirms the accurate numerical capturing of the shock intensity in the shock buffet phenomenon. Fig. 75b) shows the spatial variation of surface pressure coefficient along the profile due to shock oscillation.

3.7 Computational simulation of the flow field over 3D configurations

The computational results described in this section demonstrates the applicability of Quadflow in three-dimensional flow simulations.

3.7.1 Inviscid flow over the swept bump

A bump with thickness, 4% of the chord length is present in the X-Y plane of the computational domain. The starting and end locations of the bump in the X-Y plane is gradually varied in the Z direction to achieve a three-dimensional configuration, inclined at angle of 34° with the Z axis.

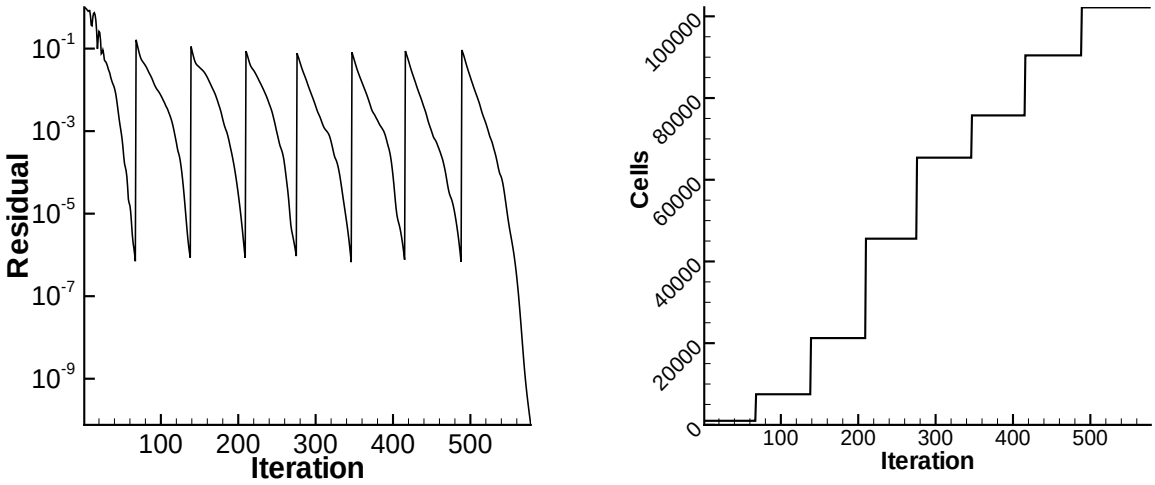

Convergence history Variation of number of cells

Figure 76: Convergence behaviour of the 3D computation over the inclined channel

The free stream Mach number of the flow and the angle of attack (α as referenced in the Fig.14) are prescribed as 0.85 and 0° respectively. The angle in the azimuthal direction (θ in the Fig.14) is set to 87°.

The computational domain is spread three chord lengths along the upstream and five chord lengths in the downstream directions from the end points of the bump. The initial grid level has 1000 cells in the domain. Following computational techniques and parameters are used for the simulation. Seven levels of grid adaptation is carried out, with every time the grid undergoing adaptation when the intermediate residual is decreased by five orders of magnitude relative to the initial residual. Ten order fall in the residual is achieved in the final adapted grid level to obtain the converged solution. Characteristic boundary conditions imposed at the inflow and outflow boundaries are observed to be effective in transmission of the characteristics through the computational domain with reduced size. The inviscid slip wall boundary condition on the bump surface is achieved by setting the normal velocity of the flow to zero.

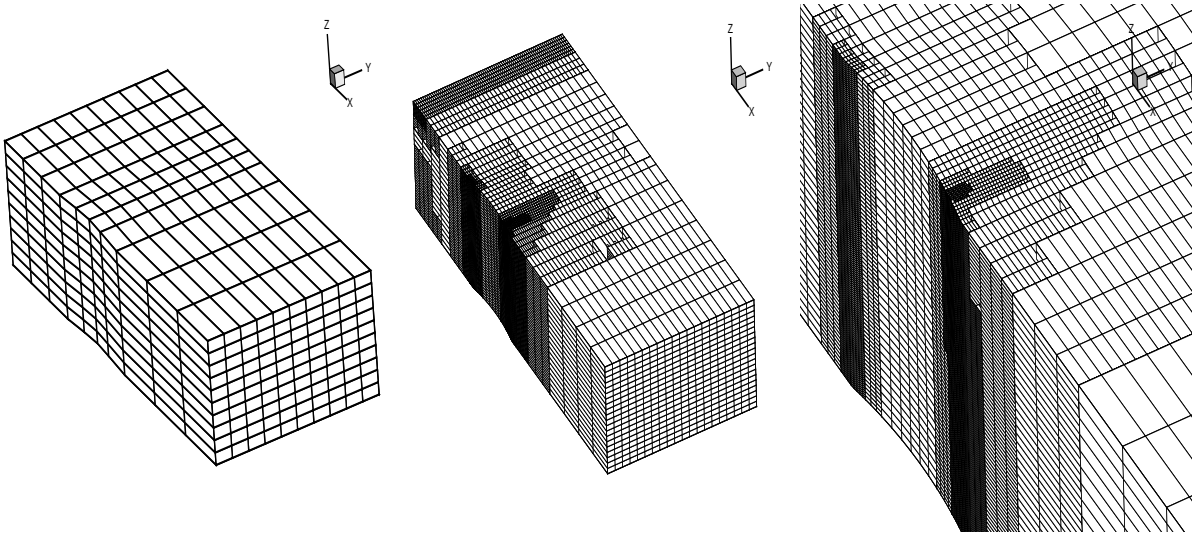

Initial grid Final grid Final grid: Close up

Figure 77: Grids used for computation

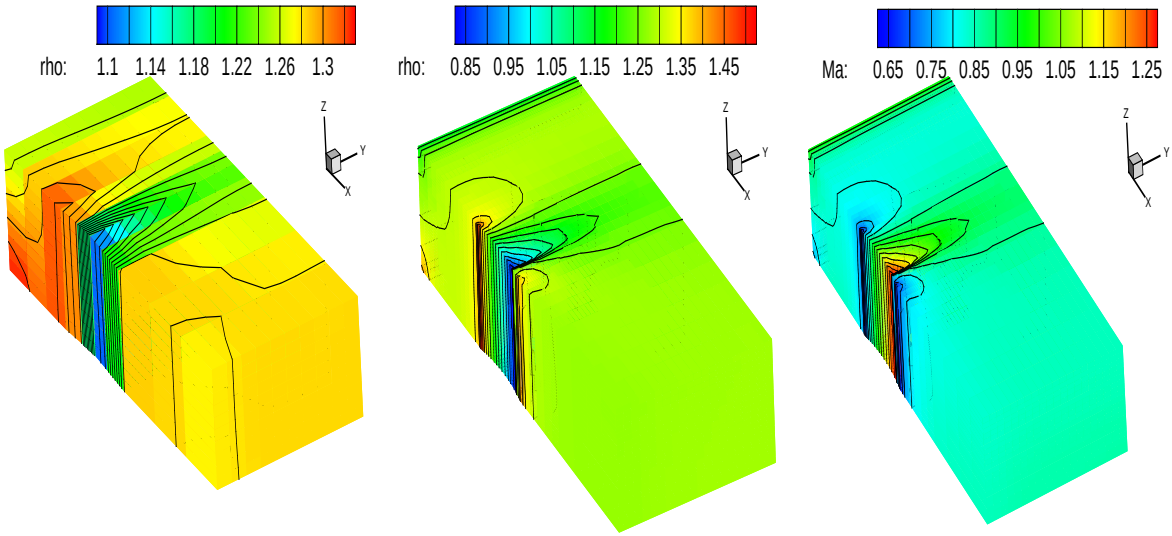

Variation of density on the initial grid

Variation of density on the final grid

Mach number variation

Figure 78: Flow solution over the three-dimensional swept bump configuration

Second order reconstruction, using the least square method is employed for spatial discretisation. Approximate Riemann solver with HLLC scheme is used for the computation of convective fluxes. First order temporal resolution is achieved using the Backward Euler scheme. Local time-stepping with maximum CFL number of 10^5 is used to accelerate the convergence for obtaining the final steady flow solution. The CFL number at the start of the computation is set to 0.8 and increased at the geometric progression with a factor of 1.1. A single Newton iteration step is used and the Jacobian matrix is formed analytically. The system of linear equations is solved using preconditioned restarted GMRES. Incomplete Lower Upper (ILU(2)) preconditioner, built from the Jacobian matrix is used. Fig. 76, shows the convergence plot and the variation of number of cells in the computational domain, obtained during the computations. Approximately 600 timesteps are required for the computation. The number of cells in the domain is gradually increased with successive adaptation to achieve 100,000 cells at the final grid level. The growth rate of the number of cells in the domain is relatively higher, as one cell is refined isotropically to create 8 cells during grid adaptation.

Fig. 77 shows the initial grid used and the final grid achieved after adaptation. The initial grid is coarse, and becomes mainly adapted at the leading and trailing lines of the bump.

Fig. 78 shows the variation of density at the initial and final grids. The flow is accelerated over the bump and a localised supersonic region is created, which is terminated with the presence of a strong shock. The localities around the shock line is refined during successive levels of grid adaptation and well captured.

3.7.2 Three dimensional turbulent flow simulation over the flat plate

Three dimensional turbulent flow with grid adaptation is simulated over the flat plate to demonstrate the capability of Quadflow. The computational domain is discretised with the grid comprising three blocks. The flow is entering into the computational domain at the free stream Mach number, M_∞=0.2 and the Reynolds number is set to 3.52×10^6. Computation is conducted considering the flow to be fully turbulent. Inviscid boundary condition is imposed on the plate belonging to the first block. The grid lines at the junction between the first an second blocks are clustered along the streamline direction to ensure the capturing of the boundary layer at the leading edge of the flat plate. The portion of the flat plate in the second block is imposed with the viscous boundary condition. The part of the flat plate in the third block is set with inviscid boundary condition in order to decrease the influence of the wake at the exit boundary. The inflow and outflow boundaries are dealt with extrapolation type boundary conditions. The first, second and third blocks have 20, 40 and 10 cells respectively along the streamline directions at the first grid level, with clustering imposed at the interface of the block boundaries. Each block has 10 cells, stretched logarithmically to resolve the boundary layer in the direction normal to the wall. The flow in the cross-stream direction is resolved with 10 cells, uniformly spaced in

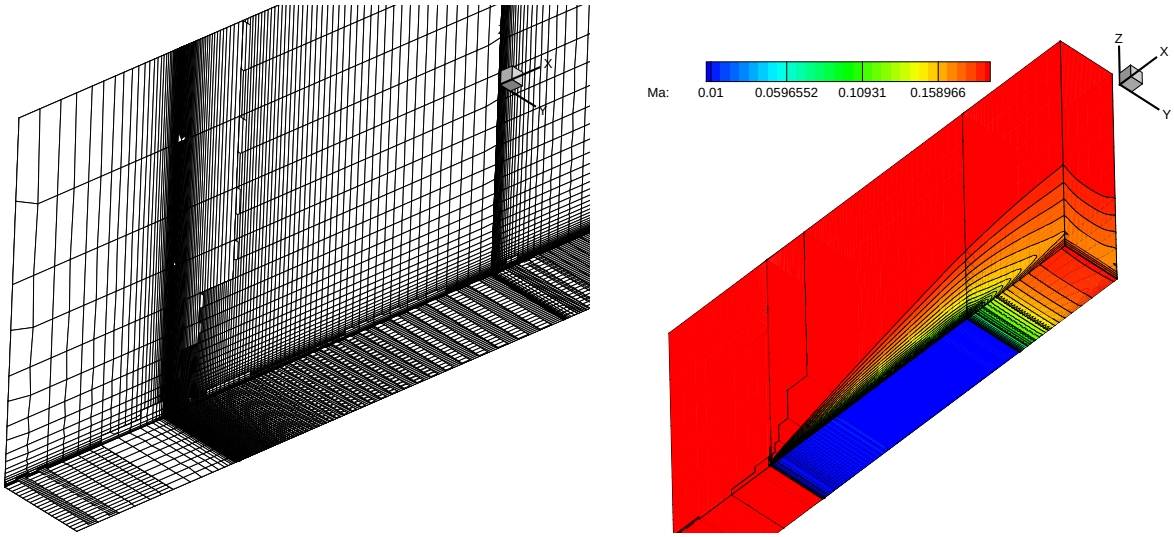

a) Final level adapted three-dimensional grid b) Mach number variation in the domain

Figure 79: Three-dimensional viscous simulation over the flat plate

the computational domain. The initial level grid has 7000 cells. Three levels of grid adaptation is used. The computation is restricted by the number of cells evolved as a result of grid adaptation. The final level grid has approximately 270,000 cells in the computational domain. The final level adapted grid and the variation of Mach number in the computational domain is shown in the Fig. 79.

4 Conclusion

In the course of the work, numerical schemes are formulated, implemented and tested to demonstrate the improvement in accuracy, speed and robustness of the adaptive solver Quadflow.

Turbulent flow solutions over the airfoil profile in cruise condition show an excellent agreement with the data obtained from the cryogenic KRG wind tunnel experiments, conducted at DLR, Göttingen by order of SFB401. The surface static pressure distribution over the profile coincides with the experimental data. The absence of the pressure sensors at the suction peak of the profile and the three-dimensional nature of the flow in the experiment causes a minor deviation in the numerically obtained aerodynamic coefficients from the experimental data.

Detached Eddy Simulation (DES) has been implemented to model the turbulence in the flow field and rigorously tested for the cruise as well as the high-lift configurations in the adaptive solver Quadflow. Grid independent results have been achieved in simulating the steady flow fields. The results predicted by DES are observed to be as accurate as the numerical prediction using S-A RANS model for simulating steady flow on the cruise configuration. The comparison of the *work-units* needed for simulations with DES model shows higher computational efficiency than using the S-A RANS model.

Surface static pressure distribution for the flow over high-lift configuration is in close agreement with the experimental data. The variation of the lift coefficient shows a linear trend at moderate angles of attack. The angle of attack initiating a large scale flow separation associated with the inception is accurately captured using the DES model, whereas the flow simulation with the S-A turbulence model shows a similar trend as observed by the earlier researchers, i.e. overprediction of the stall angle. Unsteady flow simulation carried out with the DES model shows a periodic variation of the lift coefficient explaining the periodic nature of the flow field. The computational domain is observed with a sequence of change in the flow field as a result of formation of a small separation bubble on the suction surface of the main element, its growth and merger with the separation region at the flap; eventually leading to vortex shedding. The repetitive pattern of these flow phenomena gives a time varying nature to the flow field in a periodically steady manner.

Low Mach number preconditioning with DES effectively reduces the computational time in simulating the flow field over the high-lift configuration. The presence of large region of low Mach number flow in the computational domain of the high-lift configuration is the crucial factor in improving the computational speed. The preconditioner is shown to function effectively in the domain comprising a mixture of subsonic and supersonic regions, as occurred to the flow field over the high-lift configuration at a high angle of attack. Preconditioner is shown to be improving the solution accuracy and convergence behaviour of the computation in simulating the flow field at low free stream Mach number.

Implicit backward difference scheme has been formulated and successfully implemented in the

solver for simulating unsteady flow along moving solid surfaces like in aeroelasticity. The derived scheme is shown to satisfy the Geometric Conservation Law, essential for solving Arbitrary Lagrangian Eulerian (ALE) problems. The main purpose of the scheme is to allow using as large global timesteps as limited by the flow physics rather than by the numerical stability of the scheme, thus reducing the simulation time. Computations are conducted to simulate the flowfield over an oscillating NACA0012 airfoil to test and validate the accuracy of the newly proposed scheme in the presence of grid adaptation. Despite implicit schemes are theoretically considered to be unconditionally stable; their formulations and the numerical components such as, the method of Jacobian computation, linear equation solver, type of preconditioner used in the scheme determine the actual stability. Hence, for the purpose of practical flow simulation, the allowable maximum CFL number corresponding to the global timestep is limited. The BDF scheme is shown to be robust enough to function correctly in the presence of larger maximum CFL number in the domain compared to the Mid-point scheme existing already in Quadflow, before. The maximum CFL number in the domain is increased due to the decrease in the cell size as a result of grid adaptation or due to increase in the global timestep. The robustness of the current scheme associated with the improved numerical stability is desirable in reducing the simulation time for adaptive flow simulation.

The physical problem of ”shock buffet”, involving the interaction of the shock with the boundary layer, is computed and compared with the experimentally available data. The dependency of the solution accuracy on grid resolution along the direction of shock traverse is studied. The solution is shown to be significantly improved from the coarse mesh to a fine mesh by anisotropically refining the grid cells on the airfoil profile in the chord-wise direction. The solution obtained using the finest grid shows an insignificant change from the previously used moderately refined grid, thus establishing the achievement in the grid convergence of the final solution. The distance traversed by the shock on the airfoil surface computed using the finest grid is close to the experimental value, albeit the speed of the shock is overestimated. The computationally estimated frequency of shock oscillation (144 Hz) is close to the experimental data (125 Hz). Nevertheless, the temporal variation of the surface static pressure coefficient at a location (46% of the chord length) on the airfoil surface shows an excellent agreement with the experimental data. Quadflow can accurately predict the onset of the shock buffet. Comparison with the experimental data shows, the intensity of the shock strength corresponding to the temporal variation in the amplitude of the surface static pressure coefficient is accurately estimated. The shock traversing distance is in agreement with the experiment. The overestimation of the shock speed resulted in a moderate discrepancy of the shock oscillating frequency between the numerical simulation and the experimental data. The possible improvement in the solution accuracy may lie in improving the numerical order of accuracy in spatial and temporal resolution.

Simulation of the flow field corresponding to three-dimensional configurations demonstrate the

extended capability of the Quadflow.

References

[1] A. Kumar, J. N. Hefner: Future Challenges and opportunities in Aerodynamics, *I*CAS 2000 CONGRESS.

[2] J. P. Slotnick, M. Y. An, S. J. Mysko, D. T. Yeh, S. E. Rogers, K. Roth, M. D. Baker, S. Nash: Navier-Stokes Analysis of a High Wing Transport High-Lift Configuration with Externally Blown Flaps, *AIAA-2000-4219*, 18th AIAA Applied Aerodynamics Conference, 14-17 August 2000, Denvar/Colorado.

[3] K. J. Fidkowski, D. L. Darmofal: Output-Based Error Estimation and Mesh Adaptation in Computational Fluid Dynamics: Overview and Recent Results, *A*IAA Aerospace Sciences Meeting and Exhibit, Orlando, Florida, 8^{th} Jan 2009.

[4] F. Bramkamp, B. Gottschlich-Müller, M. Hesse, P. Lamby, S.Müller, J. Ballmann, K.–H. Brakhage, W. Dahmen: H-Adaptive Multiscale Schemes for the Compressible Navier-Stokes Equations - Polyhedral Discretization, Data Compression and Mesh Generation, in: J. Ballmann(Ed.) Flow Modulation and Fluid-Structure Interaction at Airplane Wings, Numerical Notes on Fluid Mechanics(Springer-Verlag, 2003), Vol. 84, p. 125–204.

[5] F. Bramkamp: Unstructured h-Adaptive Finite-Volume Schemes for Compressible Viscous Fluid Flow, Dissertation, RWTH-Aachen, 2003.

[6] S. Müller: Multiscale Schemes for Conservation Laws, Lecture Notes on Computational Science and Engineering, Vol. 27, Springer, 2002.

[7] P. Lamby: Parametric Multi-Block Grid Generation and Application to Adaptive Flow Simulations, Dissertation, RWTH-Aachen, 2007.

[8] P. Lamby: QIGPMESH-Library Documentation, Institute fuer Geometrie und Praktische Mathematik, RWTH Aachen, 2005.

[9] K. –H. Brakhage, Ph. Lamby: CAGD tools for high quality grid generation and sparse representation, in: B.K.Soni, J.F. Thompson, J.Häuser, P.Eiseman(Eds.), Proceedings of the Ninth International Conference on Numerical Grid Generation in Computational Field Simulations, (Waikiki Beach, Hawaii, 2002) 599–608.

[10] S. E. Rogers, K. Roth, H. V. Cao, J. P. Slotnick, M. Whitlock, S. Nash, M. D. Baker: Computation of Viscous Flow for A Boeing 777 Aircraft in Landing Configuration, *AIAA-2000-4221*, 18th AIAA Applied Aerodynamics Conference, 14-17 August 2000, Denvar/Colorado.

[11] J. Ballmann, A. Dafnis, C. Braun, H. Korsch, H.-G. Reimerdes, H. Olivier: The HIRENASD Project: High Reynolds number Aerostructural Dynamics Experiments in the European Transonic Windtunnel (ETW), *I*CAS 2006, 25^{th} International Congress of the Aeronautical Sciences.

[12] EADS Airbus Gmbh(D), EADS Airbus SA(F), EADS CASA(E), ALENIA(I), Dassault Aviation(F), ETW Gmbh(D), DLR(D), ONERA(F), CIRA(I), NLR(NL), FOI(S), INTA(E), IBK(D), ASR(EL), European High Lift Programme.

[13] R. Rudnik, S. Melber, A. Ronzheimer, O. Brodersen: Three-Dimensional Navier-Stokes Simulations for Transport Aircraft High-Lift Configurations, *Journal of Aircraft*, Vol. 38, No. 5 (2001) 895-903.

[14] S. Kim, J.J. Alonso, A. Jameson: Design Optimisation of High-Lift Configurations Using a Viscous Continuous Adjoint Method, *A*IAA 2002-0844, 40th AIAA Aerospace Sciences Meeting and Exhibit, Jan. 14-17,2002, Reno/NV.

[15] M. Schatz, F. Thiele: Numerical Study of High-Lift Flow with Separation Control by Periodic Excitation, *A*IAA 2001-0296, 39th AIAA Aerospace Sciences Meeting and Exhibit, Jan. 8-11,2001, Reno/NV.

[16] A. Krumbein: Automatic transition prediction and application to high-lift multi-element configurations, *Journal of Aircraft*,Vol. 42, no. 5, 2005, pp. 1150-1164.

[17] R. C. Potter, C. P. van Dam: Viscous-Flow Analysis of a Subsonic Transport Aircraft High-Lift System and Correlation with Flight Data, *NASA-CR-199610*.

[18] T. Cebeci, E. Besnard: An Efficient and Accurate Approach for Analysis and Design of High Lift Configurations, *Canadian Aeronautics and Space Journal*, Vol. 44, No. 4, Dec. 1998.

[19] M. Nemec, D. W. Zingg: Optimisation of High-Lift Configurations Using a Newton-Krylov Algorithm, *AIAA 2003-3957*, 16th AIAA Computational Fluid Dynamics Conference, June 23-26, 2003, Olrando/Florida.

[20] J. Ballmann, A. Dafnis, H. Korsch, C. Buxel, H.-G. Reimerdes, K.-H. Brakhage, H. Olivier, C. Braun, A. Baars, A. Boucke: Experimental Analysis of High Reynolds Number Aero-Structural Dynamics in ETW, *A*IAA 2008-841, 46th AIAA Aerospace Sciences Meeting and Exhibit, 7-10 January 2008, Reno, Nevada.

[21] L. Reimer, A. Boucke, J. Ballmann, M. Behr: Computational Analysis of High Reynolds Number Aero-Structural Dynamics (HIRENASD) Experiments, *I*FASD-2009-130.

[22] J. Ballmann et al: ”Flow Modulation and Fluid-Structure Interaction at Airplane Wings” - Survey and Results of the Collaborative Research Center SFB401, *DGLR 2002 - 009*.

[23] S. Koch, G. Dietz: Druckverteilungsmessungen am BAC 3/11-Profil im KRG zur Ueberprüfung der am Modell benutzen schnellen Drucksensoren unter Kryogenen Bedingungen, *DLR, IB 224-2005 C 18*.

[24] T. J. Chung: *C*omputational Fluid Dynamics, Cambridge University Press, 2002.

[25] F. Bramkamp, Ph. Lamby, S.Müller: An Adaptive Multiscale Finite Volume Solver for Unsteady and steady flow computations. *Journal of Computational Physics*, Vol. 197, pp. 460-490, 2004.

[26] U. Frisch: Fully Developed Turbulence and Intermittency, *Annals of the New York Academy of Sciences*, Vol. 357, pp. 359-367, 1980.

[27] P.R. Spalart: Strategies for turbulence modelling and simulations, *International Journal of Het and Fluid Flow*, Vol. 21, Issue 1, pp. 252-263, June 2000.

[28] Z. She, E. Leveque: Universal Scaling Laws in Fully Developed Turbulence, *Physical Review Letters*, Vol. 72, No. 3, pp. 336-339, 1994.

[29] A. N. Kolmogorov: A refinement of previous hypotheses concerning the local structure of turbulence in a viscous incompressible fluid at high Reynolds number 1, *Journal of Fluid Mechanics*, Vol. 13, Issue 01, pp. 82-85, 1962.

[30] M. Franke, T. Rung, M. Schatz, F. Thiele: Numerical simulation of high-lift flows employing improved turbulence modelling, In*ECCOMAS 2000, Barcelona, September 11-14, 2000*.

[31] T. Rung: Statistische Turbulenzmodellierung, *internal report, Herman-Föttinger-Institut*, Technische Universitaet Berlin, 2000.

[32] T. Rung, F. Thiele: Computational modelling of complex boundary-layer flows, In9^{th} *Int. Symp. on Transport Phenomena in Thermal-Fluid Engineering, Singapore, 1996*.

[33] P. Spalart: Young-Person’s Guide to Detached-Eddy Simulation Grids, *NASA/CR-2001-211032*.

[34] S*é*bastien Deck: Numerical Simulation of Transonic Buffet over a Supercritical Airfoil, *AIAA Journal*, Vol. 43, No. 7, Jul. 2005, 1556-1566.

[35] P. Spalart, L. Hidges, M. Shur, A. Travin: Simulation of Active Flow Control on a Stalled Airfoil, *Flow, Turbulence and Combustion*, **71** (2003) 361-373.

[36] R. M. Cummings, J. R. Forsythe, S. A. Morton, K. D. Squires: Computational challenges in high angle of attack flow prediction, *Progress in Aerospace Sciences*, **39** (2003) 369-384.

[37] D. Cokljat, F. Liu: DES of Turbulent Flow over an Airfoil at High Incodence, *AIAA 2002-0590*, 40th AIAA Aerospace Sciences Meeting and Exhibit, Jan. 14-17,2002, Reno/NV.

[38] F. E. Camelli, R. Löhner: Combining the Baldwin Lomax and Smagorinsky Turbulence Models to Calculate Flows with Separation Regions, *AIAA 2002-0426*, 40th AIAA Aerospace Sciences Meeting and Exhibit, Jan. 14-17,2002, Reno/NV.

[39] C. L. Rumsey: Effect of Turbulence Models on Two Massively-Separated Benchmark Flow Cases, *NASA-2003-tm212412*.

[40] P. Batten, U. Goldberg, S. Chakravarthy: LNS-An Approach Towards Embedded LES, *AIAA 2002-0427*.

[41] C. C. Nelson, R. H. Nichols: Evaluation of Hybrid RANS/LES Turbulence Models Using an LES Code, *AIAA 2003-3552*, 16th AIAA Computational Fluid Dynamics Conference, June 23-26, 2003, Olrando/Florida.

[42] C. J. Roy, J. C. Brown, L. J. DeChant, M. F. Barone: Unsteady Turbulent Flow Simulations of the Base of a Generic Tractor/Trailor, *AIAA 2004-2255*.

[43] P. Spalart, S. Allmaras: A One-Equation Turbulence Model for Aerodynamic Flows, *AIAA 92-0439*, 1992.

[44] T. Knopp, T. Alrutz, D. Schwamborn: A grid and flow adaptive wall-function method for RANS turbulence modelling, *Journal of Computational Physics*, Vol. 220, Issue 1, December 2006.

[45] P. Batten, M. A. Leschziner, U. C. Goldberg: Average-State Jacobians and Implicit Methods for Compressible Viscous and Turbulent Flows, *Journal of Computational Physics*, **137** (1997) 38-78.

[46] A. M. O. Smith: High-Lift Aerodynamics, *Journal of Aircraft*, Vol. 12, No. 6, June 1975.

[47] R. Balaji, F. Bramkamp, F. Hesse, J. Ballmann: Effect of Flap and Slat Riggings on 2-D High-Lift Aerodynamics, *Journal of Aircraft*, 43(5), 1259-1271 (2006).

[48] T. Cebeci, E. Besnard and H. H. Chen: An Iterative Boundary-Layer Method for Multi-element Airfoils, *Computers & Fluids*, Vol. 27, No. 5-6, pp. 651-661, 1998.

[49] Catherine B. McGinley, L. N. Jenkins, R. D. Watson and A. Bertelrud: 3-D High-Lift Flow-Physics Experiment - Transition Measurements, *AIAA Fluid Dynamics Conference and Exhibit*, 6-9 June 2005, Toronto, Ontario.

[50] J. R. Wright, J. E. Cooper: Introduction to Aircraft Aero-elasticity and Loads, John Wiley and Sons Ltd, UK, 2007.

[51] J. Quest, M. C. Wright, H. Hansen, G. G. Mesuro: First Measurements on an Airbus High Lift Configuration at ETW up to Flight Reynolds Number, *AIAA 2002-0423*.

[52] I. Klioutchnikov, J. Ballmann: (2006). DNS of Transitional Transonic Flow about a Supercritical BAC3-11 Airfoil using High-Order Shock Capturing Schemes, *Direct and Large-Eddy Simulation VI. Springer*, Netherlands, pp. 737744.

[53] A. Soda, T. Knopp, K. Weinham: Numerical Investigation of Transonic Shock Oscillations on Stationary Aerofoils, Symposium on Hybrid RANS-LES Methods Stockholm/Sweden, 07/2005.

[54] A. Soda: Numerical Investigation of Unsteady Transonic Shock/Boundary-layer interaction of Aeronautical Applications, Dissertation, RWTH-Aachen, 2006.

[55] Jens Nitzsche: A Numerical Study on Aerodynamic Resonance in Transonic Separated Flow, *IFASD-2009-126*, 2009.

[56] W. Cao, W. Huang, R. D. Russell: A Moving Mesh Method Based on the Geometric Conservation Law, *SIAM Journal on Scientific Computing*, Vol. 24, Issue 1, 2002.

[57] F. Moukalled, M. Darwish: A Unified Formulation of the Segregated Class of Algorithms for Fluid at All Speeds, *Numerical Heat Transfer, Part B*, Vol. 40, No. 2, pp. 99-137, 2001.

[58] A. J. Chorin: A numerical method for solving compressible viscous flow problems, *Journal of Computational Physics*, Vol. 2, Issue 1, pp. 12-26, 1967.

[59] R. Radespiel, E. Turkel, N. Kroll: Assessment of Preconditioning Methods, *Forschungsbericht 95-29*, Institut für Entwurfsaerodynamik, Braunschweig.

[60] J. M. Weiss, W. A. Smith: Preconditioning Applied to Variable and Constant Density Flows, *AIAA Journal*, Vol. 33, No. 11, Nov. 1995, 2050-2057.

[61] J. R. Edwards, Meng-Sing Liou: Low-Diffusion Flux-Splitting Methods for Flows at All Speeds, *AIAA Journal*, **36** (9) (1998) 1610–1617.

[62] P. Batten, N. Clarke, C. Lambert, D. M. Causon: On the Choice of Wave Speeds for the HLLC Riemann Solver, *Siam J. Sci. Comput.*, **18(6)**:1553-1570, 1997.

[63] D. L. Darmofal, B. Van Leer: Local Preconditioning of the Euler Equations: A Characteristic Interpretation, *30th Computational Fluid Dynamics, VKI Lecture Series*, Vol. 1, 1999.

[64] A. Jameson: Transonic flow calculations, *MAE-report 1651*, Princeton University, 1983.

[65] B. V. Leer: Flux-vector splitting for the Euler equations, *Eighth International Conference on Numerical Methods in Fluid Dynamics*, **Lecture Notes in Physics** Vol. 170, pp. 507-512, 1982.

[66] W. K. Anderson, J. L. Thomas, C. L. Rumsey: Extension and Application of Flux-Vector-Splitting to Unsteady Calculation on Dynamic Meshes, 8^{th} *Computational Fluid Dynamics Conference*, June 9-11, Honolulu, Hawaii, 1987.

[67] D. J. Mavriplis: Revisiting the Least-Squares Procedure for Gradient Reconstruction on Unstructured Meshes, *AIAA 2003-3986*, 2003.

[68] A. Brandt: Multi-Level Adaptive Solutions to Boundary-Value Problems, *Mathematics of Computations*, Vol. 31, No. 138, pp. 333-390, 1977.

[69] W. Hackbush: Multi-grid Methods and Applications, Springer, Berlin, 1985

[70] K. Warendorf, U. Kuester, R. Ruehle: Upwind Prolongations for a Highly Unstructured Euler Solver, *Multigrid Methods VI, Proceedings of the Sixth European Multigrid Conference*, Gent, Belgium, September 27-30, 1999.

[71] I.R.M. Moir: Measurements on a Two-Dimensional Aerofoil with High-Lift Devices, *AGARD-AR-303: A Selection of Experimental Test Cases for the Validation of CFD Codes*, Vol. 1 and 2, 1994.

[72] Z. J. Wang: A fast nested multi-grid viscous flow solver for adaptive Cartesian/Quad grids, *Int. J. Numer. Meth. Fluids*, **33** (2000) 657–680.

[73] J. M. Weiss, J. P. Maruszewski, A. S. Wayne: Implicit Solution of the Navier-Stokes Equation on Unstructured Meshes, *AIAA 97-2103*.

[74] C. B. Laney: Computational Gasdynamics, *Cambridge University Press*, 1998.

[75] V. Venkatakrishnan: Convergence to steady state solutions of the Euler equations on unstructured grids with limiters, *Journal of Computational Physics*, **118** (1995) 120–130.

[76] W. K. Anderson, D. L. Bonhaus: An implicit upwind algorithm for computing turbulent flows on unstructured grids, *Computers and Fluids*, **23** (1) (2004) 1–21.

[77] S. Balay, K. Buschelman, V. Eijkhout, W. D. Gropp, D. Kaushik, M. G. Knepley, L. Curfman McInnes, B. F. Smith, H. Zhang: PETSc Users Manual, ANL-95/11 - Revision 2.1.5, Argonne National Laboratory, 2004.

[78] C. Bischof, A. Carle, P. Hovland, P. Khademi, A. Mauer: ADIFOR 2.0 Users' Guide, *Mathematics and Computer Science Division*, Center for Research on Parallel Computation, Technical Report CRPC-95516-S, June 1998.

[79] K. Wilcox and J. Peraire: Aeroelastic Computation in the Time Domain using Unsteructured Meshes, *International Journal for Numerical Methods in Engineering*, Vol. 40, pp. 2413-2431, 1997.

[80] C. Farhat, K. Pierson and C. Degand: Multidisciplinary Simulation of Maneuvering of an Aircraft, *Engineering with Computers*, Vol. 17, pp. 16-27, 2001.

[81] I. Lepot, R. Vigneron, J. A. Essers and O. Leónard: Implicit High-Order Geometrically Conservative Scheme for the Solution of Flow Problems on Moving Unstructured Grids, *Second MIT Conference on Computational Fluid and Solid Mechanics*, June 23-27, 2003 / MA, USA.

[82] Scott A. Morton, Reid B. Melville, Miguel R. Visbal: Accuracy and Coupling Issues of Aeroelastic Navier-Stokes Solution on Deforming Meshes, *Journal of Aircraft*, Vol. 35, No. 5, pp. 798-805, September-October 1998.

[83] C. Hirsch: Numerical Computation of Internal and External Flows, Volume 1: *Fundamentals of Numerical Discretization*, Wiley-Interscience Publication, 1988 *Chapter 2: The Dynamic Levels of Approximation*, pp. 89.

[84] M. J. Pandya, Neal T. Frink, Khaled S. Abdol-Hamid and James J. Chung: Recent Enhancements to USM3D Unstructured Flow Solver for Unsteady Flows, AIAA 2004-5201, August 2004.

[85] J. Thomas, M. Salas: Far-Field Boundary Conditions for Transonic Lifting Solutions to the Euler Equations, *AIAA Journal*, Vol. 24, No.7, pp. 1074-1080, July 1986.

[86] R.H. Landon: NACA0012. Oscillatory and transient pitching, pages 3.1-3.25, Compendium of Unsteady Aerodynamics Measurments, Data set 3, AGARD Report 702, 1983.